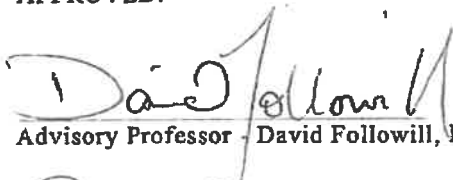


**DEVELOPMENT OF A CT METAL ARTIFACT MANAGEMENT  
ALGORITHM FOR PROTON THERAPY PLANNING (AMPP) FOR HEAD  
AND NECK CANCER PATIENTS**

by

*Daniela Rezende Fiuza Branco, MS*

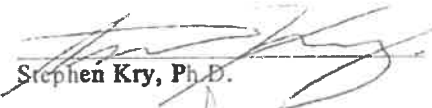
APPROVED:



Advisory Professor - David Followill, Ph.D.



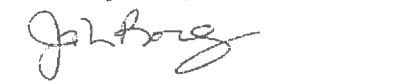
Paige Taylor, M.S.



Stephen Kry, Ph.D.



Xiaodong Zhang, Ph.D.



John Rong, Ph.D.



Steven Frank, M.D.

APPROVED:

\_\_\_\_\_  
Dean, The University of Texas  
MD Anderson Cancer Center UTHealth Graduate School of Biomedical Sciences

**DEVELOPMENT OF A CT METAL ARTIFACT MANAGEMENT  
ALGORITHM FOR PROTON THERAPY PLANNING (AMPP) FOR HEAD  
AND NECK CANCER PATIENTS**

A DISSERTATION

Presented to the Faculty of  
The University of Texas  
MD Anderson Cancer Center UTHealth  
Graduate School of Biomedical Sciences

in Partial Fulfillment  
of the Requirements  
for the Degree of

DOCTOR OF PHILOSOPHY

By

Daniela Rezende Fiuza Branco, MS.

Houston, Texas

August 2020

## ***Dedication***

I dedicate this work to the person who has taught me the meaning of the word *role-model*. The person who has shown me how important it is to selflessly lead by example and to care about his mentees like extended family. The person who, on a work level, knows when to be demanding and assertive, or patient and supportive. And on a personal level, values the importance of a healthy work-life balance and treasures his family more than anything.

Thank you for all the scientific and life lessons, Dr. Dave.

## *Acknowledgements*

I would like to, first and foremost, thank *Dave* and *Becca* for being my family away from family. I feel incredibly fortunate to have been so welcomed into your family.

*Dr. Followill*, for doing much more than showing me how to conduct research and write scientific manuscripts. I would like to thank him for teaching me how to think critically around problems and to always be ahead of the game. I do, however, mostly cherish the immaculate leadership example he was during my 6 years here. Thank you for showing me how to be positive, patient and a selfless mentor every day.

I would also like to acknowledge and thank my committee members for their critical guidance and time. *Paige Taylor*, for her infinite proton knowledge and contributions, unconditional support and availability through the years. *Dr. Stephen Kry*, for all the great ideas and extra projects that, despite seeming like “additional work” at the time, were essential to the development a complete methodology. *Dr. Xiaodong Zhang*, for always being available to help with my proton treatment planning and questions. *Dr. John Rong*, for providing the imaging expertise to the project and always making an effort to teach me how to operate the scanners around the TMC. And last but not least, *Dr. Steven Frank*, for always trying to make sure I had all the resources and information I needed to succeed and complete my work. You all have gone beyond contributing to my understanding of the scientific process – I feel inspired to continue my work in academia.

My sincere thanks to the *Kopchick* family, *John and Char*, for believing in me as a young scientist by funding part of this work and helping me build confidence in my early career.

I would also like to thank *John Costales*, our phantom engineer, for constructing our phantom, *Hunter Mehrens*, for the MATLAB guidance, and *Bobby Gongora*, our PTC proton dosimetrist for the help and advice with my numerous Head and Neck treatment planning questions.

Lastly, I would like to express my appreciation to my parents *Manuel* and *Celeste* for always providing the support I needed in order to be able to focus and achieve my goals. I would like to also thank my brother, *Luciano*, for being so willing to share his programing expertise when mine was at its early stages.

And finally, and last but not least, I would like to thank my *dearest of friends*, *Brazilians* and most recently - last 10 years or so -, *Americans* and *Canadians*. For providing me with the social balance I very much so needed to keep my extroverted mind sane.

**DEVELOPMENT OF A CT METAL ARTIFACT MANAGEMENT  
ALGORITHM FOR PROTON THERAPY PLANNING (AMPP) FOR HEAD  
AND NECK CANCER PATIENTS**

**Daniela Branco, BS, MS, PhD**

**Advisory Professor: David Followill, BS, MS, PhD**

**Purpose:** Dental amalgams (high Z materials) are common sources of artifacts in Head and Neck (HN) images. Commercial artifact reduction techniques have been offered, but many are impractical, produce inaccurate CT images or are not clinically available, thus not widely implemented. The goal of this work is to use CT gantry tilts to develop and evaluate a stereoscopic HN metal artifact management algorithm and investigate its improvement in proton treatment planning.

**Methods:** The in-house CT metal artifact management method for proton planning (AMPP) uses two angled CT scans to generate a single image set with no metal artifacts posterior to the dental metal implants. The algorithm was evaluated (geometrical distortion and HU accuracy) using a geometrical phantom simulating a HN patient with dental fillings. A HN anthropomorphic phantom composed of proton tissue equivalent materials, human skull, air cavities was used to perform a quantitative image quality comparison between AMPP and four major CT vendors' commercial metal artifact reduction (MAR) solutions (OMAR from

Philips, iMAR from Siemens, SEMAR from Canon, SmartMAR from GE), along with their implications on proton dose distributions.

**Results:** The in-house algorithm designed produced geometrically and HU accurate images free of metal artifacts posterior to the oral cavity. AMPP outperformed all vendors' solutions in terms of image quality, showing lower HU differences and fewer bad pixels (4.2% compared to 25.5-65.5%). Dose distributions were negatively impacted by the presence of metal artifacts; the vendor solutions provided varying, but suboptimal, mitigation of this effect. Our in-house algorithm (AMPP) outperformed the vendor's solutions on all treatment plans and showed the most comparable DVHs to the baseline (no metal).

**Conclusion:** A novel in-house algorithm was designed that produces geometrically and HU accurate images free of CT metal artifacts posterior to the HN region. Commercial MAR algorithms were ineffective at reducing artifacts in a HN geometrical and anthropomorphic phantom scenario. Correspondingly, they were not successful at mitigating the impact of artifacts on proton dose distributions. Our in-house algorithm outperformed all four commercial vendor solutions in both imaging and dose distributions, and is ready to be implemented on patients.

# Table of Contents

<b>DEDICATION .....</b>	<b>II</b>
<b>ACKNOWLEDGEMENTS .....</b>	<b>III</b>
<b>ABSTRACT .....</b>	<b>V</b>
<b>TABLE OF CONTENTS .....</b>	<b>VII</b>
<b>LIST OF FIGURES .....</b>	<b>X</b>
<b>LIST OF TABLES .....</b>	<b>XIII</b>
<b>CHAPTER 1 – INTRODUCTION .....</b>	<b>1</b>
1.1 HEAD AND NECK CANCER EPIDEMIOLOGY .....	1
1.2 PROTON THERAPY .....	2
1.2.1 Background .....	2
1.2.2 Proton Therapy Main Applications .....	4
1.2.3 Head and Neck Proton Treatments.....	5
1.2.4 Proton Tissue Equivalent Materials .....	7
1.3 CT IMAGING AND ARTIFACTS.....	8
1.3.1 CT Metal Artifacts in Proton Therapy.....	10
1.3.2 Potential Solutions Available .....	12
1.4 SPECIFIC PROBLEM.....	14
<b>CHAPTER 2 - HYPOTHESIS AND SPECIFIC AIMS.....</b>	<b>16</b>
2.1 CENTRAL HYPOTHESIS.....	16
2.2 SPECIFIC AIMS .....	16
2.2.1 Specific Aim 1: Algorithm Development .....	16
2.2.2 Specific Aim 2: Image Quality Analysis .....	17
2.2.3 Specific Aim 3: Proton Dosimetric Analysis .....	17
<b>CHAPTER 3 - SPECIFIC AIM 1 .....</b>	<b>18</b>
<b>DEVELOPMENT OF A STEREOSCOPIC CT METAL ARTIFACT</b>	
<b>MANAGEMENT ALGORITHM USING GANTRY ANGLE TILTS FOR HEAD AND</b>	
<b>NECK PATIENTS .....</b>	
3.1 INTRODUCTION .....	18
3.2 MATERIALS AND METHODS .....	22
3.2.1 Algorithm.....	22
3.2.2 Step 1: Untilting of image set.....	24
3.2.3 Step 2: Correction of metal artifact.....	26
3.2.4 Evaluation .....	26



3.3	RESULTS .....	29
3.3.1	<i>Qualitative Analysis: Artifact removal attainment</i> .....	29
3.3.2	<i>Quantitative Analysis: Algorithm integrity analysis</i> .....	32
3.3.3	<i>Comparison with Commercial Solution</i> .....	35
3.4	DISCUSSION .....	38
3.5	CONCLUSION .....	41
<b>CHAPTER 4 - SPECIFIC AIM 2 .....</b>		<b>43</b>
<b>IMAGE QUALITY ANALYSIS OF A NOVEL CT METAL ARTIFACT MANAGEMENT TECHNIQUE AGAINST FOUR MAJOR CT VENDOR TECHNIQUES ON AN ANTHROPOMORPHIC HEAD AND NECK PHANTOM ...43</b>		
4.1	INTRODUCTION .....	43
4.2	MATERIALS AND METHODS .....	45
4.2.1	<i>Anthropomorphic head and neck phantom</i> .....	45
4.2.2	<i>Scans</i> .....	47
4.2.3	<i>Data Analysis</i> .....	48
4.2.4	<i>Robustness evaluation</i> .....	49
4.3	RESULTS .....	50
4.3.1	<i>Planar Artifact Severity</i> .....	50
4.3.2	<i>Structure HU number accuracy</i> .....	53
4.3.3	<i>AMPP robustness evaluation</i> .....	54
4.4	DISCUSSION .....	55
<b>CHAPTER 5 - SPECIFIC AIM 3 .....</b>		<b>58</b>
<b>THE DOSIMETRIC IMPLICATIONS OF COMMERCIAL CT METAL ARTIFACT REDUCTION ALGORITHMS AND A NOVEL IN-HOUSE ALGORITHM FOR PROTON THERAPY OF HEAD AND NECK CANCER .....58</b>		
5.1	INTRODUCTION .....	58
5.2	METHODOLOGY .....	61
5.2.1	<i>Anthropomorphic Phantom</i> .....	61
5.2.2	<i>CT image sets and MARs algorithms</i> .....	62
5.2.3	<i>Treatment Planning</i> .....	63
5.2.4	<i>Data Analysis</i> .....	66
5.3	RESULTS .....	66
5.4	DISCUSSION .....	76
5.5	CONCLUSION .....	80
<b>CHAPTER 6 – DISCUSSION .....</b>		<b>82</b>
6.1	GENERAL DISCUSSION .....	82
6.2	RESPONSE TO THE HYPOTHESIS .....	85

6.3	FUTURE STUDIES .....	87
6.3.1	<i>Algorithm Application and Expansion</i> .....	87
6.3.2	<i>Patient Studies</i> .....	89
6.4	CLINICAL IMPLEMENTATION .....	90
<b>CHAPTER 7 – CONCLUSION</b>	<b>.....</b>	<b>91</b>
<b>APPENDIX A</b>	<b>.....</b>	<b>92</b>
<b>APPENDIX B</b>	<b>.....</b>	<b>103</b>
<b>CHAPTER 8 – BIBLIOGRAPHY</b>	<b>.....</b>	<b>105</b>
<b>CHAPTER 9 - VITA</b>	<b>.....</b>	<b>120</b>

# List of Figures

Figure 1. The thermoplastic mask and head mold and screwed into treatment couch. ....	6
Figure 2: Hounsfield Units versus Relative Linear Stopping Power calibration curve .....	7
Figure 3: Diagram illustrating the x-ray fan beam striking the arc of detectors. ....	9
Figure 4: Artifacts caused by metallic dental fillings in Head and Neck patients. ....	10
<i>Figure 5: Diagram representing a patient with HN disease with the range of CT slices affected by the dental work. The red circle shows the region of typical HN disease that gets affected by artifacts resulting from metal in the mouth. ....</i>	<i>22</i>
Figure 6: Diagram of a sagittal view of a HN patient with the CT gantry tilted superiorly (a) and inferiorly (b) showing the artifact-affected slices. In the final artifact-reduced image (c), the posterior region (red circle) is clear, and the artifacts are focused on the anterior region. ....	23
<i>Figure 7: Both halves of the geometrical phantom (a) and the tooth structures without (b) and with (c) metal amalgam fillings used in the testing of the algorithm. ....</i>	<i>27</i>
Figure 8: (a) Sagittal view of the uncorrected image set of the geometrical phantom acquired at a 0° angle with metal teeth. The red box indicates artifact-affected slices. (b) Uncorrected image acquired at a 25° angle appearing tilted and elongated. Inferior tilted scan (c) and superior tilted scan (d) after the first part of the algorithm showing the desired typical axial appearance and corrected to normal height. Final artifact-reduced image reconstructed using (c) and (d). ....	31
Figure 9: Axial and sagittal views of the geometrical phantom after the complete algorithm was applied. Images show the phantom with (a) no metal at 0°, (b) metal at 0°, (c) metal at 5°, (d) metal at 10°, (e) metal at 15°, (f) metal at 20°, (g) metal at 25°, (h) metal. ....	32

Figure 10: Results for distortion measurements showing each difference obtained between the measurements of the different plugs and phantom done with the gantry at 0° with no metal teeth present (baseline) and with metal teeth present for the 6 different CT gantry angles in the AP (a), LR (b), and SI (c) directions.....	33
Figure 11: Hounsfield unit (HU) measurements of all materials for the different CT gantry angles. ....	35
Figure 12: Side-by-side comparison of SmartMAR and the technique developed here to the uncorrected metal scan of the phantom. ....	36
Figure 13: (a) Axial and sagittal CT views of the Alderson phantom prior to modifications. (b) Axial and sagittal CT views of the modified phantom, which included a cylindrical insert containing a central target and 3 healthy structures, and a jaw insert. Holes were drilled in the molars in the jaw insert; these were filled with bone-equivalent materials in this panel. (c) Axial and sagittal CT views of the modified phantom with metal amalgam capsules in the tooth holes. The metal artifacts generated by the capsules are evident. ....	46
Figure 14: (a-e) Axial and sagittal CT views of the anthropomorphic phantom, corrected using the commercial MAR algorithms (a-d) or the in-house-developed AMPP algorithm (e). The same axial slice was chosen from each data set for the analysis.....	51
Figure 15: HU error maps show differences between corrected images and corresponding baseline images. Severe HU differences are displayed by the dark red and dark blue colors. ....	52
Figure 16: (a) Axial and sagittal CT views of the modified Alderson phantom including the jaw insert and the cylindrical insert (containing a central target, parotids, spinal cord). (b)	

Axial and sagittal CT views of the modified phantom with metal amalgam capsules in the tooth holes showing the metal artifacts generated. ....	62
Figure 17: Target contours created (a-e) on the anthropomorphic phantom designed based on real HN patient disease (f-j), respectively. ....	64
Figure 18: Dose volume histograms for the (a) Horseshoe, (b) Sphere and (c) Bean CTVs comparing all the MAR-corrected and not corrected images.....	67
Figure 19: Axial view of the anthropomorphic phantom showing the proton dose distributions for the (a) Horseshoe, (b) Sphere and (c) Bean targets. Each PTV is shown in red for all the different MAR corrected and uncorrected image sets. ....	72
Figure 20: Anterior-posterior and left-right HU profiles extracted from each MAR corrected and uncorrected image set. ....	75
Figure 21: DVH comparison between the Dot target in its original position and the Dot target in area with less severe metal artifacts. The commercial algorithms provide target coverages closer to the Baseline once the target is moved to a location with less artifacts, indicating success in artifact correction is related to location within the phantom. ....	76
Figure 22: Diagram representing a HN patient with metal in the oral cavity showing the extent of the artifacts (dashed lines) on angled CT scans (a-b) and on the final AMPP reconstructed image (c). (d) shows the technique once expanded to also eliminate artifacts in the anterior region (nose and chin) in addition to the posterior region.....	88

## List of Tables

Table 1: Shear and scaling factors used in the affine transformations. ....	25
Table 2: Imaging protocols for all scans obtained. ....	29
Table 3: Mean HU numbers and standard deviations in parenthesis of plugs and phantom for all relevant scans. ....	38
Table 4: HU number differences between the relevant scans for both metal artifact reduction techniques. ....	38
Table 5: Mean HU errors within each structure volume inside the phantom by correction technique. ....	54
Table 6: HU standard deviation (SD) of each structure volume inside the phantom by correction technique. ....	54
Table 7: Mean HU errors within structure volumes and percentages of bad pixels for different imaging parameters under which the AMPP-corrected images were acquired. ....	55
Table 8: Head and neck CT protocols used for the baseline and the metal scans. ....	63
Table 9: Treatment planning parameters used for each target's proton plan designed on the baseline. ....	65
Table 10: Planning evaluation metrics for all targets included in this study. The baseline and AMPP plans are highlighted for ease of comparison. Underlined numbers show a correlation between V100 and D0.03cc values, indicating an overdose (larger D0.03cc) as opposed to achieving quality target coverage ( $V100 = 100$ ). ....	69

# ***Chapter 1 – Introduction***

## **1.1 Head and Neck Cancer Epidemiology**

Cancers that are collectively known as Head and Neck cancers describe malignant tumors of the upper aero digestive tract. This anatomical region includes the oral cavity, pharynx, larynx, paranasal sinuses, nasal cavity, and salivary glands. The oral cavity can be further subdivided into lips, front two thirds of the tongue, gingiva, labial and buccal mucosa, floor of the mouth and hard palate. The pharynx, known as the throat, is a hollow tube about 5 inches long and is composed of 3 parts; nasopharynx (upper region of the pharynx behind the nose), oropharynx (inferior to nasopharynx, including posterior one third of tongue, soft palate and tonsils), and hypopharynx (lower part of pharynx) [1]. Most HN cancers start in squamous cells that line the mucosal surfaces of these regions, and therefore are referred to as squamous cells carcinomas of the head and neck. These malignancies can also start in organs such as the salivary glands, but are less common [2].

Head and neck (HN) cancer is the ninth most common malignancy in the world, with mortality rates continuing to be high despite recent advances in conventional therapy [3]. HN cancer incidence and mortality rates worldwide are attributed to environmental and behavioral risk factors. Tobacco and alcohol are well established risk factors, where each factor alone may account for a two- to three-fold increase in incidence of these malignancies [4]. The various forms of smokeless tobacco are also carcinogenic and can contribute to increased risk of oral cancer [5]. High risk genotypes of the human papillomavirus (HPV) family as well as

human herpes viruses are also strongly correlated with an increased probability of the occurrence of these cancers [6, 7]. Other environmental factors have been shown to influence the incidence of HN malignancies such as poor oral hygiene [8], inhalation of atmospheric pollution [9], and exposure to man-made mineral fibers [10] and formaldehyde [11]. Dietary deficiencies and imbalances may also be associated with an increased risk [12, 13]. However, regardless of the origin of these environmental agents, they tend to be more potent in individuals with diets deficient in antioxidants and micro nutrients, typically found in fruits and vegetables [14, 15]. The exact causes of these malignancies are not sufficiently understood, and tumor size, tumor stage, nodal status, grade of tumor, performance status, site of primary, thickness, depth of invasion, and tumor margins are strong predictors of treatment success [16, 17].

## **1.2 Proton Therapy**

### **1.2.1 Background**

The medical benefits of radiation were immediately recognized after the discovery of x-rays and radioactivity in 1896. Over the last few decades, radiation therapy has evolved tremendously with the inclusion of computers. The introduction of computerized treatment planning, different treatment modalities and image guidance has aided in the creation of more complex and accurate treatment plans. Proton radiation therapy is still considered a relatively new modality even though the use of proton radiation to treat patients was first attempted in the 1950s. It was not until the late 70s that proton therapy was considered more viable for cancer treatments [18-20] and subsequently, a large increase in the number of proton radiation



therapy centers occurred after 2000. As the use proton radiation therapy became more widespread, new treatment innovations were investigated and were used clinically. Various beam delivery techniques to produce spread out Bragg peaks (SOBPs) and broad beams were established and allowed for the production of flat dose distributions with higher efficiency [21].

Similar to photons, proton therapy makes use of proton beam radiation to cause lethal damage to the DNA present in tumor cell nuclei that ultimately leads to cell death. The main goal of proton therapy is to deliver high radiation doses to tumors while maintaining healthy tissues under clinically safe dose constraints. Protons were first introduced in the attempt to improve target dose conformity and deliver lower integral doses to the patient. This dosimetric advantage originates from the physical phenomenon known as the pristine Bragg peak which is characterized by a sharp increase in dose deposition followed by a sharp fall-off.

When compared to photons, protons can help spare normal tissues by offering lower integral dose and absence of exit dose. However, the Bragg peak itself cannot deliver 100% of the prescribed dose to the whole extent of the disease. The depth in which the Bragg peak occurs is a function of the energy of the proton beam used. Therefore, a compilation of pristine Bragg peaks of varying energies can be used to form what is known as Spread Out Bragg Peak (SOBP). The superposition of different monenergetic beams allows for better spatial coverage of the target with the limitation of increasing the entrance dose.

## **1.2.2 Proton Therapy Main Applications**

The majority of cancer patients today receive multi-modality treatments, including surgery, chemotherapy and radiation therapy, where approximately 40% of all patients receive radiation therapy at some point during the course of their treatment. Proton therapy specifically is heavily used for the treatments of prostate cancer (70% of all cancer patients treated with protons in the US), breast, lung, brain, liver and head and neck malignancies [22]. Another important application of proton therapy is with regards to pediatric tumors. Children are at higher risk of developing secondary malignancies [23]. They are also more susceptible to radiation effects in organ growth and function, causing significant impact on their future health [24]. Risk for growth abnormalities and the development of subsequent carcinomas can be minimized with the lower integral dose achieved with proton therapy.

For HN cancer specifically, concurrent radiation therapy and chemotherapy has been shown in randomized trials to improve survival, compared with either radiation therapy or chemotherapy alone [25]. The value of protons in head and neck disease sites originates from the ability to minimize the dose to the large number of critical structures surrounding or adjacent to the target, such as the brainstem, optic structures, mandible and teeth, parotids, oral cavity, esophagus, larynx, and spinal cord. The complexity of head and neck cancer is due not only to the large concentration of organs at risk (OAR), but also to the large extent and involvement of these malignancies. Proton therapy has been shown to be analogous to photon therapy for the treatment of HN tumors while resulting in fewer normal tissue complications improving the quality of life for the proton therapy patients [26].

### **1.2.3 Head and Neck Proton Treatments**

One of the reasons why the head and neck region is particularly difficult to treat with radiation is because of the presence of tissue heterogeneities. The area is not only irregularly shaped but also composed of several different types of materials, such as air, tissue, muscle, blood vessels, saliva, bony structures, etc. The large presence of interfaces can be difficult to account for accurately in treatment planning systems thus leading to inaccuracies in the dose calculation and dose distributions. In addition, the area allows for motion that can significantly alter the range of the protons beams used in the treatment. Aside from regular breathing, patients can swallow, cough, move their tongue inside their mouths or change their neck flexion during the treatment. These small changes in the beam path could lead to proton range changes of up to several millimeters [27], which can cause substantial variations in target and OARs doses [28]. In order to avoid this potential harm to the patient, specific immobilization equipment must be used in the treatment process.

A wide variety of patient specific devices are available to help immobilize the patient in a repeatable and comfortable position. Specifically for head and neck, thermoplastic masks, head molds, and vacuum assisted bite blocks are widely employed in the clinic. The thermoplastic mask and head mold are screwed into the couch and can be seen in Figure 1. Similar to the head mask and head mold, the bite blocks are used in most treatment and help maintain the tongue immobile and away from the target volume.

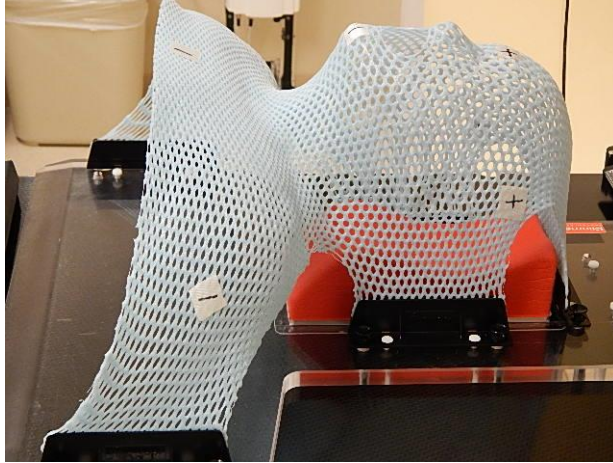


**Figure 1. The thermoplastic mask and head mold and screwed into treatment couch.**

The selection of these devices involves more than just trying to limit deviations in the position of the target and healthy tissues. It is important to also consider the impact of these devices in the proton beam range. Therefore, low-density materials are used and properly accounted for in the treatment plan dose calculation by including them in the CT simulation of the patient. Proton treatments are particularly sensitive to changes in patient positioning, variations in internal anatomy, and interference from immobilization devices. Therefore, comfortable and near-tissue equivalent immobilization hardware, quality planning CT simulations and consistent deliveries are of great importance in order to achieve successful proton head and neck treatments.

## 1.2.4 Proton Tissue Equivalent Materials

Photon dose calculations rely on the conversion of the material's electron density to Hounsfield units (HU). In contrast, proton dose calculations depend on the material's stopping power to describe the particle's energy lost through the medium. Therefore, materials that can be considered tissue equivalent in a photon beam may not necessarily be proton tissue equivalent. Hence, calibration curves that convert HU to relative linear stopping power (RLSP) need to be created while commissioning a treatment planning system. These calibrations need to be specific for each CT scanner and technique used [29]. Materials with a RLSP that is within 5% of the tissue equivalent HU-RLSP curve in Figure 2 are considered suitable for proton therapy [30].

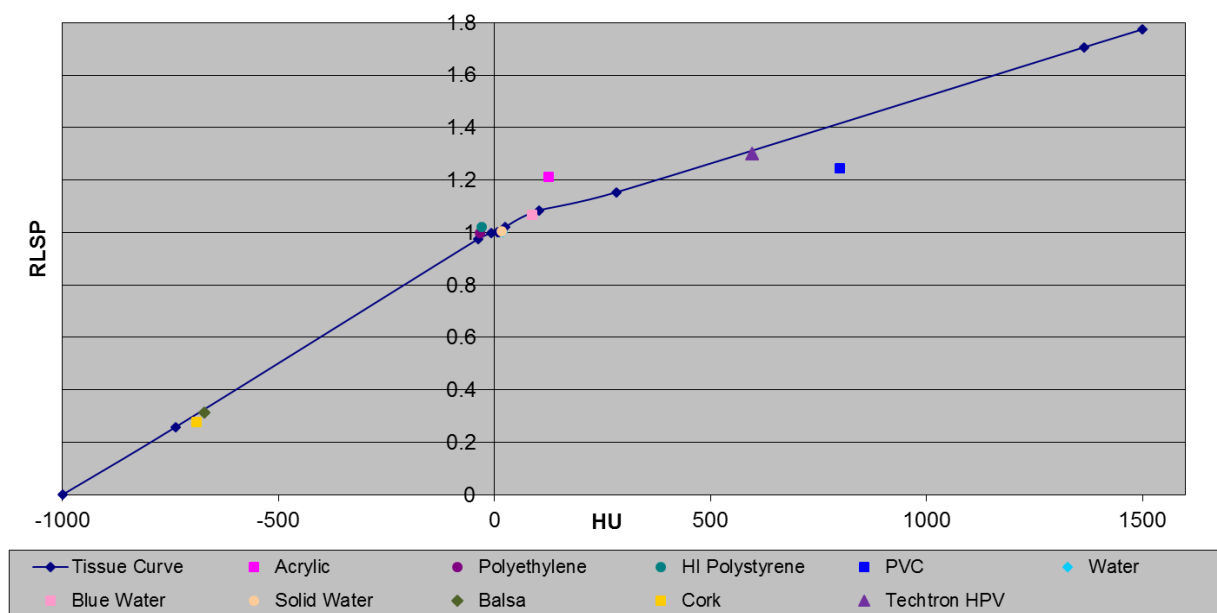


**Figure 2: Hounsfield Units versus Relative Linear Stopping Power calibration curve**

One possible way of creating a calibration curve is based on CT measurements, however it is not the most reliable method. HU measurements have a general uncertainty of up to 3%

[31], and depend on the scanner, scan protocol and matrix size used [32]. Another source of error in this method is the approximation of real tissue with tissue substitutes. The chemical composition of real tissue cannot be properly represented in tissue substitutes, resulting in significant differences in RLSP and HU. Therefore the widely adopted procedure in the proton community to perform the RLSP and HU calibration is the stoichiometric method. This “virtual” calibration is based on real tissues and can be created by calculating the material’s HU and RLSP using both their chemical composition and measured HU [29].

An accurate representation of patient geometry, heterogeneity map, and material composition are crucial when trying to fully exploit the advantages of proton therapy. Uncertainties in the RLSP to HU conversion can be translated into uncertainties in the proton beam range, thus it is essential to attempt to minimize these uncertainties. Ideally a direct measurement of the RLSP using proton CT would be used in treatment planning systems, however that technology is not yet fully developed. Therefore, the stoichiometric method needs to be evaluated for its own uncertainties. Some of them can be related to the inherent uncertainties of the CT imaging process, determination of physical parameters in the stoichiometric formula, mean excitation energies and the assumption of RLSP being constant across all proton energies [33].

### **1.3 CT Imaging and Artifacts**

Computed Tomography (CT) imaging combines a series of x-ray measurements taken at different angles to produce 3D images of scanned objects. Most CT scanners complete full 360 degree rotations of the gantry in order to collect the data. The x-ray tube and detector are

placed inside a large housing that serves to protect the patients from all the fast moving parts. Modern CT scanners use a continuous output x-ray source that spans the length of the detector array. Recent generation scanners have the arrangement of the detectors aligned on an arc relative to the x-ray tube so that there is very little difference in photon fluence to the detectors, due to inverse square law, and so that the photons strike normal to the detector's surface, minimizing lateral positioning errors (Figure 3) [34]. The raw data acquired is usually reconstructed into a series of axial CT image slices. Each axial image slice is 2D and can be arranged together to form the full 3D CT image of the object being imaged.

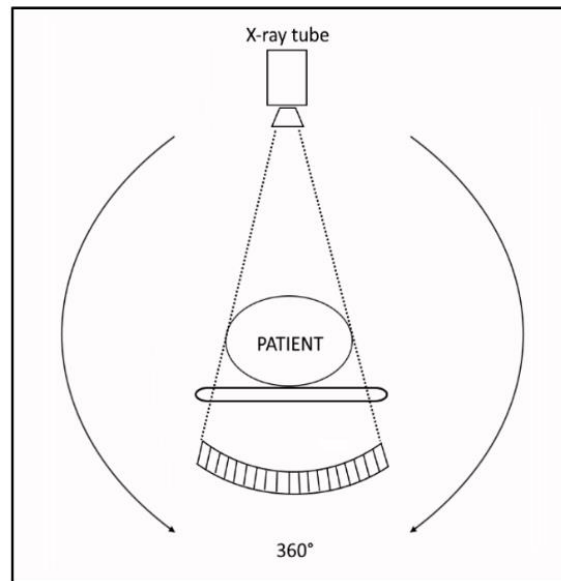


**Figure 3: Diagram illustrating the x-ray fan beam striking the arc of detectors.**

CT artifacts are systematic discrepancies between the HU represented in the reconstructed image and the true HU from the accurate attenuation coefficients of the object. CT imaging artifacts can originate from partial volume effects, aliasing, undersampling in the cone beam direction, and the presence of high density objects in the scan field. Dense objects, such as bone and metal, cause common issues in the reconstruction of the CT images.

Beam hardening is an example of a type of artifact caused by the presence of high atomic number materials in the CT bore. Bone and metal cause the lower energies of the spectrum to be preferentially attenuated when compared to higher energy, leading the beam to become “harder”, i.e. a higher energy than normal. Reconstruction algorithms apply a correction function to correct for beam hardening [35], but are optimized for human tissues and therefore cannot fully rectify the high density materials. Highly attenuating materials also causes the exiting x-rays to have a low photon flux and therefore can lead to photon starvation on the detectors reducing the quality of the image. The combination of beam hardening and photon starvation produces streaking artifacts in the reconstruction and can affect the image severely. Figure 4 shows examples of severe metal artifacts in head and neck patients.

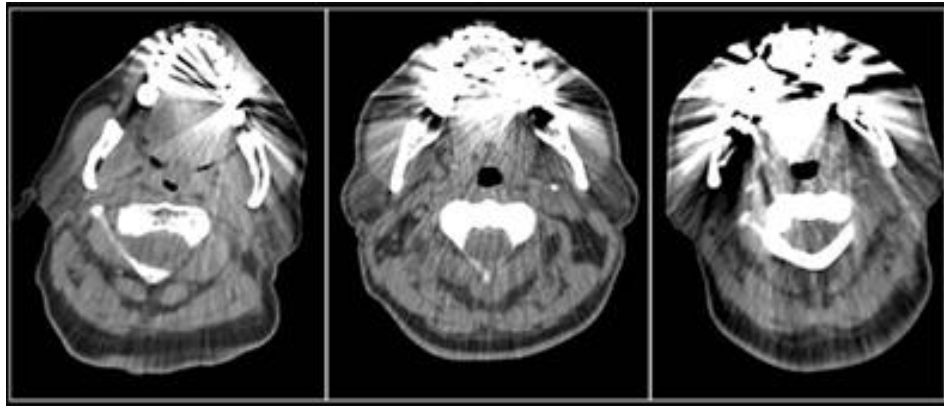


**Figure 4: Artifacts caused by metallic dental fillings in Head and Neck patients.**

### **1.3.1 CT Metal Artifacts in Proton Therapy**

Modern proton therapy has the ability to offer highly conformal dose distributions to targets while sparing surrounding healthy tissue. Therefore, it is exceptionally important to precisely identify and define the planning target volume (PTV) and OARs in patients. Imaging



artifacts can pose a problem for physicians when completing a diagnosis or attempting to delineate the extent of disease. The most common artifacts present in head and neck cases are the ones caused by the presence of high atomic number materials in the image, such as metal implants and dental amalgams, often found in dental fillings.

Dental filling metal amalgam artifacts can obscure the visualization of tumors and normal tissues in the oral cavity and oropharynx. This obscurity can lead to the improper contouring of the disease site and therefore cause incorrect dose coverage of the tumor that might result in an underdosing of the target. Aside from the difficulty in visualization of the target volumes and definition of PTV and OARs, metal artifacts will alter the true HU in the affected pixels. In photon therapy, the streaking caused by metal artifacts is less of a problem because they cause relatively small inaccuracies in the dose distribution predicted by the treatment planning system, largely because photons are exponentially attenuated with depth. Proton dose calculations in contrast, rely rigorously on the accurate representation of the HU values so that the correct RLSP is predicted [36]. Therefore, proton treatment plans could display erroneous beam ranges and dose distributions when artifacts are present and severe.

Our proton center dosimetry department has estimated that nearly 100% of the head and neck cases present with metal dental fillings that interfere with the treatment plan, possibly due to the older age range of the diagnosed patient population. Studies have shown that the presence of dental artifacts can in fact increase the interobserver contouring variability of head and neck tumors [37]. In addition, dosimetric comparisons have also demonstrated increased dose heterogeneity and reduced target dose coverage due to the presence of these artifacts [38, 39]. Several commercial solutions for metal artifact reduction have been proposed, but they can still provide inaccurate HU information, produce additional streaking artifacts, or require

extensive computation time, thus being clinically prohibitive and hence are not widely adopted.

### **1.3.2 Potential Solutions Available**

Metal dental fillings pose a challenge to head and neck radiation treatment planning, especially in proton therapy due to the extraordinary dependency on accurate HU to stopping power conversions. Several solutions have been proposed to try to help minimize the perturbations in the dose calculations produced by severe metal artifacts. However, many of these solutions only provide partial improvement and can be more costly and inconvenient for patients.

One potential solution could be the use of magnetic resonance imaging (MRI). Nevertheless, MRI is more costly and may not be suitable for all patients, such as those with pacemakers and metal prosthesis/implants. MRI is not artifact free and therefore different distortions may be introduced to the images. In addition, MRI images do not provide the HU information necessary for proton radiation treatment planning.

Newhauser et al investigated streak related range errors and whether they could be avoided using mega voltage (MV) CT images in the treatment planning. They accomplished a significant range uncertainty improvement, from 5-12 mm using uncorrected kVCT to 3 mm or less using MVCT. However, it is not known whether MVCT images can be used in proton treatment planning. Hence, using a combination of kVCT, for better image quality, and MVCT, for reduced proton range error, was the optimal approach in their study [40]. However, this study was only performed for proton delivery of the pelvis area and has not

been evaluated for other disease sites. In addition, further investigations need to be completed to determine the suitability of the approach for clinical use.

Replacing the metal amalgam with a radiologically inert composite material is also an available option. Composite fillings have been shown to demonstrate comparable HU ranges relative to native teeth [41]. Nonetheless, filling replacements can take approximately 1 hour per tooth and the cost and insurance coverage are not exactly determined. Hence, replacing fillings may seem relatively simple, but it requires additional time for dentist visits and may be inconvenient or costly for some patients.

A solution that has gained popularity in recent years is the use of dual energy CT. The acquisition of two different X-ray energy spectra can be used to generate virtually monochromatic attenuation information. This allows for the reconstruction of images theoretically free of beam hardening effects which, as discussed before, are a large component of CT metal artifacts. However, this alternative only addresses the beam hardening component of metal artifacts. Photon starvation and scatter remain an issue and often dampen the success of the algorithms. Studies have reported a reduction in metal artifacts with the use of dual energy CT algorithms but with a compromise in image quality through the introduction of new streaks and a reduction in Contrast to Noise Ratio.

Current common practice includes the use of overriding techniques and of various commercial metal artifact reduction (MAR) algorithms. Overriding HU for known or expected values in CT images is both time-consuming and very subjective, factors which can be eliminated with automated approaches such as available algorithms. However, a recent study focusing on three current commercially available methods has concluded that they were

generally not successful at reducing artifacts specifically caused by dental fillings [42]. Other post-processing metal artifact reduction algorithms have been published but have not found clinical acceptance [43-45]. Despite the practicality and availability of vendor specific algorithms in all clinics, MAR algorithms are not widely used. Most physics teams hesitate to recommend their vendor's MAR solutions due to lack of knowledge of how they affect treatment planning dose distributions and hence, resort to manual overrides of tissue and metal.

## **1.4 Specific Problem**

There is still an evident need for better metal artifact management in highly heterogeneous sites, such as head and neck. Despite several publications of metal artifact reduction algorithms over the last two decades, studies of their effectiveness in proton treatment planning are limited [22]. The impact of dental artifacts on head and neck treatments has been investigated in photon therapy [38] but not extensively in proton therapy. There are some proton studies that have evaluated dosimetric effects and the accuracy in proton range calculations due to hip prostheses' artifacts [46, 47], but little has been done for proton head and neck artifact cases. Dose calculations on highly heterogeneous sites can pose an extraordinarily difficult task due to the large number of sharp transitions between low and high attenuation materials [48].

The vast majority of MAR algorithms involve the manipulation of the raw CT projection data through the identification of corrupted projections followed by its replacement with interpolated data. The success of this method is highly dependent on the precision of the

estimation of the removed data. Several interpolation and filtering approaches have been investigated in literature [49-51]. The importance of this step is demonstrated by the sharp transitions between the original projections and the interpolated projections, which can generate new artifacts. In addition, data loss near the metal edges cannot be recovered and can result in blurring. Head and neck patients present with dental fillings of varying shapes and locations, creating a difficult challenge to these algorithms to completely eliminate the streaking and blurring in the images.

The technique described in this work is an innovative solution as it is not based on direct interpolation methods and therefore does not require the removal and replacement of the missing data by estimated (and not necessarily correct) data, possibly causing additional artifacts. In addition, the methodology developed here is not system specific and therefore is available to any CT scanner that allows for gantry tilts. The goal of this work is to introduce, test and compare the Artifact Management for Proton Planning (AMPP) algorithm developed on a geometrical phantom, and perform a quantitative image quality analysis by comparing it to major vendors' commercially available approaches. In addition, a proton treatment planning dosimetric exercise was performed to investigate the effectiveness of the algorithm in improving dose calculations.

## ***Chapter 2 - Hypothesis and Specific Aims***

### **2.1 Central Hypothesis**

The central hypothesis is that a CT artifact management technique can be developed for Head and Neck proton therapy delivery that will reduce dental induced artifacts posterior to the oral cavity better than current clinical artifact reduction techniques as measured by an improvement in the visualization of the targets and OARs and, accuracy of the delivered proton dose distribution.

### **2.2 Specific Aims**

#### **2.2.1 Specific Aim 1: Algorithm Development**

**Aim 1:** Develop a MAR algorithm using CT gantry tilts and test it on a geometrical phantom that will contain removable metal implants, such as dental amalgam fillings, and tissue equivalent materials. In addition, a comparison to a clinical commercial algorithm will be performed.

Working hypothesis: *an artifact reduction algorithm can be developed using CT gantry tilts and can be successfully evaluated as a proof of principle. In addition to being an accurate and effective MAR algorithm, the technique developed in this work will outperform a current clinical solution.*

### 2.2.2 Specific Aim 2: Image Quality Analysis

**Aim 2:** Build an anthropomorphic Head and Neck phantom and perform an image quality analysis of AMPP by comparing it to major vendors' commercially available solutions. Parallel to the geometrical phantom, the anthropomorphic phantom will contain removable metal amalgam implants that will allow for scans with and without metal artifacts.

Working hypothesis: *an anthropomorphic phantom can be designed that will mimic human structures and disease with tissue equivalent materials for a generalized head and neck cancer. The algorithm developed in this work will outperform current vendor solutions showing improved percent of bad pixels and HU differences.*

### 2.2.3 Specific Aim 3: Proton Dosimetric Analysis

**Aim 3:** Perform a treatment planning dosimetric analysis comparing proton dose distribution differences when a plan designed on a baseline image set (CT without metal artifacts) and is copied to different MAR image sets, without beam reoptimization.

Working hypothesis: *the AMPP MAR solution will provide the most optimal image set to use in proton treatment planning.*

## ***Chapter 3 - Specific Aim 1***

### ***Development of a stereoscopic CT metal artifact management algorithm using gantry angle tilts for head and neck patients***

#### **3.1 Introduction**

Computed tomography (CT) imaging artifacts are discrepancies between true Hounsfield unit (HU) values and those that are displayed. These can pose a problem for physicians who are completing a diagnosis or attempting to identify or delineate the extent of disease. In the reconstruction of the CT images, dense objects such as bone and metal are a common source of artifacts through beam hardening and photon starvation. Beam hardening is caused by the presence of dense (and high atomic number) structures in the beam path. The x-ray spectrum undergoes an upward shift in average energy due to the preferential attenuation of lower-energy photons. CT reconstruction algorithms attempt to correct for beam hardening but are optimized for human tissues and cannot fully address highly attenuating materials such as metals [1]. Photon starvation occurs when these highly attenuating materials cause the exiting x-rays to have a low photon flux on the detectors. Consequently, the combination of



beam hardening and photon starvation produces streaking artifacts in the reconstruction and can affect the image severely.

The most common artifacts present in head and neck (HN) cancer patients are the ones caused by the presence of high atomic number materials in the image, such as dental amalgams. Dental filling metal amalgam artifacts can obscure the visualization of tumors in the oral cavity and oropharynx. This obscuring of the anatomy can lead to poor visualization of tissues and therefore improper definition of the target, potentially providing suboptimal management of the disease, particularly including radiotherapy quality. Studies have shown that the presence of dental artifacts can in fact increase the inter-observer contouring variability of HN tumors [2]. Aside from the difficulty in visualization of tumors and in definition of planning target volumes and organs at risk (OARs), metal artifacts will alter the true HU values in the affected voxels which negatively impacts the quality of radiotherapy in such areas. Kim et al. and Mail et al. have demonstrated that such artifacts result in increased dose heterogeneity and reduced target coverage [3, 4]. In photon therapy, calculation errors were found to be as high as 12% when fillings are present, compared with 3% when no metal was present [5]. The consequences for dose calculation accuracy are also particularly relevant in proton therapy because of the strong dependency between a correct relative linear stopping power prediction and accurate representation of HU values [6-9]. Proton treatment plans could display erroneous beam ranges and dose distributions when artifacts are present.

Several solutions for metal artifact reduction have been proposed, but many are impractical or not clinically feasible and therefore are not extensively adopted. Newhauser et al. accomplished a significant range uncertainty improvement in proton treatment planning

with the use of megavoltage (MVCT) CT images. However, it is not known whether MVCT images can be used in treatment planning and their study was only performed for proton delivery of the pelvis area and has not been evaluated for other disease sites. Kim et al. recently published a post processing technique that requires an additional CT scan to obtain complementary image data to help reduce metal artifacts on the original scan [10]. However, the success of their technique can be highly sensitive to noise and the severity of artifacts present. Replacing the metal amalgam in dental fillings with a radiologically inert composite material is also an available option. Composite fillings have been shown to demonstrate comparable HU ranges relative to native teeth [11]. Nonetheless, filling replacements can take approximately 1 hour per tooth, and the cost and insurance coverage are not exactly determined, limiting the applicability of this technique. Current common practice to help manage metal artifacts includes the use of overriding techniques and of various metal artifact reduction algorithms. Overriding HU values in HN patients is the process in which dental fillings and their artifacts are identified, contoured and assigned an expected HU value to be used in the dose calculation algorithms. Overriding HU for known or expected values in CT images is both time-consuming and subjective, factors which can be eliminated with automated approaches such as available algorithms. The majority of current artifact reduction approaches involve algorithms that manipulate the raw projection data [12-15] and can generally be divided into 2 groups: iterative reconstruction algorithms and projection completions methods. The former approach starts from an initial guess image, re-projects the image to the sinogram space, compares it to the original projections to generate a correction, applies that correction and repeats that process until the difference between the images is minimized. This approach is superior at handling metal artifacts but it requires

extensive computation time, making the technique clinically unfeasible. The latter approach works by replacing the corrupted projections in the sinogram space with interpolated data from regions of the sinogram unaffected by the metal. The estimation of the missing raw data values will determine how successful the algorithm is. Sharp transitions between the original projections and the interpolated ones cause additional artifacts. Moreover, the estimation of raw data values creates blurring in the final image due to data loss near the metal edges, which is not recoverable through the estimation of values. Despite the creation of additional artifacts and direct interpolation of HU information, projection completion methods gained more popularity. However, a recent study of three current commercially available artifact reduction methods concluded that they were generally not successful at reducing artifacts specifically caused by dental fillings [16]. Indeed, particularly for dental artifacts, that study found that the commercial solutions had either a minimal effect or actually made the artifacts worse. Other post-processing metal artifact reduction algorithms have been published but have not found clinical acceptance [17-19].

Despite several publications of metal artifact reduction algorithms over the past two decades, there remains an evident need for better metal artifact management in highly heterogeneous sites, such as the HN [5, 16, 20]. To address the need for better metal artifact management, we developed an algorithm that is not based on direct interpolation methods and therefore will not require the removal, replacement, and consequential loss of data points. In addition, the algorithm will not be system specific and thus could be used with any CT scanner that allows for gantry tilts, which is a feature offered on scanners from all major CT manufacturers. In this work, we will introduce the artifact management algorithm and

provide testing on a geometrical phantom as a proof of principle. An initial clinical comparison to a vendor's current algorithm solution will also be presented.

## 3.2 Materials and methods

### 3.2.1 Algorithm

Similar to the concept of stereoscopic imaging, the algorithm developed in this work makes use of two angled CT scans to generate one artifact-reduced image set. The issue with traditional  $0^\circ$  degree scans on patients with HN disease who have dental fillings or implants is that the artifact-compromised slices are located where typical HN disease is located (Figure 5), posterior to the oral cavity.

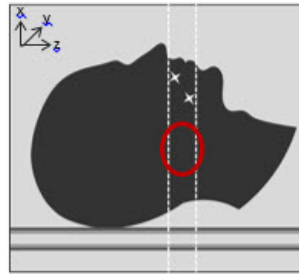


***Figure 5: Diagram representing a patient with HN disease with the range of CT slices affected by the dental work. The red circle shows the region of typical HN disease that gets affected by artifacts resulting from metal in the mouth.***

The goal of this algorithm was to use two angled CT scans to reconstruct an image where the posterior region can display the accurate HU information without the need for the widely used metal thresholding/deletion and interpolation techniques. In simple terms, the reconstruction technique is performed in the image space and is based on the combination of the superior portion of a superiorly tilted scan with the inferior portion of an inferiorly tilted

scan, as shown in Figure 6. The imaging technique and reconstruction algorithm create an image with the actual (not interpolated) HU information present in the posterior region of the patient's CT image. In order to remove the artifacts from the posterior region, the artifacts are focused on the anterior portion of the head. In other words, the artifacts now occupy previously unaffected regions such as the nose and chin, as it can be seen in Figure 6(c). This trade-off was made because disease and OARs typically are not located in those regions; the most common primary presentations of head and neck disease are the oropharynx and base of tongue. In the event of predominantly anterior disease, such as lip cancer, this trade-off would likely not be appropriate and this approach may not be viable. However neoplasms arising in the nasal cavity and oral cavity are fairly uncommon, accounting for less than 1% and 2% of all HN cases in the United States respectively [21].

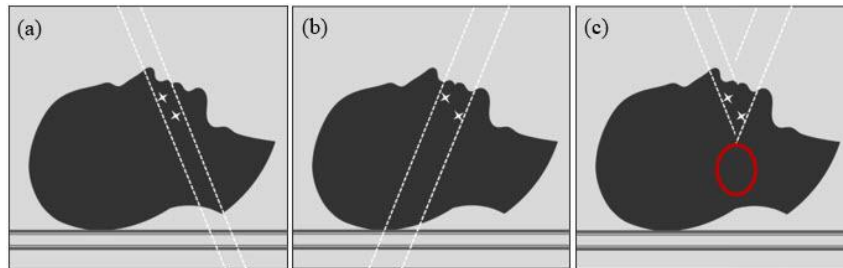


**Figure 6: Diagram of a sagittal view of a HN patient with the CT gantry tilted superiorly (a) and inferiorly (b) showing the artifact-affected slices. In the final artifact-reduced image (c), the posterior region (red circle) is clear, and the artifacts are focused on the anterior region.**

The framework for our new algorithm is divided into two main steps and can be found in Appendix A. Step 1 is responsible for untilting the images that were acquired at an angle, so that they appear as regular axial slices and can then be used in step 2. Step 2 uses those

untitled images to form an image with the metal artifacts greatly reduced. The complete artifact reduction routine depends on the number of images per scan but on average takes less than 1 minute to complete.

### 3.2.2 Step 1: Untilting of image set

Step 1 was accomplished by performing 3-D affine geometric transformations to the entire image volume. Affine transformations are done using linear mapping functions that preserve specific points, straight lines, and planes. After affine transformations, sets of parallel lines remain parallel, making them suitable for this part of the algorithm. In order to achieve such transformations, the algorithm performed a matrix multiplication with specific shear factors that were previously determined based on the angle of tilt of the gantry. The general form of this transformation is given by:

$$I = M \times I'$$

Where M is the geometric transformation matrix, I' the input image set, and I the final transformed image set:

$$I = \begin{bmatrix} x \\ y \\ z \\ 1 \end{bmatrix}, \quad M = \begin{bmatrix} 1 & sh_{yx} & sh_{zx} & 0 \\ sh_{xy} & 1 & sh_{zy} & 0 \\ sh_{xz} & sh_{yz} & 1 & 0 \\ 0 & 0 & 0 & 1 \end{bmatrix}, \quad I' = \begin{bmatrix} x' \\ y' \\ z' \\ 1 \end{bmatrix}$$

The first affine transformation was a shear transformation, and it was applied on the sagittal plane so that the tilted image volume could be resampled into the typical axial orientation. In order for that to happen, all shear factors in the shear transformation matrix M were set to 0, except  $sh_{zy}$ . This factor determined the amount of shearing the image needed across the y-axis and therefore was directly related to the CT gantry angle in which the

image was acquired. The resampling of the tilted slices required an interpolation because of the possibility of the voxels being moved off the grid points while untilting the image set, and for this project, we used a linear interpolation. The second affine transformation performed on the image was a scaling transformation. Similar to the matrix multiplication done for the shearing transformation, the scaling was performed by applying the appropriate factors on the M matrix (Table 1), which were determined empirically to provide the best match between the reconstructed and baseline images. CT images acquired at an angle are elongated on the y-axis and therefore need a correction along that direction. For our setup, appropriate scaling was obtained when all elements of the identity matrix M were set to 0 except the position  $M_{2,2}$ , which scales the y-axis. This process was completed for the superior and inferior tilted images so that the new transformed image sets were then displayed as traditional axial slices and could be used in step 2.

<b>Angle</b>	<b>Shear Factor</b>	<b>Scaling Factor</b>
<b>5°</b>	0.019	0.999
<b>10°</b>	0.041	0.989
<b>15°</b>	0.060	0.965
<b>20°</b>	0.078	0.945
<b>25°</b>	0.092	0.905
<b>30°</b>	0.108	0.871

*Table 1: Shear and scaling factors used in the affine transformations.*

### **3.2.3 Step 2: Correction of metal artifact**

The superior and inferior modified image sets from step 1 were used to reconstruct the final artifact-reduced image. On each image set, this portion of the algorithm searched axially through each pixel, starting at the superior-most slice, until it found the first metal thresholded pixel. That slice number was saved, and the same process was performed in opposite order starting from the inferior-most slice. This repetition was done to determine the first and last slices on which artifacts were present. The number of slices with artifacts is dependent on the size of the implants and slice thickness, but for this phantom, the images contained approximately 2.0 cm (in the superior-inferior direction) of artifact-affected slices. Once those were identified, a center slice (in the center of the artifact-affected slices) was determined by averaging the first and last slice numbers previously determined and used as the reference slice for that particular image set. The artifact-free slices were selected in each image set, up to the reference slice (for instance, the superior slices up to the reference slice in the superiorly tilted image set and the inferior slices up to the reference slice in the inferiorly tilted image set). Finally, the artifact-free slices were merged as shown in Figure 6(c), and the final artifact-reduced image was formed. In addition, the metadata in the final untilted image volume created required a correction. The reconstructed images were still assigned an angled metadata tag and had to be corrected in order to be properly displayed in the imaging software and treatment planning systems.

### **3.2.4 Evaluation**

The routine described in the previous section was tested on a geometrical phantom simulating a HN cancer patient with dental fillings. The phantom was composed of high-



impact polystyrene and was divided into two halves representing an upper and lower human jaw so that teeth structures could be inserted [

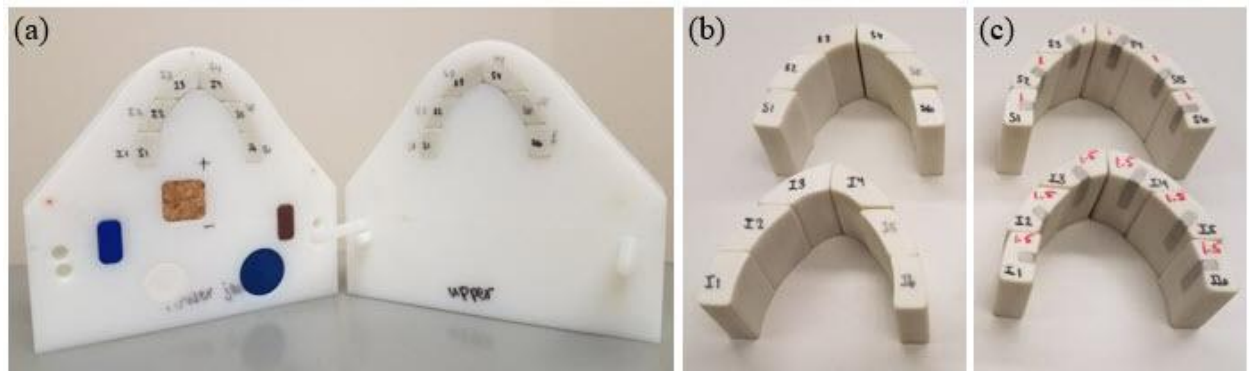


**Figure 7(a)**. The tooth structures were made of Gammex 450 cortical bone substitute (Middleton, WI). Two sets of teeth were used in the evaluation of the algorithm. The first one was used as the baseline and contained only the cortical bone material in order to obtain the artifact-free image set [

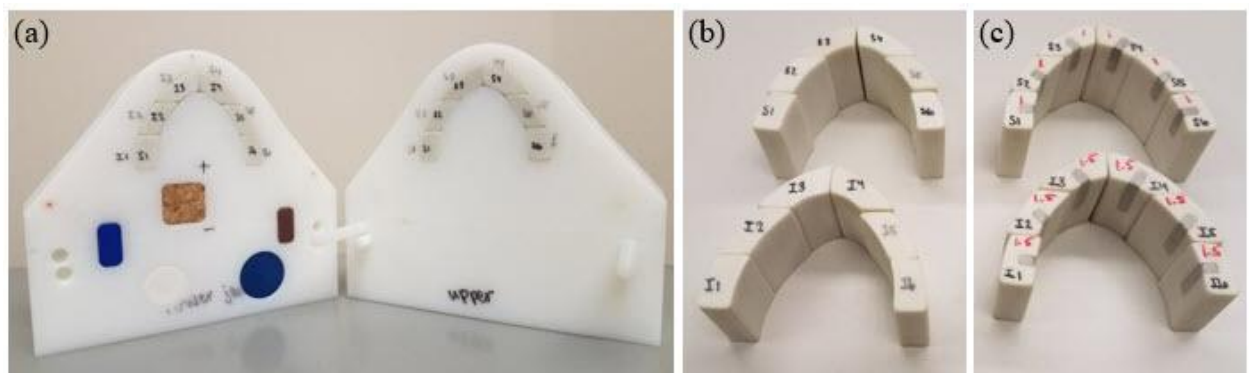


**Figure 7(b)].** The second set was modified to contain Dispersalloy (Dentsply, Milford, DE) dental amalgam (physical density =  $9.6 \text{ g/cm}^3$ ), as seen in

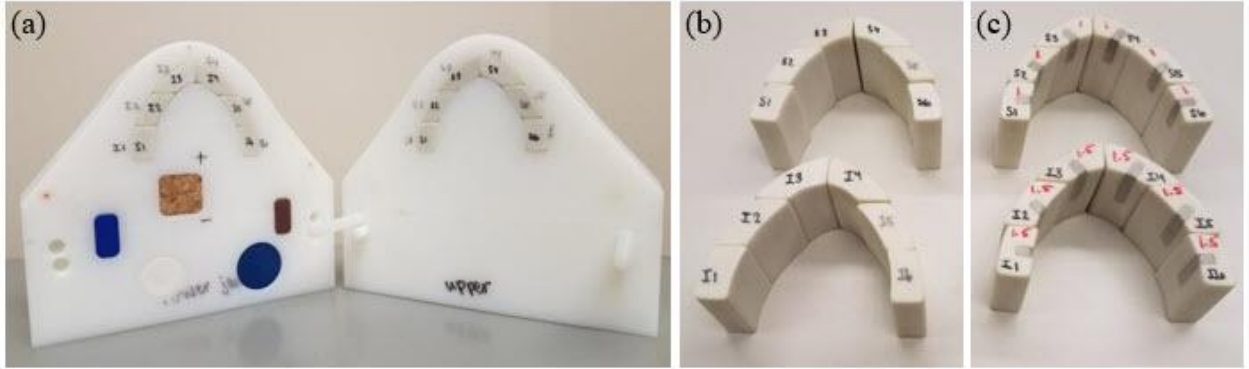


**Figure 7(c).** The general configuration and size of the dental fillings inserted in the modified set were determined by a dentist. The phantom was  $15 \times 13.5 \times 8 \text{ cm}$ , and each tooth was approximately 3 cm long. The modified set of teeth contains 1.5 cm long metal amalgam fillings.

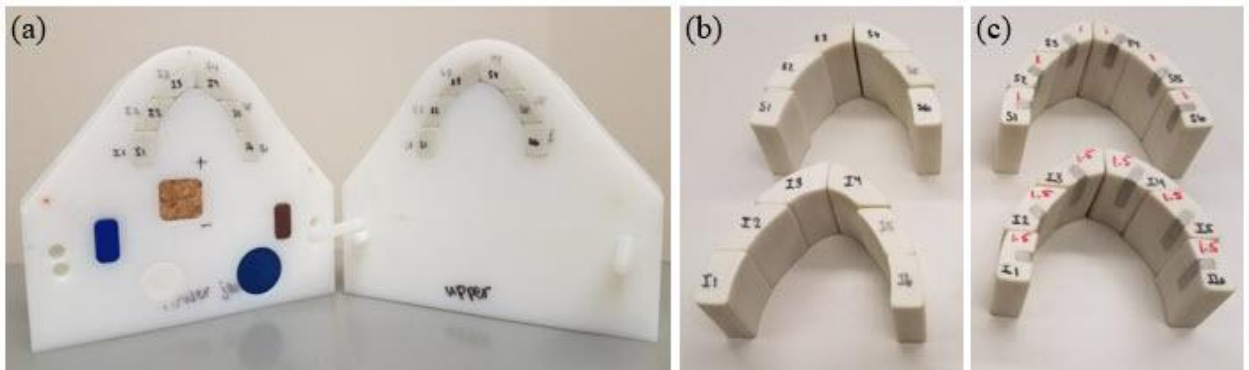


**Figure 7: Both halves of the geometrical phantom (a) and the tooth structures without (b) and with (c) metal amalgam fillings used in the testing of the algorithm.**

The geometrical phantom also contained plugs of different materials located posterior to the teeth set; these materials were selected to span the range of HU values seen in images of HN patients. These plugs were two lateral rectangles made of solid water ( $1 \times 2$

$\times 2$  cm, physical density =  $1.04 \text{ g/cm}^3$ ; CNMC, Nashville, TN) and blue water ( $1 \times 2 \times 1$  cm, physical density =  $1.09 \text{ g/cm}^3$ ; Gammex, Middleton, WI), two cylinders made of polybutylene terephthalate (PBT) (diameter:  $2.5 \times 1$  cm, physical density =  $1.31 \text{ g/cm}^3$ ; Gammex, Middleton, WI) and Techtron HPV bearing grade (diameter:  $2 \times 1$  cm, physical density =  $1.430 \text{ g/cm}^3$ ; Gammex, Middleton, WI), and a cuboid made of cork ( $2 \times 2 \times 4$  cm, physical density =  $0.24 \text{ g/cm}^3$ ). The plugs were used as structures of interest in the phantom to help test the integrity of the algorithm and its ability to remove artifacts. Geometrical distortion and HU accuracy measurements were used to establish a comparison between the metal-free scan (baseline) and the reconstructed image set.

To quantify the algorithm performance, geometric distortion was evaluated through geometrical measurements of the plugs and phantom taken in the anterior-posterior (AP), left-right (LR) and superior-inferior (SI) directions. Measurements were done with the CT gantry at  $0^\circ$  with no metal teeth (baseline) and with metal amalgam (8 total metal teeth) and at the 6 gantry tilt angle reconstructions performed ( $5^\circ$ ,  $10^\circ$ ,  $15^\circ$ ,  $20^\circ$ ,  $25^\circ$ ,  $30^\circ$ ). All scans in the algorithm performance analysis were scanned on the GE Lightspeed VCT using the HN CT protocol and the parameters are listed in Table 2. To maintain consistency throughout all the measurements, the plug dimensions were obtained by measuring the full width at half maximum (FWHM) on HU profiles across the center of each plug. HU accuracy testing was done measuring fixed region of interest (ROI) sizes among the different reconstructed scans. Mean HU numbers were collected inside each plug and compared between the baseline scan and reconstructed image set with reduced artifacts. All measurements were done using Eclipse treatment planning system (version 13.6; Varian Medical Systems, Inc., Palo Alto, CA). In addition to the algorithm performance analysis, the technique developed in this

work was compared to the vendor's artifact reduction algorithm solution; SmartMAR. For that scan, the phantom was imaged with the metal teeth in place and reconstructed with SmartMAR applied. Similar to the previous analysis, geometrical and HU number measurements were obtained from the phantom's metal scan and compared to baseline images obtained from the same scanner (Table 2).

	kVp	mAs	Slice Thickness (mm)	Filter Type	Recon Kernel	Tube Rotation Time (s)
<b>Angle technique (All Angles)</b>	120	400	2.5	Medium Filter	Standard	0.8
<b>Baseline</b>	120	400	2.5	Medium Filter	Standard	0.8
<b>Metal Uncorrected</b>	120	400	2.5	Medium Filter	Standard	0.8
<b>Baseline - SmartMAR</b>	120	320	3.75	Medium Filter	Standard	1.0
<b>Metal Corrected - SmartMAR</b>	120	320	3.75	Medium Filter	Standard	1.0

*Table 2: Imaging protocols for all scans obtained.*

### 3.3 Results

#### 3.3.1 Qualitative Analysis: Artifact removal attainment

The first step of the algorithm developed in this work successfully untitled and corrected the angled CT image set. Figure 8(a) shows a sagittal screenshot of the 0° scan of the geometrical phantom with the metal teeth inserted and the artifacts created by them. As expected, the artifacts extended all the way through the posterior region of the phantom. Figure 8(b) demonstrates how the images acquired at an angle appear tilted and elongated. This particular example is a superior 25° tilt and shows the artifacts running perpendicular to the couch along the AP direction. After the first part of the algorithm was completed, the

image set [Figure 8(c)] showed the two halves of the phantom and its structures as it would be seen in the regular perpendicular scan [Figure 8(a)], except with the artifacts extending away from the HN posterior region of interest. Figure 8(d) shows the end result for the inferiorly tilted image set. It is important to notice the geometric distortion along the AP direction in the uncorrected image set [Figure 8(b)]. The uncorrected images acquired at an angle become elongated (in the AP direction only) compared with the real phantom size. Figure 8(c) and Figure 8(d) show the phantom after the algorithm was applied, corrected to normal height and untilted, which were later used to form Figure 8(e) showing the final artifact-reduced reconstructed image set.

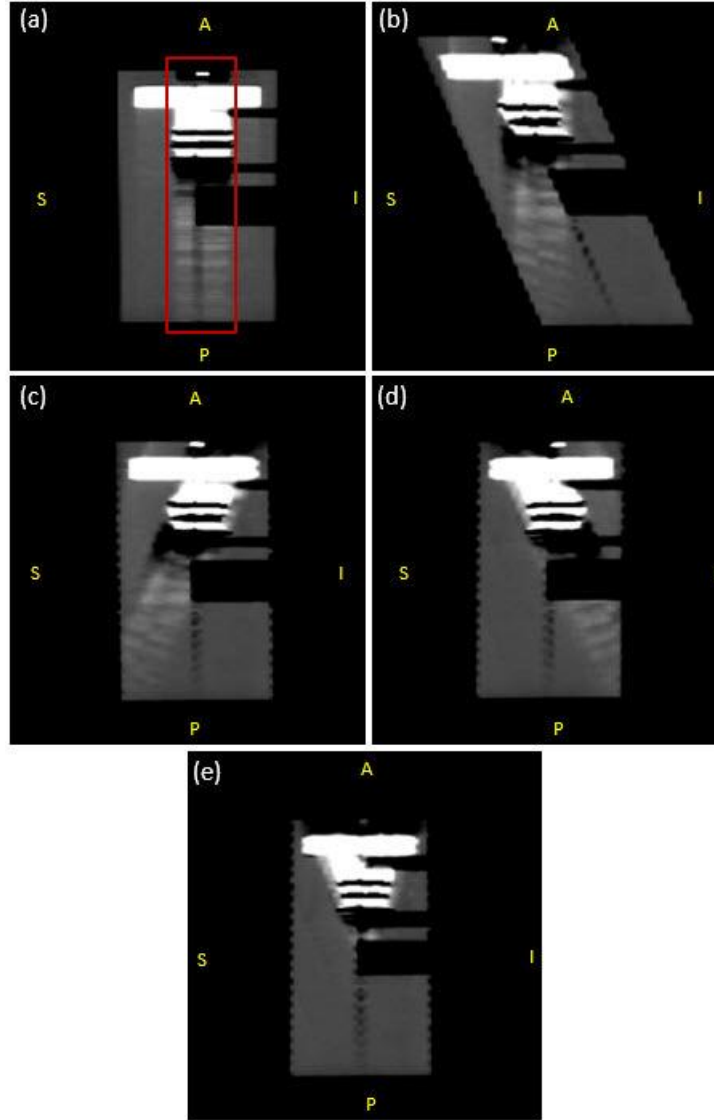


**Figure 8: (a) Sagittal view of the uncorrected image set of the geometrical phantom acquired at a  $0^\circ$  angle with metal teeth. The red box indicates artifact-affected slices. (b) Uncorrected image acquired at a  $25^\circ$  angle appearing tilted and elongated. Inferior tilted scan (c) and superior tilted scan (d) after the first part of the algorithm showing the desired typical axial appearance and corrected to normal height. Final artifact-reduced image reconstructed using (c) and (d).**

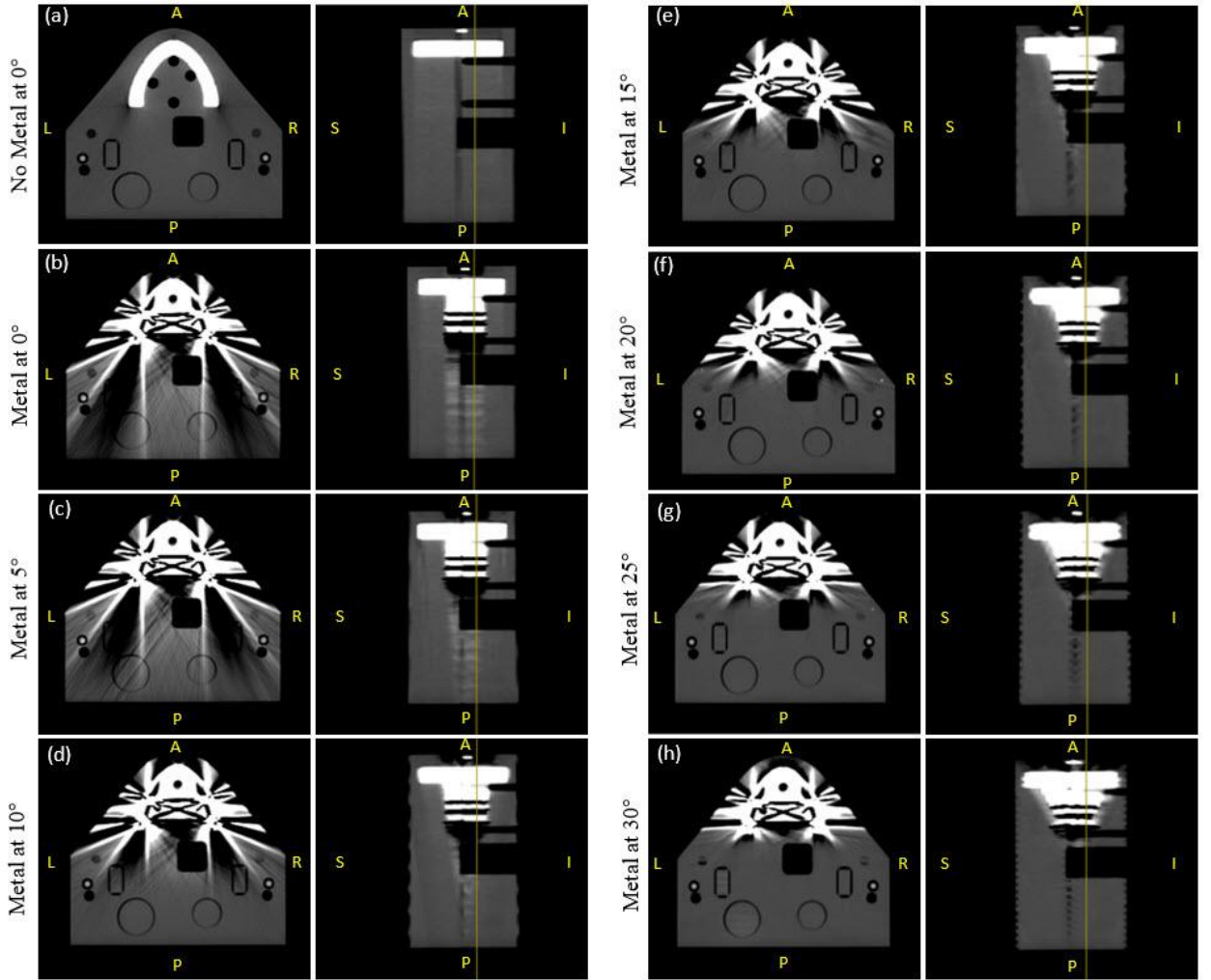


**Figure 9: Axial and sagittal views of the geometrical phantom after the complete algorithm was applied. Images show the phantom with (a) no metal at  $0^\circ$ , (b) metal at  $0^\circ$ , (c) metal at  $5^\circ$ , (d) metal at  $10^\circ$ , (e) metal at  $15^\circ$ , (f) metal at  $20^\circ$ , (g) metal at  $25^\circ$ , (h) metal.**

The metal artifact reduction step of the algorithm design was successful at managing artifacts in the posterior region of the phantom. This can be seen in Figure 9, which shows the axial and sagittal views of the geometrical phantom at the same slice location for each

CT angle examined. The vertical yellow line on each sagittal view represents the corresponding axial image. It is possible to see that as the CT gantry angle increases, the posterior region of the artifacts created by the metal amalgam becomes clearer. As mentioned in the previous section, the artifacts in the reconstructed images remained in the mouth and chin regions, which can be seen more clearly on the larger angle reconstructions.

### **3.3.2 Quantitative Analysis: Algorithm integrity analysis**

In addition to the qualitative examination of the algorithm, the distortion measurements are shown in Figure 10. Each data point represents the difference between the measurements of the plugs and phantom with the gantry at 0° with no metal teeth present (baseline) and with metal teeth present, for the six CT gantry angles. It is possible to see that there is no trend in the measurements across the different gantry angles and different directions, indicating that our artifact management algorithm will provide geometrically accurate images for any CT gantry angles used. Owing to the fact that no trend was observed, total averages were calculated for all the plugs and phantom measurements in each direction. The average total distortions for all gantry angles in the AP, LR, and SI directions were 0.17 mm, 0.12 mm, and -0.14 mm, respectively. A negative data point on the plot means that the distance measurement of the plug on the corrected image set was smaller than on the baseline image set. To test the reproducibility of the measurement technique, the standard deviation (SD) was calculated for the lowest- and highest-density sample materials: cork and Techtron HPV. For each direction, 10 FWHM measurements



were obtained and showed an average SD between the materials of 0.12 mm, 0.13 mm, and 0.33 mm for the AP, LR, and SI directions, respectively.

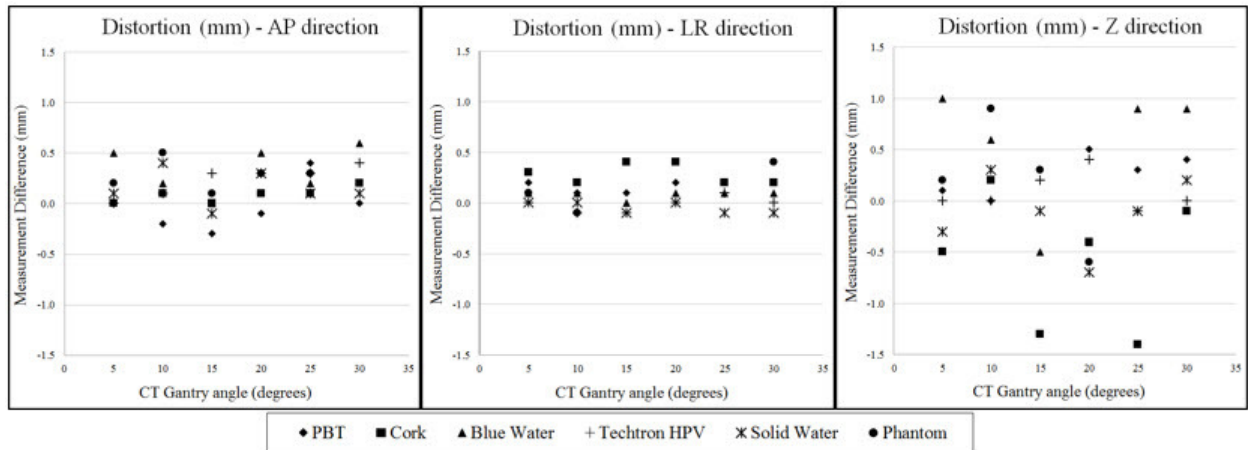


**Figure 10: Results for distortion measurements showing each difference obtained between the measurements of the different plugs and phantom done with the gantry at 0° with no metal teeth present (baseline) and with metal teeth present for the 6 different CT gantry angles in the AP (a), LR (b), and SI (c) directions.**

The measurement data for each material were fitted with a linear regression line and analyzed for statistical significance in which the dependent variable was each material in question. An  $\alpha$  level of 0.05 was used; all  $P$ -values calculated for the materials' regression lines' slopes showed no significance, indicating there was no distortion pattern related to gantry angle. The fitted slopes varied from positive to negative with very small values, ranging from -0.05 to 0.014, again indicating no trend. In addition, all regression line

intercepts included 0 in the 95% confident intervals (CIs), showing no evidence that the intercepts of the linear fit were positive or negative. The statistical analysis performed here showed that the measured geometrical distortion was random and not correlated with CT gantry angle.

The HU measurements also showed no correlation with varying gantry angles and are shown in Figure 11. Linear regression lines were also fitted for each material, and the same regression analysis was performed as described above. Similar to the distortion measurements, all of the material slopes' *P*-values were above significance level, indicating no pattern correlating HU with gantry angle tilt. Additionally, for each material, the HU values measured were statistically consistent (within the 95% CI) with the true (untitled) HU value.

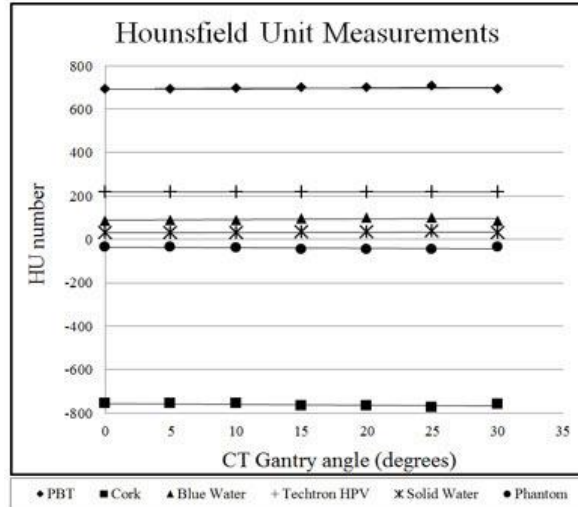


**Figure 11: Hounsfield unit (HU) measurements of all materials for the different CT gantry angles.**

### 3.3.3 Comparison with Commercial Solution

Figure 12 shows a side-by-side comparison of the same slice in the phantom after our artifact management technique and SmartMAR were applied. Qualitatively, it is possible to see that SmartMAR improves part of the streaking but creates other artifacts in the image. It is also noticeable that SmartMAR affects the entire slice in which metal is present. That is due to the algorithm being performed in the sinogram space. In contrast, our algorithm creates no additional artifacts in the posterior region and fully eliminates the streaking caused by the metal implants.

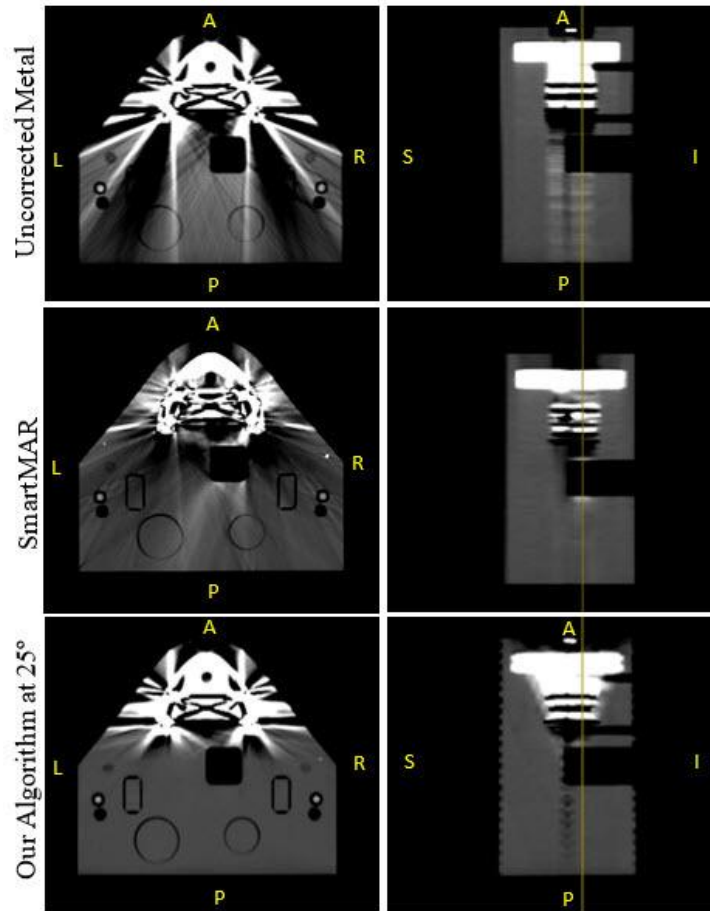


**Figure 12: Side-by-side comparison of SmartMAR and the technique developed here to the uncorrected metal scan of the phantom.**

In the quantitative comparison between both techniques, it was discovered that SmartMAR corrected images showed no relevant geometrical distortion. The average total distortions for all plugs and phantom in the AP, LR, and SI directions were very small; 0.03 mm, 0.05 mm, and -0.3 mm, respectively. Table 3 shows the HU numbers collected and their standard deviations (SD) inside the fixed ROIs for all scans. Table 4 shows the HU number differences between the relevant scans; metal uncorrected and respective baseline, and metal corrected (SmartMAR and our Technique) and respective baselines. Ideally the HU number difference should be close to 0, indicating no difference between the baseline scan and the corrected image set in question. However, the metal uncorrected scans are filled with dark and light streaks hence showing large HU differences. The streaking is also indirectly represented by the SD inside the ROIs (Table 3); the uncorrected image sets showed large variations in HU numbers, hence displaying large SD values. It is possible to notice that, for most plugs (blue water, Techtron HPV, solid water and phantom), SmartMAR provided some improvement in the HU accuracy with HU differences closer to 0 than the metal uncorrected images. However, the HU number values were still far from what they were expected to be (baseline). It is important to notice that the PBT and cork plugs' HU values were worsened by SmartMAR's algorithm. In contrast, our technique showed very small differences in HU number, indicating that the image quality in the posterior region of the phantom was nearly identical to the scan without any metal present. In addition, due to the absence of streaking in the posterior region of the phantom, the SD values collected on the scan corrected with our algorithm were much smaller than SmartMAR's and comparable to the baseline values (Table 3).

**Structure**

**HU number Mean**

	Baseline	Metal Uncorrected	SmartMAR corrected	Our Technique at 25° corrected
<b>PBT</b>	693 (2)	681 (31)	683 (8)	695 (1)
<b>Cork</b>	-758 (10)	-657 (27)	-496 (15)	-756 (12)
<b>Blue Water</b>	87 (0)	-70 (28)	45 (2)	91 (1)
<b>Techtron HPV</b>	218 (1)	306 (57)	167 (21)	216 (1)
<b>Solid Water</b>	29 (1)	-113 (19)	-34 (4)	29 (2)
<b>Phantom</b>	-36 (2)	19 (9)	-5 (8)	-40 (1)

*Table 3: Mean HU numbers and standard deviations in parenthesis of plugs and phantom for all relevant scans.*

Structure	HU Number Difference with Baseline (HU)		
	Metal Uncorrected	SmartMAR	Our technique at 25°
<b>PBT</b>	-13	21	-1
<b>Cork</b>	-109	280	-2
<b>Blue Water</b>	171	40	-4
<b>Techtron HPV</b>	-89	50	2
<b>Solid Water</b>	153	55	0
<b>Phantom</b>	-66	35	5

***Table 4: HU number differences between the relevant scans for both metal artifact reduction techniques.***

### **3.4 Discussion**

The algorithm generated in this work was successful at eliminating metal artifacts created by dental amalgam in the posterior region of the image. It is possible to see that as the CT gantry angle increases, the posterior region becomes clearer of metal-affected pixels, leading to better visualization of the structures in the phantom. As a consequence of the combination of two angled scans, the artifacts extend to regions that were previously unaffected, such the nose and chin. However, as previously mentioned, those areas do not normally contain disease or OARs.

Several metal artifact reduction methods have been proposed and are currently available to the community. These methods include the use of MVCT, dual-energy CT, magnetic resonance imaging, additional CT scans and the complete removal of the dental work. However, each has important limitations and hence lacks wide clinical acceptance. A common technique in radiation oncology is to manually override HU values, but this has major drawbacks in that anatomy is still obscured and is now assumed to be homogeneous. Current metal artifact reduction algorithms are promising but have the downside of replacing missing data with artificially interpolated generated data. That approach creates additional uncertainty in the HU information, and such uncertainty is undesirable in diagnosis and in therapeutic dose calculations, particularly in applications such as proton therapy.

The metal artifact reduction technique presented in this work uses two angled CT scans to eliminate the metal artifacts posterior to the dental implants and produce accurate and faithful HU number information. Unlike the existing algorithms, the one developed here uses the correct HU information to reconstruct the final image and does not rely on metal thresholded sinogram deletions and interpolation of data, which can cause more artifacts [20] and uncertainty in HU accuracy. The technique developed in this study also has the potential to be applied to other areas of the body that have metal inserts (eg, surgical clips, prostheses) and therefore has the potential for improvement in artifact management and imaging of anatomical structures other than just HN. Another advantage of this technique is that it is performed in the image space and hence can be used by any CT scanner vendor. Raw data is intellectual property proprietary to each vendor and thus, is very difficult to attain. The method developed here does not require the manipulation of raw data and therefore can provide images with minimal artifacts posterior to the oral cavity.

The size difference measurements for all the plugs showed no correlation with gantry angle, in all directions. Angled CT scans elongate the imaged object in the AP direction, but these distortions were managed using a geometrical correction applied in the first part of the algorithm. Following that correction, all distortion measurements were on the order of 0.1 mm, with similarly small SDs. Measuring the distances in the SI direction was more challenging owing to worse resolution in that direction, yielding a larger observed SD—nearly three times that seen in the AP and LR directions. Similar to the distortion findings, the HU number was not correlated with gantry angle and showed high consistency throughout the different reconstructed images compared with the baseline image set. These results indicated that our novel technique described here provided nearly artifact-free images

in the posterior region of the phantom that were geometrically and HU number accurate when compared to a metal-free baseline. In addition to being geometrically and HU number accurate, it also outperformed a current commercially available artifact reduction method. When compared to SmartMAR, our technique provided better HU accuracy in the posterior region of the phantom and corrected the streaking caused by the metal implants better, shown by the improved HU difference and SD measurements inside the plugs and phantom.

The technique developed here manages metal artifacts with the use of correct (not interpolated or manipulated) data but carries one potential drawback. The reconstruction of the artifact-free image require two scans instead of one, which may deliver additional dose to the patient. The cost of any extra dose ( $< 10$  cGy) would need to be weighed against improved image quality and associated benefit to diagnosis and/or radiotherapy treatment of patients. The comparison to SmartMAR shown in this manuscript is indicative of the potential benefit behind our approach. For radiotherapy patients in particular, this one-time extra dose is negligible ( $< 0.1\%$ ) compared with the total treatment and imaging dose already committed to HN cancer patients.

The presented methodology in this manuscript was the introduction of a stereoscopic solution to reduce metal artifacts present in patients' HN CT images through the use of CT gantry angles. Future work will expand the image quality and robustness study comparing this technique to all major vendors' current metal artifact reduction algorithms with the use of a HN anthropomorphic phantom. We will also further investigate the performance of the technique in the context of radiation therapy and treatment planning system dose calculations. A dosimetric analysis will be performed on the anthropomorphic phantom to show the advantages of the algorithm developed here over the other approaches currently in



use. Proton treatment planning dose calculations and proton beam differences will be of particular interest because of their large dependency on HU accuracy and robustness.

### **3.5 Conclusion**

A stereoscopic metal artifact management algorithm was developed using CT gantry angle tilts and evaluated in a geometrical HN phantom. The algorithm developed here offered the improvement of not requiring the replacement of deleted metal thresholded data with artificially interpolated data. In addition, it used accurate HU data obtained from two different scans and was divided into two parts: the first included the untilting and correction of the angled image set, and the second involved the removal of the metal artifacts in the posterior region. Unlike other existing algorithms, this algorithm is independent of the CT scanner provider and therefore can be used in any scanner that allows for gantry tilts. Also, our technique is applied in the image space, and therefore does not require the need to acquire and manipulate the proprietary raw data from vendors. The images showed the successful removal of the artifacts present in the posterior region on the phantom, allowing for much better visualization of the structures. The quantitative analysis of the algorithm performance showed that it presents artifact corrected images with no geometrical distortion and with HU number accuracy when compared to the baseline. In addition, our technique outperformed a commercially used algorithm, SmartMAR, in providing artifact-free images with better HU agreement with the metal-free baseline. Future work will be done to further expand the image quality analysis and robustness among all major vendors' solutions, and to evaluate treatment planning dosimetry, specifically applied to proton therapy since proton treatment quality and robustness are highly dependent on HU accuracy.



## ***Chapter 4 - Specific Aim 2***

### ***Image quality analysis of a novel CT metal artifact management technique against four major CT vendor techniques on an anthropomorphic head and neck phantom***

#### **4.1 Introduction**

Head and neck scans represent almost 30% of all computed tomography (CT) scans done each year [1]. A substantial amount of these head and neck scans exhibit metal artifacts, particularly as produced by patients' dental work. These artifacts obscure tissues in the oral cavity and oropharyngeal region decreasing the ability to differentiate and delineate disease [2-4], potentially leading to erroneous diagnoses. This problem is also relevant in radiation oncology where the CT scan is used for treatment planning; metal artifacts on CT images have been found to increase dose heterogeneity and reduce target coverage [3-5].

Several solutions for metal artifact reduction (MAR) have been proposed, but many are impractical, produce inaccurate CT images, and/or are not clinically available and therefore are not extensively adopted [5-10]. Major vendors also offer MAR algorithms for clinical use. While these algorithms contain proprietary information, they are known to be

sinogram-based and work through the identification, deletion, and replacement of corrupted raw data. For example, Philips Healthcare offers an orthopedic MAR (OMAR) function, which is an iterative projection modification solution that performs several steps, including thresholding metal regions from the sinogram, removing them, and interpolating the missing data, to reconstruct the final artifact-adjusted image [11]. Similar to the OMAR function, Siemens Healthcare's iterative MAR (iMAR) algorithm removes high-contrast structures from the sinograms before interpolating the missing data [12]. GE Medical Systems' SmartMAR algorithm segments the metal data in the projection space and replaces those data with inpainted data [13]. Toshiba Medical's single-energy MAR (SEMAR) algorithm is also based on raw data segmentation and interpolation but incorporates different proprietary gradient correction features [14].

The effectiveness of existing MAR algorithms has been found to be partial. While these algorithms reduce the presence and severity of artifacts, this reduction is far from complete. Particularly for the difficult situation of the head and neck, typical algorithms were found to only reduce the severity and number by 15-30% [15]. Moreover, algorithms that manipulate the sinogram data estimate values to replace missing or suspected corrupted data instead of using true measured data. This process of estimating data can introduce inaccurate substitutions [9], possibly causing additional artifacts [16]. Hence, there is a clear need to improve metal artifact management, particularly in highly heterogeneous anatomical sites, such as the head and neck.

The purpose of this work was to perform a quantitative image quality analysis of our in-house-developed Artifact Management for Proton Planning (AMPP) algorithm for managing metal artifacts on head and neck CT scans by comparing the algorithm to major

vendors' commercially available approaches. The technical details of the AMPP algorithm are presented in a separate paper, but the algorithm reconstructs the image using a pair of tilted scans. The reconstruction occurs in the image space and so are the post-processing steps, which can be applied on any scanner and do not require data interpolation or estimation only making use of unedited scan data. In this study we evaluated the quantity of image improvement and found that the AMPP algorithm outperformed all of the vendors' commercially available approaches in the elimination of artifacts in the oropharyngeal region.

## **4.2 Materials and Methods**

### **4.2.1 Anthropomorphic head and neck phantom**

We designed an anthropomorphic head and neck phantom composed of tissue-equivalent materials [17], with a human skull and air cavities mimicking the tissue heterogeneities in patients. This phantom was based on an Alderson phantom (The Phantom Laboratory, Salem, NY) (

Figure 13a) modified to have a jaw insert and a cylindrical insert accessible from the bottom of the neck (

Figure 13b). The cylindrical insert, which was made of Solid Water (CNMC, Nashville, TN), enabled us to introduce soft-tissue features into the phantom, including a horseshoe-shaped “tumor” in the middle of the insert, 2 parotids lateral to the tumor, and spinal cord. These features were made of Blue Water (Gammex, Middleton, WI). The cylinder design was based on human anatomy representative of generalized oropharyngeal disease that is widely used for head and neck radiotherapy credentialing [18, 19].

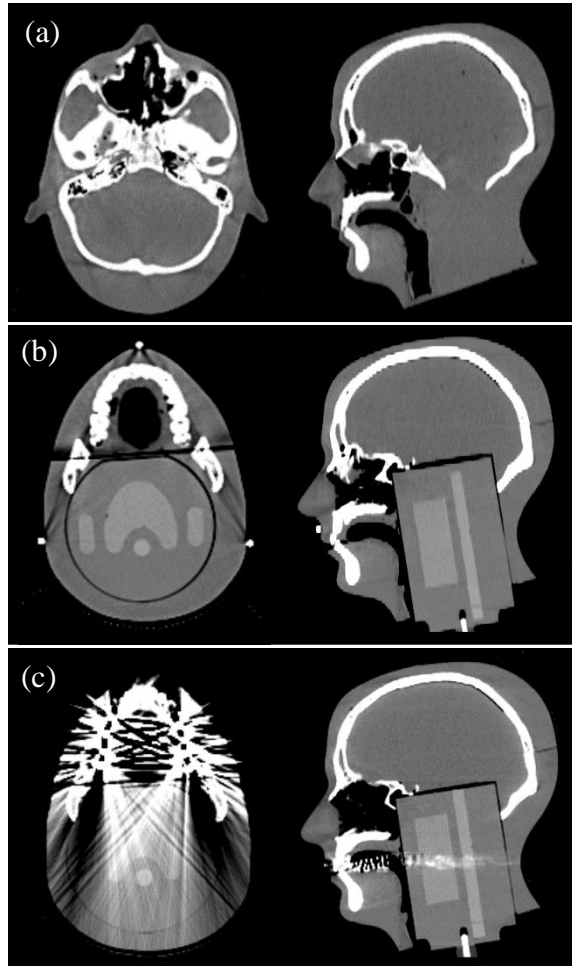


**Figure 13: (a) Axial and sagittal CT views of the Alderson phantom prior to modifications. (b) Axial and sagittal CT views of the modified phantom, which included a cylindrical insert containing a central target and 3 healthy structures, and a jaw insert. Holes were drilled in the molars in the jaw insert; these were filled with bone-equivalent materials in this panel. (c) Axial and sagittal CT views of the modified phantom with metal amalgam capsules in the tooth holes. The metal artifacts generated by the capsules are evident.**

The jaw insert enabled us to obtain images with and without metal artifacts. The lower jaw was cut to expose the top and bottom teeth. Holes were drilled in each of the 8 molars (4 superior and 4 inferior) to hold capsules made of either bone-equivalent material to simulate a case with no fillings (Techton HPV Bearing Grade; Gammex) or metal amalgams (Dispersalloy; Milford, DE) to simulate fillings and introduce metal artifacts. The locations, dimensions, and materials of the capsules were selected by a dental oncologist to be clinically realistic. The phantom with the metal amalgam capsules in place and the artifacts generated by them are shown in

Figure 13c.

#### **4.2.2 Scans**

The anthropomorphic phantom was scanned using Brilliance Big Bore (Philips Healthcare System), SOMATOM Definition Edge (Siemens Healthcare), Revolution HD (GE Medical Systems), and Aquilion PRIME (Toshiba Medical) CT scanners. Each scanner was



used to acquire an image set with the bone-equivalent capsules (baseline scan) and an image set with the metal amalgam capsules (metal scan). Each metal scan was reconstructed using the respective vendor’s MAR algorithm (corrected scan). The in-house AMPP algorithm was applied to image sets acquired with the Siemens SOMATOM Definition Edge scanner only, due to its performance being independent of CT scanner vendor (demonstrated in the robustness study of this manuscript). The parameters of each head and neck CT protocol used for the baseline and the metal scans are shown in Appendix B.

### 4.2.3 Data Analysis

The MARs algorithms were evaluated using severity of artifacts criteria over a centrally located CT slice and HU number accuracy over the introduced structures in the phantom.

***Planar Artifact Severity.*** We quantified artifact severity that remained after application of different MARs algorithms by comparing the HU maps of the MAR-corrected images with those of the corresponding baseline images for a central axial slice; for example, we compared OMAR-corrected scans with baseline scans obtained using the Philips scanner. To ensure that the same central slice of the phantom was compared across all platforms, the slices were selected with respect to fiducials positioned on the phantom. To ensure proper registration between the each baseline slice and its corresponding MAR corrected slice, we used rigid, intensity-based image registration in MATLAB. After image registration, we created HU error maps by subtracting each MAR-corrected image from its corresponding baseline image.

We calculated the percentage of bad pixels inside the circle that defined the phantom cylinder, which was considered the region of interest in the phantom that the algorithm aimed

to improve. All pixels with a HU error above +20 HU or below -20 HU were considered to be bad pixels. The 20-HU threshold was based on the HU standard deviation obtained in the baseline scan. The average standard deviation calculated inside the baseline structure volumes was 8 HU; therefore, HU differences more than 2 standard deviations from the mean were considered to be too far from the baseline value and thus represented demonstrably erroneous pixels.

**Structure HU number accuracy.** The target and OARs on the baseline image were contoured using the Eclipse treatment planning system (version 13.6; Varian Medical Systems, Inc., Palo Alto, CA). Contours were extended superiorly-inferiorly through the artifact-affected slices (~1.5 cm). Thus, the HU number accuracy was quantified for the volumes of interest affected by artifacts (i.e., those posterior to the metal in the oral cavity). The volumes created on the baseline scans were copied onto the corrected metal scans to maintain consistency throughout the volumes analyzed. The mean HU numbers and standard deviations were measured inside each structure, and mean HU differences were calculated using each metal scan HU ( $\overline{HU}_{MAR\ technique}$ ) and corresponding baseline scan HU ( $\overline{HU}_{baseline}$ ) according to the following equation:

$$\overline{\Delta HU} = \overline{HU}_{MAR\ technique} - \overline{HU}_{baseline}$$

#### 4.2.4 Robustness evaluation

We evaluated the robustness of the AMPP algorithm by applying the algorithm to images acquired using several different scanning parameters. The imaging parameters are

shown in Appendix B. For example, to determine the extent to which CT x-ray tube energy affected the performance of the algorithm, we applied AMPP to images acquired at 100, 120, and 140 kVp. The AMPP-corrected scan was repeated at 120 kVp on a GE scanner to investigate the algorithm's independence of scanner type. The AMPP algorithm was also evaluated in the context of different slice thicknesses, filter types, head tilt statuses, and scanner-specific reconstruction algorithms. To obtain each baseline scan, we repeated each metal scan without the metal amalgam in place so that each AMPP-corrected scan was compared with a corresponding baseline scan obtained using the exact same imaging parameters. In each scenario, artifact severity was evaluated by assessing the percentage of bad pixels and HU number accuracy within the structures' volumes.

## **4.3 Results**

### **4.3.1 Planar Artifact Severity**

The effectiveness of the existing MAR algorithms is shown qualitatively in Figure 14a-d; the AMPP-corrected image is shown in Figure 14e. The same axial slice was chosen from each data set for the analysis. Each MAR algorithm diminished the severity of the artifacts in the uncorrected images (

Figure 13c) but with varying, and sometimes limited, success. In some instances, the MAR algorithms introduced additional artifacts in the posterior region characterized by a subtle ripple effect on the streaks Figure 14c). In contrast, the AMPP algorithm eliminated artifacts posterior to the oral cavity; the AMPP-corrected image was nearly identical to the corresponding baseline image (

Figure 13b). Immediately near the metal, none of the algorithms evaluated were able to reduce the artifacts due to the proximity to the metal implants. Hence only the posterior region of the phantom was evaluated in the analysis. This compromise was considered to be acceptable because that is mostly the area of interest in oropharyngeal disease.

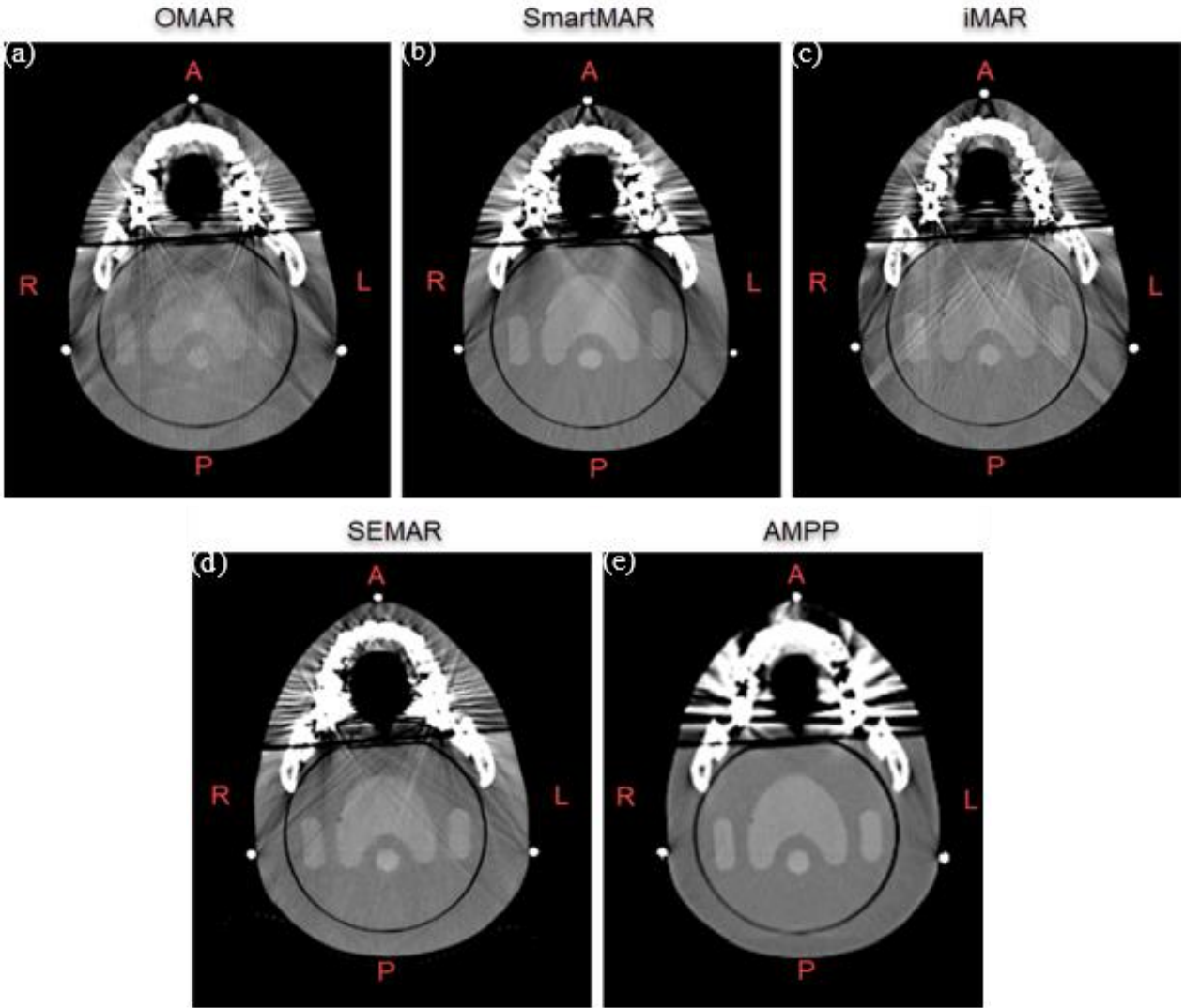


**Figure 14: (a-e) Axial and sagittal CT views of the anthropomorphic phantom, corrected using the commercial MAR algorithms (a-d) or the in-house-developed AMPP algorithm (e). The same axial slice was chosen from each data set for the analysis.**

The HU error maps show the quantitative differences between the corrected images and the corresponding baseline images in Figure 15. There were severe differences, displayed by

the dark red and dark blue colors, between the uncorrected image and corresponding baseline images. Compared with the uncorrected image, the MAR-corrected images were improved, but they still showed remarkable inconsistencies with the corresponding baseline images. In contrast, the AMPP-corrected image showed great agreement (within  $\pm 20$  HU) with the baseline image, displaying a mostly green difference map inside and outside the phantom. The percentages of bad pixels in the circular region of interest that defined the cylinder in the phantom were 78.1%, 65.5%, 29.1%, 25.5%, 27.9% and 4.2% for the uncorrected, OMAR, SEMAR, iMAR, SmartMAR and AMPP techniques respectively.

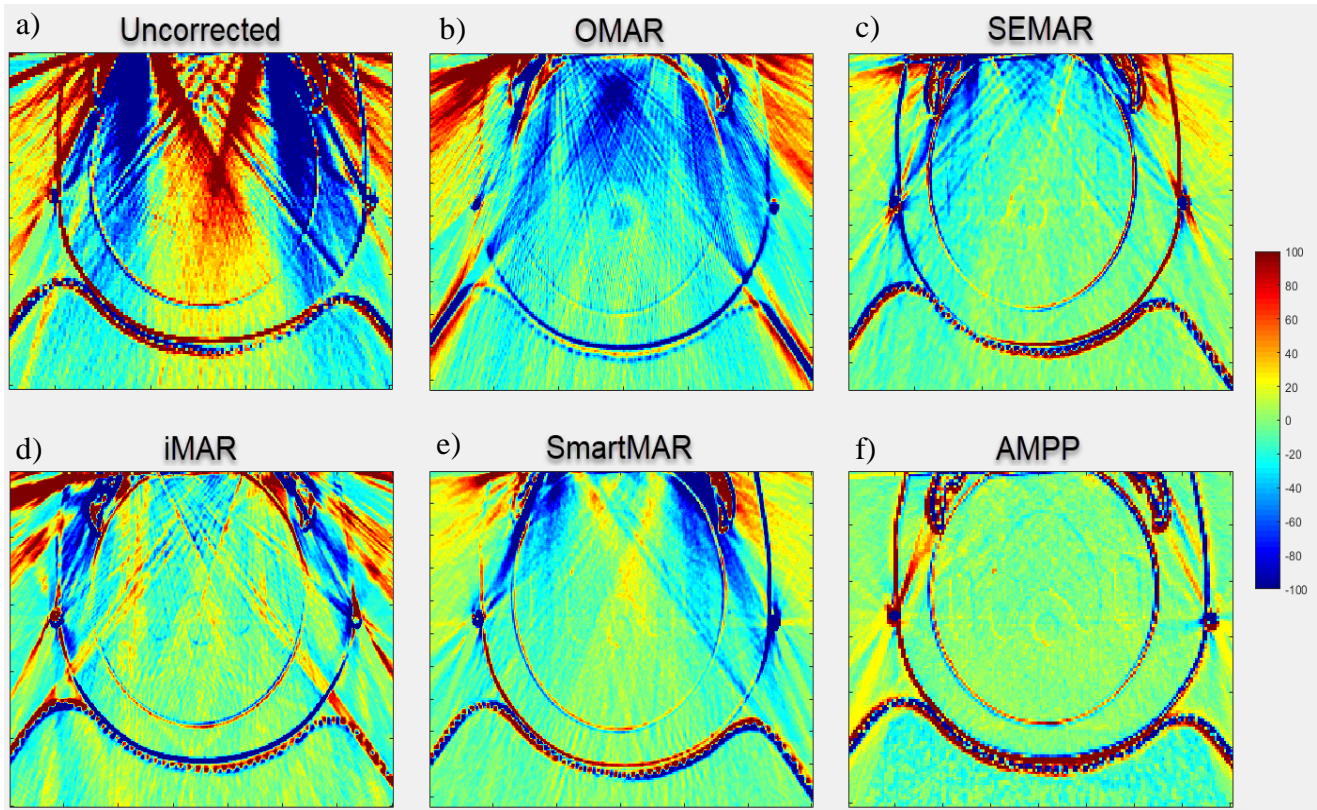


**Figure 15: HU error maps show differences between corrected images and corresponding baseline images. Severe HU differences are displayed by the dark red and dark blue colors.**

### 4.3.2 Structure HU number accuracy

For a volumetric analysis of the affected slices, the mean HU errors in the structure volumes in the phantom for the uncorrected and corrected images are shown in Table 5: Mean HU errors within each structure volume inside the phantom by correction technique.. The columns show the mean HU differences for each metal scan corrected by a MAR algorithm and its respective baseline. A difference close to 0 means that the algorithm improved the HU numbers within all volumes compared to the uncorrected scan. A negative number means the baseline HU value in that structure was larger than on the metal corrected scan. The commercial MAR algorithms provided different degrees of improvement depending on structures; notably, there were structures that had systematic average HU errors in excess of 20 HU, and all vendor algorithms had structures with average systematic errors of at least 15 HU. The AMPP algorithm consistently outperformed the commercial algorithms, regardless of location or anatomy, and improved the HU accuracy to nearly the same as that of the uncorrected baseline scan; the maximum systematic HU error was only 2 HU. The standard deviations in each structure volume for the baseline, uncorrected, and corrected images are shown in Table 6: HU standard deviation (SD) of each structure volume inside the phantom by correction technique.. As expected, the uncorrected image had the largest standard deviation owing to the many high- and low-density streaks within the phantom. The MAR algorithms showed some improvement but did not perform as well as the AMPP algorithm, which yielded standard deviations similar to the baseline values.

Structure	Mean HU error within Structure Volume (HU)					
	Uncorrected	OMAR	SmartMAR	iMAR	SEMAR	AMPP
<b>PTV</b>	39	-18	2	-15	-3	-2
<b>Spinal Cord</b>	36	-13	3	-13	-1	-1
<b>Right Parotid</b>	-67	-34	-15	3	-20	2
<b>Left Parotid</b>	-63	-36	-24	-4	-19	1

**Table 5: Mean HU errors within each structure volume inside the phantom by correction technique.**

Structure	HU SD within Structure Volume (HU)						
	Baseline	Uncorrected	OMAR	SmartMAR	iMAR	SEMAR	AMPP
<b>PTV</b>	8	41	25	13	27	13	6
<b>Spinal Cord</b>	9	21	19	10	21	13	9
<b>Right Parotid</b>	11	49	19	9	16	17	7
<b>Left Parotid</b>	6	43	23	13	15	13	6

**Table 6: HU standard deviation (SD) of each structure volume inside the phantom by correction technique.**

### 4.3.3 AMPP robustness evaluation

The percentages of bad pixels and mean HU errors for the different imaging parameters under which the AMPP-corrected images were acquired are shown in Table 7: Mean HU



errors within structure volumes and percentages of bad pixels for different imaging parameters under which the AMPP-corrected images were acquired. The AMPP algorithm performed similarly regardless of imaging parameter; each AMPP-corrected image showed similarly small HU differences and a small percentage of bad pixels as compared with the corresponding baseline images.

Structure	Mean HU error (HU)							
	Energy, 100	Energy,	Energy,	Energy, 140	Slice	SFOV	Head	Recon
	kVp	120 kVp	120 kVp	kVp				
	(Siemens)	(GE)	(Siemens)	(Siemens)				
<b>PTV</b>	-1	-1	-2	-1	0	0	-2	0
<b>Spinal Cord</b>	0	-2	-1	0	0	0	-2	2
<b>Right Parotid</b>	2	-3	2	1	4	-1	-3	2
<b>Left Parotid</b>	2	6	1	-1	3	6	-2	2
<b>% Bad Pixels</b>	1.5	1.4	4.2	0.8	3.8	2.5	2	2.6

**Table 7: Mean HU errors within structure volumes and percentages of bad pixels for different imaging parameters under which the AMPP-corrected images were acquired**

## 4.4 Discussion

On the basis of HU number information, all MAR algorithms reduced the percentage of bad pixels, at varying degrees of efficacy. Although the OMAR-corrected images retained

several artifacts and thus still had a large percentage of bad pixels, the SEMAR, iMAR, and SmartMAR algorithms reduced the percentage of bad pixels by factors of 2-3. In contrast, the AMPP algorithm reduced the percentage by a factor of 20. In terms of the entire volume of the affected slices, the current commercial MAR algorithms showed inconsistent performance; whereas the SmartMAR and SEMAR algorithms performed well where the target and spinal cord were defined, the iMAR algorithm performed well where the parotids were defined. In contrast, the AMPP algorithm performed consistently well throughout the entire posterior region of the phantom, regardless of the location and intensity of the metal artifacts. This was true both in terms of eliminating systematic HU errors as well as minimizing any spread in the HU over the structure. Our findings also show that the AMPP algorithm performed well under different CT image acquisition parameters. The percent of bad pixels achieved with the AMPP algorithm under different parameters were all similar to each other and smaller than those achieved with the commercial MAR algorithms, ranging from 0.8% to 4.2%, whereas those in the MAR-corrected images ranged from 25.5% to 65.5%. That the AMPP algorithm is robust, as well as independent of scanner type and imaging parameters, is important for its clinical application. These results suggest that the AMPP algorithm, whose performance exceeded that of all currently available commercial algorithms in the current study, can be applied to any scanner that allows for gantry tilts.

The results of this study hinge on the accurate registration of the image sets as described in the methods section. Good registration was evaluated visually, but in addition, we also investigated the sensitivity of the results to the image registration process. To investigate the impact of an incorrect registration, we shifted the AMPP-corrected image 1 and 2 pixels compared with the baseline image and reassessed the percentage of bad pixels in

the corrected image. Whereas the bad pixel percentage of the original AMPP-corrected image was 4.2%, that of the AMPP-corrected image with a misalignment of 1 pixel was 5.9%, and that of the AMPP-corrected image with a misalignment of 2 pixels was 11.8%. The figure showing the error maps for the incorrect registrations is shown in Appendix B. It is possible to see the outline of the target and OARs as the pixel offset increases. However, the percentage of bad pixels on the obviously poorly registered AMPP-corrected images were still much lower than those on the MAR-corrected images, suggesting that the registration process was robust.

In this study, a novel MAR algorithm was evaluated and compared to 4 currently available major commercial algorithms; OMAR (Philips Healthcare System), SmartMAR (GE Medical Systems), iMAR (Siemens Healthcare) and SEMAR (Toshiba Medical). An anthropomorphic head and neck phantom was designed and used to perform the analysis by providing a method for obtaining metal free scans (baseline) and artifact filled scans (with metal amalgam). Although commercial MAR algorithms generally reduced the severity of metal artifacts in head and neck CT scans, the algorithms performed slightly differently from each other, consistent with their individual proprietary distinctions. Unanimously, their performance was inferior to that of our in-house-developed AMPP algorithm. The AMPP algorithm has the potential to be broadly implemented, improve visualizations in patient anatomy and provide accurate, not interpolated HU information. This can help with diagnosis as well as treatment planning in radiation oncology. In future studies, we will evaluate the proton therapy dosimetric performance of the MAR algorithms investigated in the present study.

## ***Chapter 5 - Specific Aim 3***

### ***The dosimetric implications of commercial CT metal artifact reduction algorithms and a novel in-house algorithm for proton therapy of head and neck cancer***

#### **5.1 Introduction**

Dental amalgam implants present a common challenge in the Head and Neck (HN) cancer patient population. Metal fillings, common in many cancer patients, can create severe imaging artifacts when undergoing computed tomography (CT) imaging. These artifacts can seriously affect disease diagnosis as well as the subsequent radiation treatment planning [1-3]. These artifacts are characterized by dark and bright streaks throughout the CT image slices that were affected by the metal, resulting in incorrect HU number designations and blurring of anatomy. High atomic number metals strongly attenuate the CT signal, causing incorrect HU calculation and assignment during the image reconstruction process. This selective attenuation phenomenon is called beam hardening and is the fundamental cause of CT metal artifacts[4]. Image reconstruction algorithms will attempt to correct for this polyenergetic nature of the x-ray spectrum but are not optimized for highly attenuating materials such as metal. In addition to beam hardening effects, high density materials will create increased

scatter and photon starvation in the detectors that add to the deterioration of the resulting CT images. Techniques to reduce noise by increasing the tube potential and mAs, or the use of adaptive filtering have been shown to be helpful but only partially alleviate the image quality issues [5].

One current available strategy to address metal artifacts in CT images is through the use of commercial artifact reduction algorithms. In general, metal artifact reduction (MAR) algorithms work through the detection and removal of corrupted data, followed by the interpolation of the data and reconstruction of the final CT images. Each vendor offers a unique algorithm; these differ in their approach at estimating the missing data. Linear interpolation, sinogram normalization, tissue class modeling and other methods used are some examples of such MAR techniques [6-8]. The various commercial MAR techniques can result in substantial differences between the final reconstructed images [9]. Addressing artifacts through MAR algorithms may seem like an attractive solution due the elimination of the subjectivity and time-consuming aspects of the typical manual Hounsfield unit (HU) overriding techniques used in the clinic. However, sinogram manipulation in CT images that contain metal artifacts needs to be considered carefully as its success is highly dependent on the accurate estimation of the new interpolated values. Sharp transitions between original projections and estimated projections can create additional unwanted artifacts [10], and data loss near the metals can cause blurring in the image [11]. Moreover, these algorithms have been found to be substantially ineffective at resolving the artifacts.

In addition to the potential for data loss and introduced artifacts, the success of these algorithms at actually reducing artifact severity must also be considered. Studies evaluating the performance of CT MAR algorithms have been published in the literature. However, most

of the studies were only performed in simplistic environments such as homogenous geometrical phantoms with qualitative endpoints [12-14]. Huang et al. investigated three current commercially available MAR algorithms on a heterogeneous anthropomorphic phantom and concluded that they were not successful at reducing artifacts specifically caused by dental fillings and introduced new artifacts in adjacent image planes [15]. In addition to a lack of quantitative image quality studies and a poor algorithm performance in highly heterogeneous sites, the success of commercial MAR algorithms on dose calculation [16, 17] has been substantially limited to photon therapy; the impact on proton radiation therapy is unknown. A key component to accurate proton therapy treatment planning is knowing the exact range of the protons as they travel through the patient. Any uncertainty in the proton range will result in an uncertainty in the location of the dose deposition from protons. Proton beam ranges are a topic of focus in the proton therapy community due their high sensitivity to uncertainty, one source of which is incorrect HU assignment in CT images [18]. The precise location of the distal dose gradient in patients needs to be predicted accurately in order to fully utilize the potential advantage of proton's sharp falloff at the distal end of the proton dose distribution. The accuracy in proton dose calculations is directly related to the conversion schemes implemented to relate HU information to relative stopping power. Hence, the purpose of this study is to investigate the dosimetric impact of all major vendor's MAR algorithms as they compare to each other. In addition, we also include and compare a novel in-house technique (AMPP) [19], which is a stereoscopic technique developed using CT gantry tilts and is different from the commercial options as it is not based on sinogram manipulation or direct interpolation methods. The dosimetric impact of these algorithms were evaluated using an anthropomorphic HN phantom.

## **5.2 Methodology**

### **5.2.1 Anthropomorphic Phantom**

A realistic anthropomorphic HN phantom composed of tissue-equivalent materials [20] with a human skull and air cavities mimicking tissue heterogeneities in patients was used in this study. The phantom was an Alderson phantom (The Phantom Laboratory, Salem, NY) that was modified to allow for both artifact-filled and baseline (no artifacts) CT scans. The lower jaw was cut to expose the top and bottom teeth and holes were drilled in each of the 8 molars (4 superior and 4 inferior). Capsules made of material that is bone-equivalent in proton beams [21] were made that could be inserted into the molars were used to simulate patients with no fillings (Techton HPV Bearing Grade; Gammex) and capsules made with metal amalgams (Dispersalloy; Milford, DE) were used to simulate fillings and introduce metal artifacts. The locations, dimensions, and materials of the capsules were selected by a certified dentist to be clinically realistic.

In addition to the jaw modification, a cylindrical insert accessible from the bottom of the neck was designed to introduce soft-tissue features into the phantom, including a Horseshoe-shaped target in the middle of the insert, and two lateral parotids and a spinal cord posterior to the target that served as organs at risk (OAR). The design describes a generalized oropharyngeal disease and shares dimensions with the IROC proton head and neck phantom used for clinical trial credentialing [22]. The cylindrical insert and the structures were made of Solid Water (CNMC, Nashville, TN) and Blue Water (Gammex, Middleton, WI), respectively. Figure 16(a) shows the axial and sagittal CT scans of the phantom displaying the structures described above in the cylindrical insert without the dental amalgams in place.

Figure 16(b) is the CT scan of the HN phantom when the bone equivalent teeth structures were replaced by the dental metal amalgams, creating streaking artifacts that can be visualized in the axial and sagittal views.

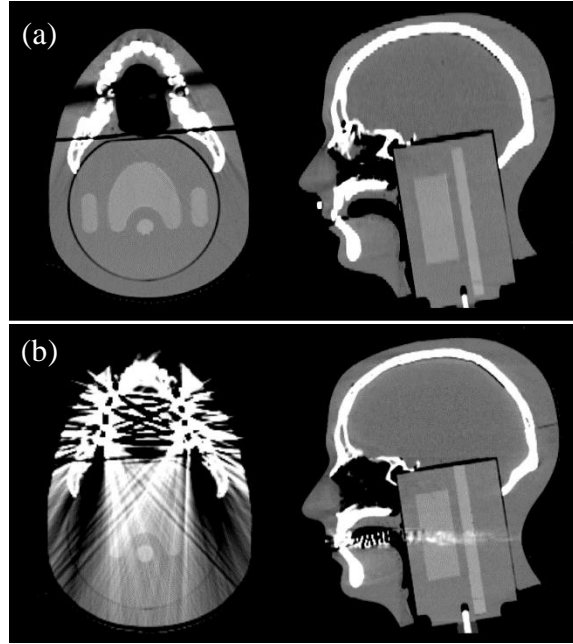


**Figure 16: (a) Axial and sagittal CT views of the modified Alderson phantom including the jaw insert and the cylindrical insert (containing a central target, parotids, spinal cord). (b) Axial and sagittal CT views of the modified phantom with metal amalgam capsules in the tooth holes showing the metal artifacts generated.**

### **5.2.2 CT image sets and MARs algorithms**

The anthropomorphic phantom was scanned using the Brilliance Big Bore (Philips Healthcare System, Bothell, WA), SOMATOM Definition Edge (Siemens Healthcare, Forchheim, Germany), Revolution HD (GE Medical Systems, Waukesha, WI), and Aquilion PRIME (Canon Medical Systems USA, Tustin, CA) CT scanners. In order to maintain positional consistency throughout all scans, the phantom was aligned in the supine position using a Klarity™ mold and fiducials. Each scanner was used to acquire an image set with



the metal amalgam capsules in place in order to generate the artifacts. Each metal scan was reconstructed using the respective vendor's MAR algorithm: OMAR from Philips, iMAR from Siemens, SEMAR from Canon, SmartMAR from GE, and AMPP as our in-house algorithm. The AMPP algorithm was applied to an image set acquired with the Siemens scanner without the vendor's MAR algorithm in place. In addition to the corrected image sets, an uncorrected image (based on the Siemens scan) was also acquired. A baseline scan was also obtained in which the bone equivalent capsules were used and hence, provided an artifact-free image. The imaging parameters (kVp, slice thickness, mA, scan field of view, head tilt and reconstruction type) of each scan are shown in Table 8. CT scan parameters were kept as similar as possible.

MAR TECHNIQUE	CT VENDOR	ENERGY (KVP)	SLICE THICKNESS (MM)	MA	FOV	PHANTOM HEAD TILT	RECON TYPE
<b>BASELINE</b>	Siemens	120	2	300	Head	No	Standard
<b>UNCORRECTED</b>	Siemens	120	2	300	Head	No	Standard
<b>OMAR</b>	Philips	120	3	300	Head	No	Standard
<b>SEMAR</b>	Toshiba	120	3	280	Head	No	Standard
<b>IMAR</b>	Siemens	120	2	300	Head	No	Standard
<b>SMARTMAR</b>	GE	120	2.5	300	Head	No	Standard
<b>AMPP</b>	Siemens	120	2	300	Head	No	Standard

**Table 8: Head and neck CT protocols used for the baseline and the metal scans.**

### 5.2.3 Treatment Planning

Proton spot scanning treatment plans were designed using Eclipse treatment planning system (version 13.6; Varian Medical Systems, Inc., Palo Alto, CA) on the baseline image set, following the treatment planning guidelines used by the MD Anderson Proton Therapy

Center of Houston, TX. Two anterior oblique beams and a posterior beam were used to deliver a prescription of 60 Gy to the Horseshoe shaped target shown in Figure 17 (a). Despite not being visibly present in the CT images, additional target shapes and sizes (Figure 17(b-e)) were contoured within the insert in order to further investigate the performance of the MAR algorithms at different anatomical locations. The additional four target contours, designated Bean, Sphere, Dot and X, were based on actual human disease locations and shapes treated at the MD Anderson Proton Therapy Center and are shown in Figure 17(f-j). The treatment planning parameters used for each target's plan were based on clinical arrangements and can be found in Table 9.

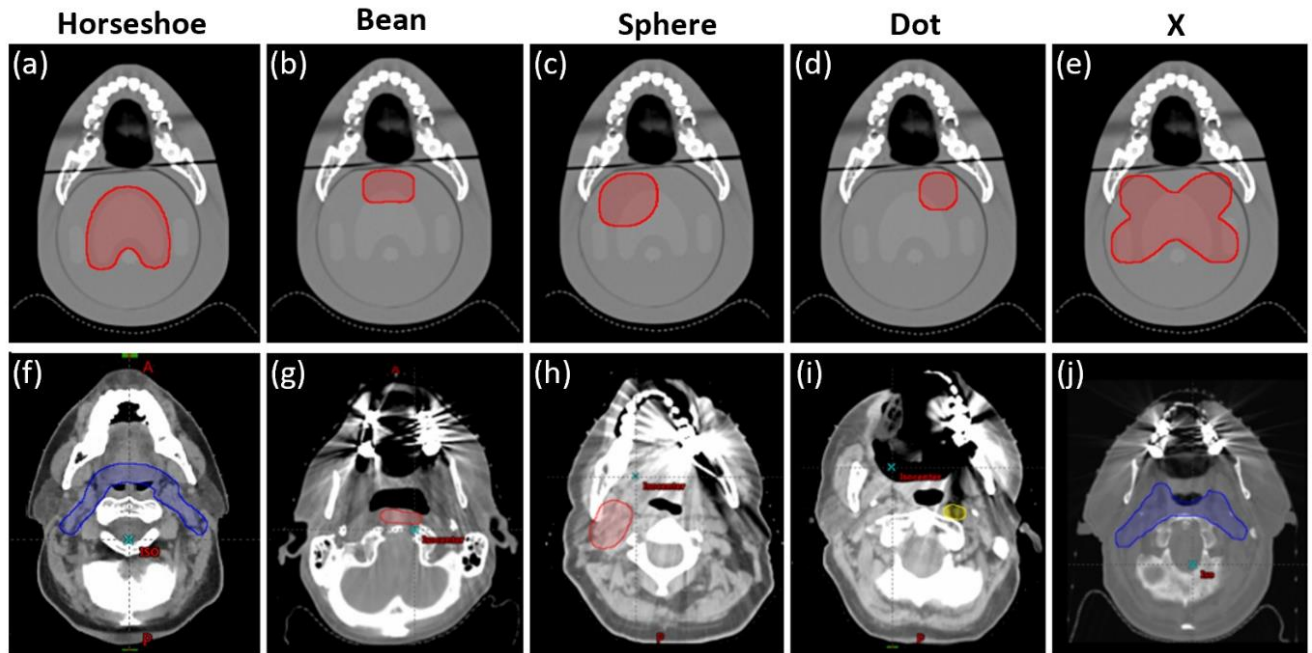


**Figure 17: Target contours created (a-e) on the anthropomorphic phantom designed based on real HN patient disease (f-j), respectively.**

TARGET	PLANNING PARAMETERS	FIELD 1	FIELD 2	FIELD 3
<b>HORSESHOE</b>	Angle	180	65	295
	Couch rotation	0	350	10
	Field Weight	1	1	1
	Collimator rotation	0	0	0
<b>BEAN</b>	Angle	180	80	175
	Couch rotation	0	0	0
	Field Weight	1	1	1
	Collimator rotation	0	0	0
<b>SPHERE</b>	Angle	180	255	275
	Couch rotation	0	0	0
	Field Weight	1	1	1
	Collimator rotation	0	0	0
<b>DOT</b>	Angle	180	80	275
	Couch rotation	0	0	0
	Field Weight	1	1	1
	Collimator rotation	0	0	0
<b>X</b>	Angle	180	80	280
	Couch rotation	0	0	0
	Field Weight	1	1	1
	Collimator rotation	0	0	0

**Table 9: Treatment planning parameters used for each target's proton plan designed on the baseline.**

Each targets' plan was designed on the baseline image set with a beam arrangement depicted in Table 2. Multi-field optimization was used in all plans to achieve the best target coverage. Once optimized, the proton beams were copied onto the different artifact corrected image sets without reoptimization of the beams' parameters. This step was taken to evaluate dose distribution differences once the beams were placed in the different MAR-corrected and uncorrected image sets. An additional step was taken to address the positioning of the phantom on the different CT scanner couches. The dose grid used was considered to be inside the body

contour of the phantom in order to avoid dose calculation errors originating from variations in the different CT table HU number. The body contour was copied onto all image sets so the same dose grid was used.

#### **5.2.4 Data Analysis**

The evaluation of the proton dose distributions' differences for the various targets and MAR algorithms was performed by comparing typical clinical dose volume histogram (DVH) metrics, including planning target volume (PTV D95) and clinical target volume (CTV D99) coverages, V100, D0.03cc, and heterogeneity indexes. Since these metrics are dependent on the volume of the structures being evaluated, each target was copied from the baseline onto the other image sets to maintain consistency between all volumes. The extent in the superior-inferior direction of all targets was 1.8 cm and it was chosen to include the slices that contained artifacts. In addition to using the DVH metrics, a qualitative assessment of the MAR-corrected dose distributions as compared to the baseline dose distribution was performed.

### **5.3 Results**

Clinically realistic plans were successfully designed and optimized for each of the PTVs on the baseline image set. The dose distributions originating from the baseline plans copied onto the MAR-corrected and uncorrected images showed substantial differences as compared to the baseline DVHs. This was observed for all 5 target shape/location combinations analyzed. The DVHs obtained for the Horseshoe, Bean, and Sphere targets are shown in

Figure 18 as representatives of the DVH data. In general, the target DVHs from the commercial MAR algorithms showed both underdosing and/or overdosing of the target depending on the algorithm used to correct the artifacts and the anatomical location of the target. For example, for the Bean target, most algorithms systematically overestimated the dose to the target by as much as 5-6%. For the Sphere target, most algorithms systematically underestimated the dose by 1-2%. But the patterns were varied. Also of note is the black line in this figure, which shows the result when no metal artifact reduction strategy is applied. This result is comparable, and often superior to, the commercial MAR solutions from the vendors, indicating that the vendor solutions were not particularly successful at mitigating the impact of the artifacts. However, the in-house algorithm AMPP showed the highly comparable DVHs to the baseline (no metal) proton plan (Figure 18), indicating AMPP was the best image set to perform the proton dose calculations for all targets.

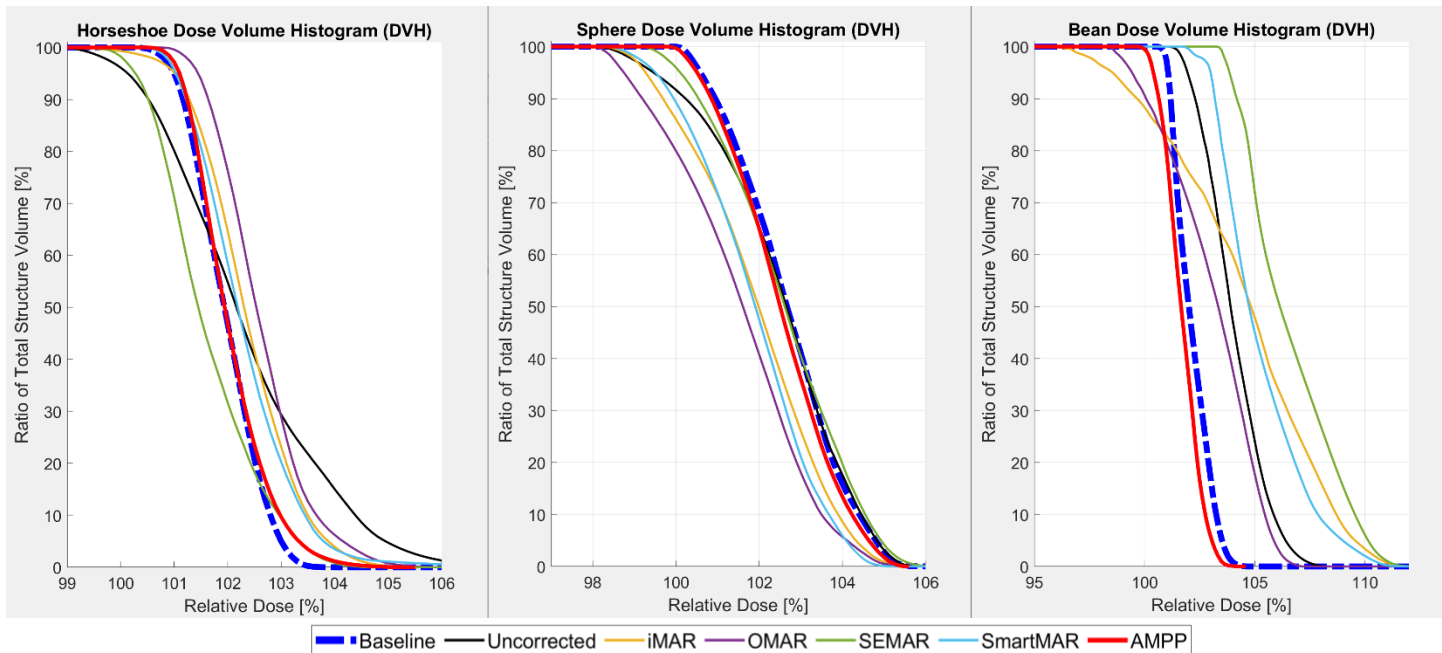


**Figure 18: Dose volume histograms for the (a) Horseshoe, (b) Sphere and (c) Bean CTVs comparing all the MAR-corrected and not corrected images.**

The baseline treatment plans generated on metal-free baseline images served as a reference for the MAR technique comparisons. All had PTV D95 and CTV D99 target coverages that were clinically acceptable per the review of an MD Anderson radiation oncologist, and CTV V100 and D0.03cc values within the clinical recommendations. In contrast, the DVH metrics extracted from the plans copied onto the artifact-corrected and uncorrected images varied greatly depending on the algorithm used to correct the artifacts and the location of the target. Table 10 shows a comprehensive view of the DVH metrics for each target shape and image set, with each value ordered from lowest to highest. Since the DVH metrics are a representation of the DVH curves, this data is consistent with that shown in Figure 18, and highlights that no commercial MAR algorithm consistently reproduced the same result as the baseline, and were also inconsistent in how those deviations manifested depending on the target shape/location. AMPP, however, showed consistently similar DVH metrics for all targets as compared to the baseline. This was true for all metrics evaluated.

	PTV D95 (%)		CTV D99 (%)		V100 (%)		D0.03cc (%)		Heterogeneity Index
<b>Horseshoe Target</b>									
NoMAR	100.2	NoMAR	99.4	NoMAR	96.0	Baseline	103.5	Baseline	1.027
SEMAR	100.3	SEMAR	99.8	iMAR	99.3	SEMAR	104.4	AMPP	1.032
Baseline	100.9	iMAR	100.2	OMAR	<u>100.0</u>	AMPP	104.8	OMAR	1.038
iMAR	101.0	Baseline	100.7	SEMAR	<u>100.0</u>	iMAR	105.2	SEMAR	1.040
SmartMAR	101.0	AMPP	100.8	SmartMAR	<u>100.0</u>	OMAR	<u>105.6</u>	iMAR	1.043
AMPP	101.1	OMAR	101.1	Baseline	100.0	SmartMAR	<u>107.2</u>	SmartMAR	1.045
OMAR	101.4	SmartMAR	101.7	AMPP	100.0	NoMAR	107.6	NoMAR	1.068
<b>Sphere Target</b>									
NoMAR	99.1	OMAR	98.3	OMAR	79.9	SmartMAR	104.8	Baseline	1.050
OMAR	99.1	NoMAR	98.6	iMAR	86.0	OMAR	105.2	AMPP	1.050
iMAR	99.4	iMAR	98.7	SmartMAR	88.8	iMAR	105.3	SmartMAR	1.059
SEMAR	99.9	SmartMAR	98.8	NoMAR	91.6	AMPP	105.3	SEMAR	1.060
SmartMAR	99.9	SEMAR	99.5	SEMAR	95.9	Baseline	105.4	iMAR	1.064
Baseline	100.4	AMPP	100.1	Baseline	99.7	NoMAR	105.5	OMAR	1.066
AMPP	100.4	Baseline	100.2	AMPP	99.7	SEMAR	105.7	NoMAR	1.068
<b>Bean Target</b>									
iMAR	98.5	iMAR	96.8	iMAR	88.3	AMPP	103.5	Baseline	1.031
OMAR	99.4	OMAR	98.6	OMAR	90.7	Baseline	104	AMPP	1.035
AMPP	100.4	AMPP	100.1	AMPP	99.5	OMAR	106.7	NoMAR	1.056
Baseline	101.0	Baseline	100.9	Baseline	100.0	NoMAR	<u>107.5</u>	SEMAR	1.072
NoMAR	102.0	NoMAR	101.5	NoMAR	<u>100.0</u>	SmartMAR	<u>110.5</u>	OMAR	1.079
SmartMAR	103.0	SmartMAR	102.1	SEMAR	<u>100.0</u>	iMAR	111	SmartMAR	1.082
SEMAR	103.9	SEMAR	103.5	SmartMAR	<u>100.0</u>	SEMAR	<u>111.1</u>	iMAR	1.146
<b>Dot Target</b>									
NoMAR	99.5	NoMAR	100.0	NoMAR	99	AMPP	103.5	Baseline	1.023
AMPP	100.4	AMPP	100.8	OMAR	<u>100</u>	Baseline	103.7	AMPP	1.027
Baseline	100.8	Baseline	101.4	SEMAR	<u>100</u>	NoMAR	107.5	SmartMAR	1.035
OMAR	102.0	OMAR	101.9	iMAR	<u>100</u>	OMAR	<u>108.5</u>	SEMAR	1.047
SEMAR	104.5	iMAR	104.3	SmartMAR	<u>100</u>	SEMAR	<u>109.5</u>	iMAR	1.062
iMAR	104.6	SEMAR	104.6	Baseline	100	SmartMAR	<u>109.5</u>	NoMAR	1.075
SmartMAR	106.0	SmartMAR	105.9	AMPP	100	iMAR	<u>110.8</u>	OMAR	1.076
<b>X Target</b>									
NoMAR	99.1	NoMAR	99.2	NoMAR	94.8	Baseline	105	Baseline	1.043
SEMAR	99.4	OMAR	99.4	OMAR	96.0	NoMAR	105.5	AMPP	1.045
OMAR	99.6	SEMAR	99.4	SEMAR	96.8	SmartMAR	105.5	SmartMAR	1.050
iMAR	100.0	SmartMAR	99.4	iMAR	97.4	iMAR	105.7	iMAR	1.054
SmartMAR	100.0	iMAR	99.6	SmartMAR	97.5	AMPP	105.8	NoMAR	1.055
Baseline	100.3	Baseline	100.2	Baseline	99.7	OMAR	106	SEMAR	1.057
AMPP	100.5	AMPP	100.3	AMPP	99.8	SEMAR	106	OMAR	1.059

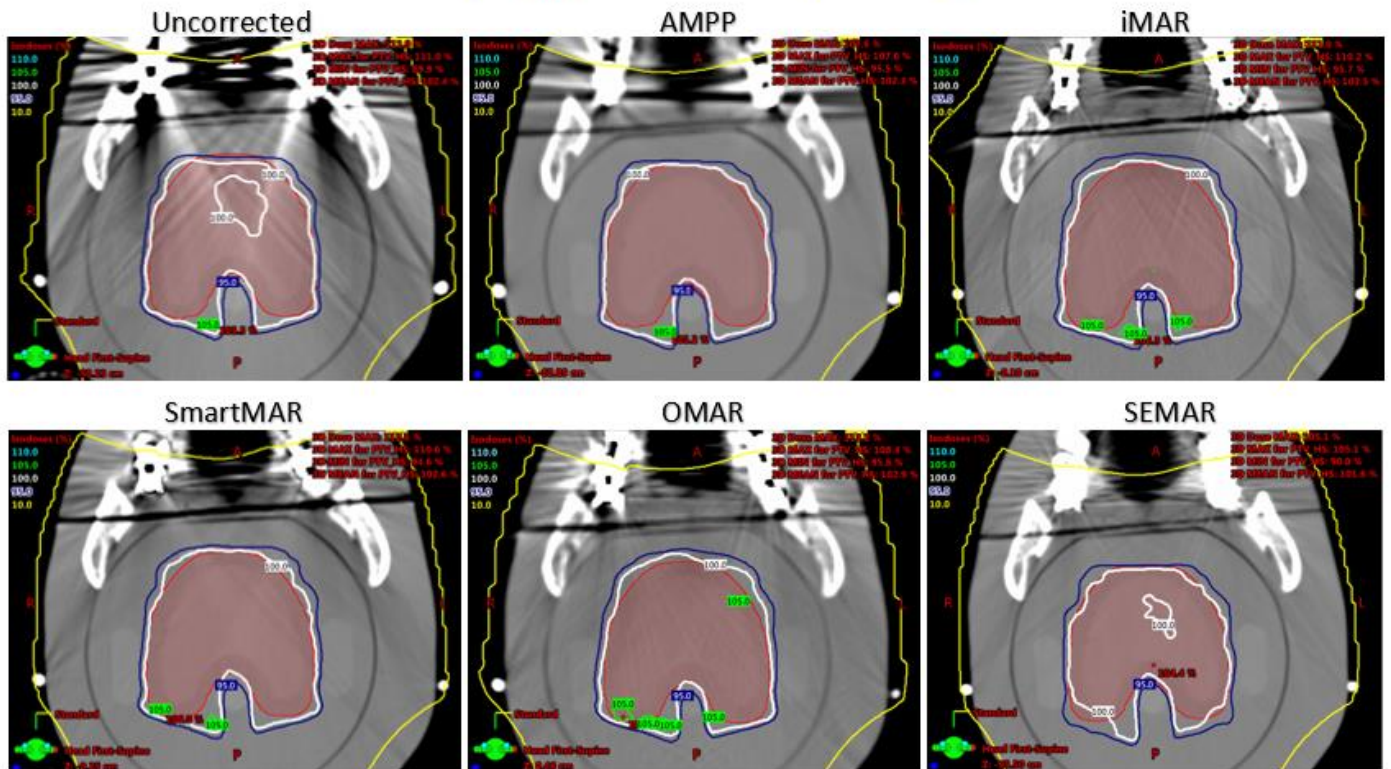
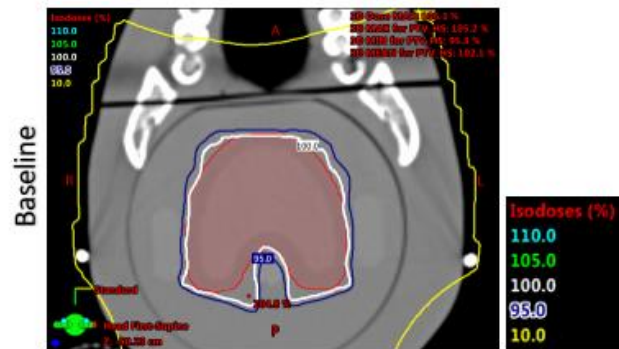
**Table 10: Planning evaluation metrics for all targets included in this study. The baseline and AMPP plans are highlighted for ease of comparison. Underlined numbers show a correlation between V100 and D0.03cc values, indicating an overdose (larger D0.03cc) as opposed to achieving quality target coverage (V100 = 100).**

The proton dose distributions for the Horseshoe, Sphere, and Bean targets can be seen in

Figure 19. The changes in the dose distribution observed throughout the different targets are shown on a representative CT slice directly affected by the streaking artifacts. The same axial slice was selected in each image set to allow for a direct comparison. For all targets, the dose distributions calculated on the MAR-corrected and uncorrected images showed substantial discrepancies when compared to the baseline. The Horseshoe shaped target showed the most stable dose distribution across all image sets, with only a few hot and cold spots and reasonable target coverage compared to the baseline. In contrast, the Sphere target showed an all-around underdosing for all commercial MAR solutions and the uncorrected image. Conversely, the Bean target showed a large increase in hotspots, sometimes having nearly the entire target covered by the 105% isodose line with SmartMAR and SEMAR. Alternatively, dose distributions copied onto AMPP-corrected images showed good agreement to the baseline across all targets analyzed.



(a)



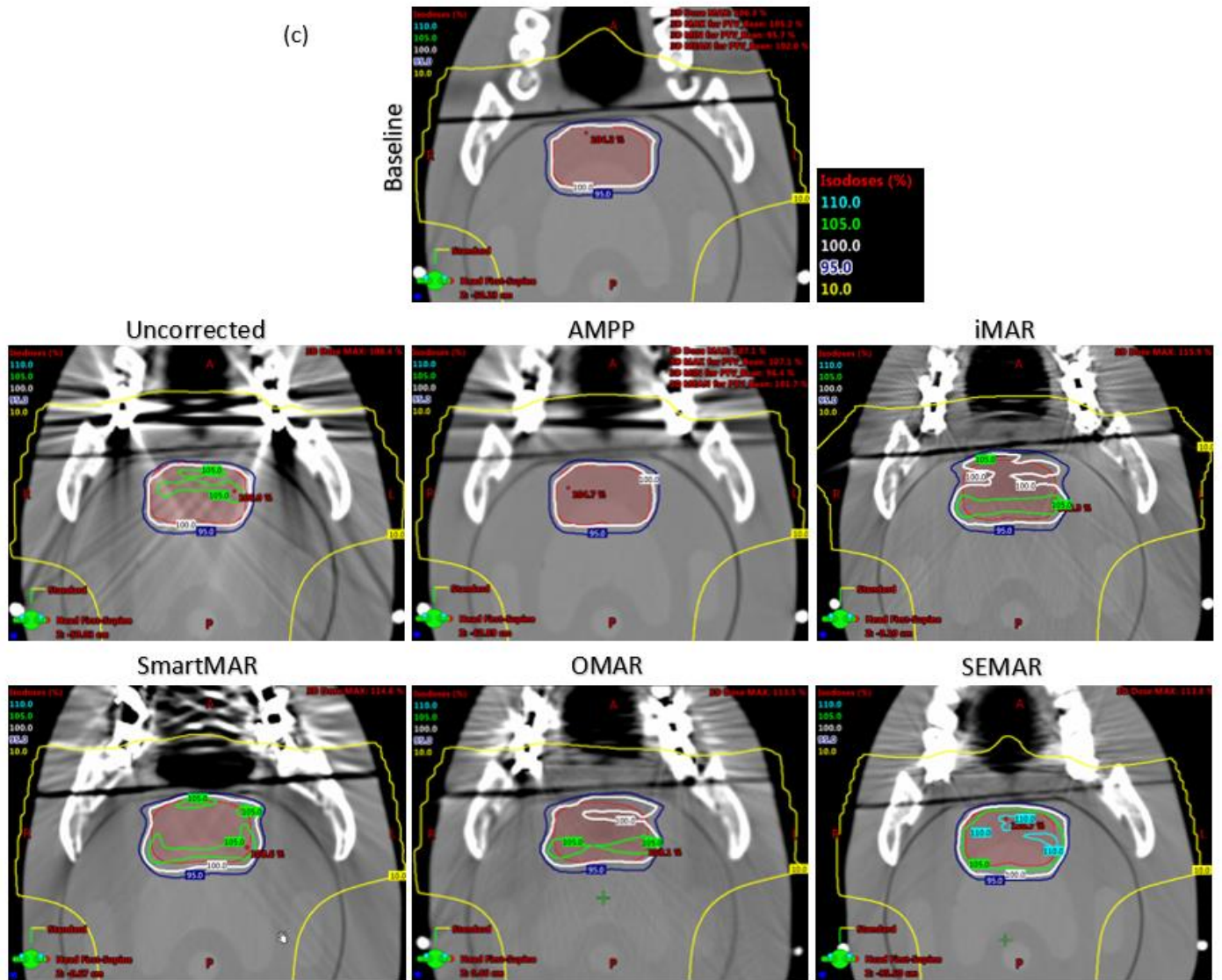
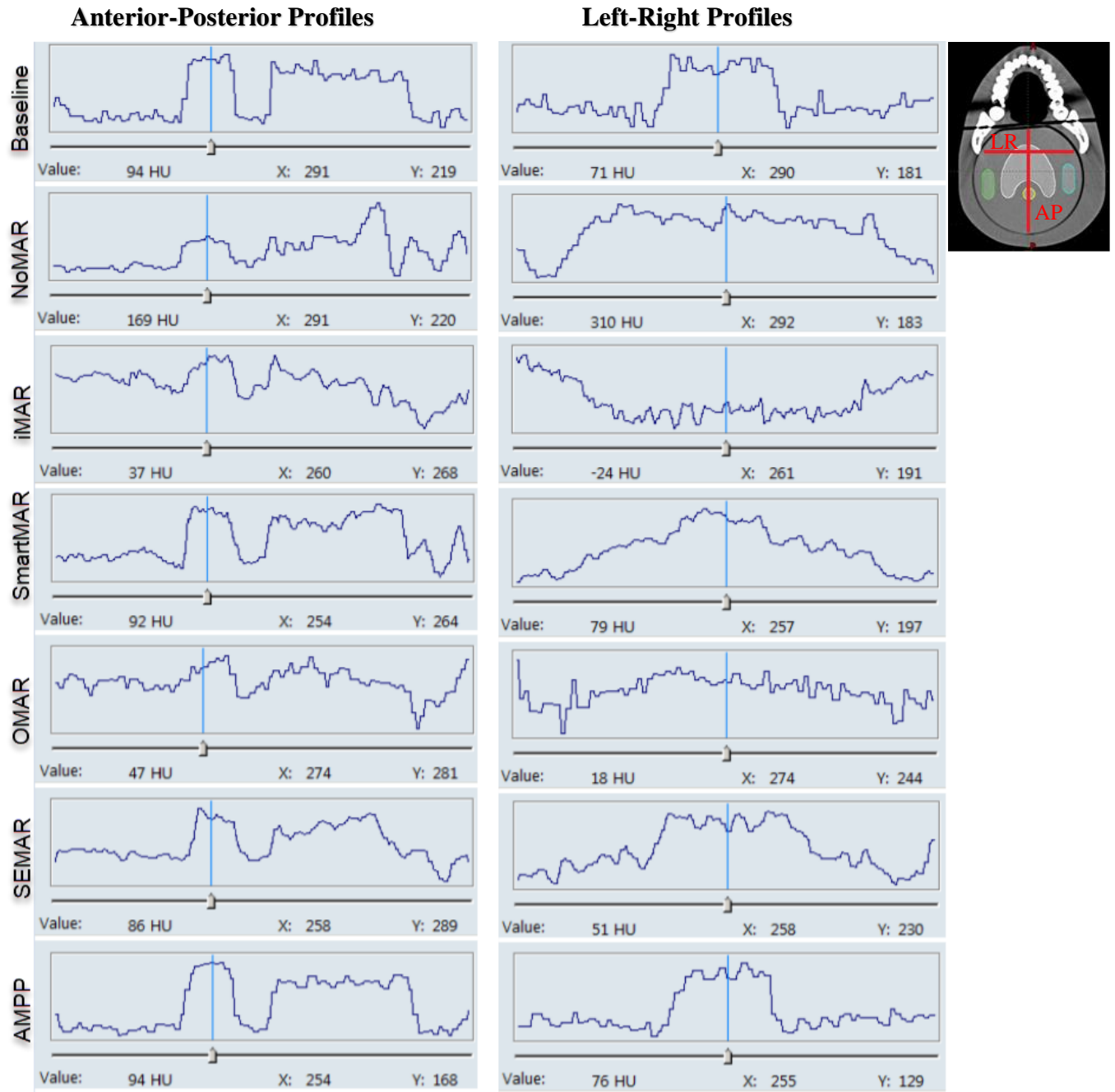


Figure 19: Axial view of the anthropomorphic phantom showing the proton dose distributions for the (a) Horseshoe, (b) Sphere and (c) Bean targets. Each PTV is shown in red for all the different MAR corrected and uncorrected image sets.

In order to further understand cases where inadequate or inaccurate HU corrections were obtained with the commercial MARs algorithms, which were sometimes worse than no correction at all, an HU profile assessment and an additional dosimetric investigation was performed. Anterior-posterior (AP) and left-right (LR) HU profiles were extracted using the planning system from all image sets and are shown in Figure 20. The blue vertical line serves as a reference point along the profiles and was kept consistent within the phantom, presenting the HU value inside the spinal cord on the AP profile and inside the Horseshoe target on the LR profile. It is possible to see the large impact in the HUs on the reference values when artifacts are left uncorrected or commercial algorithms have been applied as compared to baseline. There is a variation of 37 HU to 169 HU and -24 HU to 310 HU in comparison to the baseline reference values of 94 HU and 71 HU, for the AP and LR profiles, respectively. These represent stopping power percent differences that range from -4.4% to 2.7% and -7.1% to 10% as compared to the baseline for the AP and LR profiles, respectively, and explains the proton beam range and dosimetric consequences seen in the treatment planning results shown in Figure 18. In addition to the reference value varying substantially, the shape of the profile was drastically changed in some instances. The LR profile, for example, lost the baseline peak representing the Horseshoe target on the uncorrected, iMAR, SmartMAR, OMAR image sets. In contrast to profiles through the uncorrected images, or those corrected with commercial MARs, the AMPP algorithm showed nearly identical reference HU values and the most consistent profile shape compared to the baseline in both directions. This supports the dosimetry results that proton plans on AMPP corrected images were most comparable to the baseline.

In order to further investigate the algorithm performance, the treatment planning exercise was repeated for the Dot target at a location that was originally less affected by artifacts (3 cm posteriorly). This investigated if the differences seen were the result of the target size or target location. After moving the Dot PTV, the plans designed on the commercial algorithm image sets showed improved performance by matching the Baseline DVH better (Figure 21). This finding supports the interpretation that the commercial algorithms perform better where metal artifacts are minimal, implying their correction in severe artifact regions is insufficient.

## **HU Line Profiles**



**Figure 20: Anterior-posterior and left-right HU profiles extracted from each MAR corrected and uncorrected image set.**

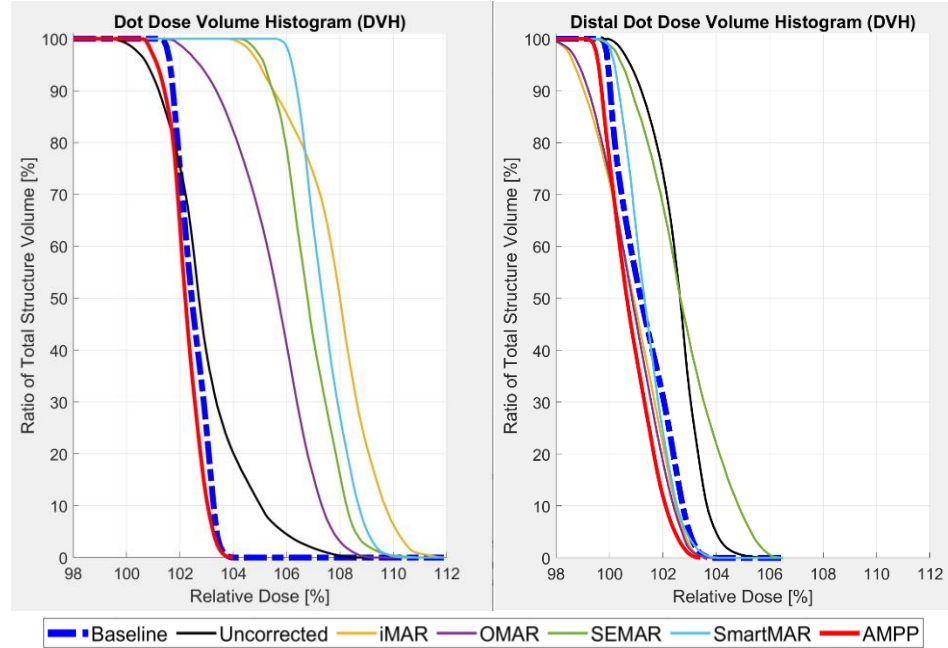


**Figure 21: DVH comparison between the Dot target in its original position and the Dot target in area with less severe metal artifacts. The commercial algorithms provide target coverages closer to the Baseline once the target is moved to a location with less artifacts, indicating success in artifact correction is related to location within the phantom.**

## 5.4 Discussion

Our study demonstrated that uncorrected CT metal artifacts and the commercial MAR algorithms negatively impact the proton dose distributions for all five of the different target shapes and locations. The AMPP-corrected images, however, provided dose distributions that consistently agreed with the baseline dose distribution, for all five targets, as evidenced in Figure 18. None of the commercial MAR algorithms were found to affect the dose distributions in a consistent manner, either by over or underdosing the PTVs. For instance, the

solutions from Philips (OMAR) and Siemens (iMAR) were both found to overdose the Horseshoe shaped target, underdose the Sphere shaped target, and simultaneously underdose (dip in the shoulder region of the target DVH) and overdose (increase in hotspots shown by the larger DVH tail and elevated D0.03cc value) the Bean shaped target. In general, the dose distributions on the MAR corrected and uncorrected image sets underdosed the Sphere target, overdosed the Bean target, and had mixed results for the Horseshoe target. It is also important to note that there were instances that the uncorrected (i.e. full artifact) image set yielded better dose distributions than the ones corrected by some of the commercial solutions. For instance, SmartMAR, iMAR and OMAR on the Sphere target and SEMAR and SmartMAR on the Bean target showed DVH curves that agreed less well with the baseline plan than did the uncorrected image set.

The resulting dose distribution differences noted above between the baseline images and the uncorrected, commercial MAR algorithm-corrected, and AMPP algorithm-corrected, can be further understood in terms of the DVH metrics extracted from all of the proton plans. The CTV coverage provided by the AMPP-corrected image set was consistently the closest to the baseline for all targets analyzed, whereas no clear pattern of agreement was observed for each of the commercial MAR solutions. For example, the iMAR-corrected plan showed an underdosing of the Bean CTV (D99) but also a large overdosing of the Dot CTV (D99). With regards to volume coverage, the Sphere target showed clinically unacceptable ( $V_{100} > 95$ )  $V_{100}$  results from OMAR, iMAR, SmartMAR, and Uncorrected, while AMPP showed identical coverage to the baseline plan. For the Dot, Horseshoe and Bean targets several  $V_{100}$  values were 100% due to the fact that those targets were substantially overdosed, rather than because the artifacts were well managed by the MAR algorithm. The overdosing and creating



of hotspots in the target is further illustrated through the D0.03cc DVH metric. For those same targets, Dot, Bean and Horseshoe, the MAR techniques that showed 100% V100s also showed the largest D0.03cc values (underlined for clarity in Table 10). The same overdosing was not observed for Sphere because it was mostly underdosed and it tended to show mixed results in terms of dose coverage between the baseline results and other plans. In addition, no consistent performance was observed between the commercial algorithms for target heterogeneity. Our in-house stereoscopic artifact management algorithm, AMPP, on the other hand, was in excellent agreement with the baseline metrics as shown in Table 10.

A qualitative comparison of the dose distributions further demonstrated what was observed in the extracted DVH curves and planning metrics. The Horseshoe shaped target showed no major differences in the various dose distributions for the different MAR corrections compared to the baseline, except for a few cold spots inside the target for the uncorrected and SEMAR plans. The Sphere target on the other hand, showed cold spots inside the PTV for all of the plans originating from the commercial MAR solution and uncorrected image sets, consistent with the DVH information. Alternatively, the Bean target isodose lines showed a number of hotspots for all commercial techniques and in some instances, cold spots as well (iMAR and OMAR). In contrast to the largely poor performances of the commercial MAR algorithms analyzed here, AMPP consistently showed dose distributions that overlaid the baseline dose distributions for all of the targets.

These dosimetry evaluations between the ideal baseline image set and the various MAR-corrected image sets suggest that the commercial MAR algorithms' performances vary more with target location and less with target shape. The targets that were located close to the oral cavity, and therefore subject to the more severe artifacts, had dose distributions showing



greater variations (targets Bean, Sphere and Dot were located near the dental fillings in areas that traversed very light and very dark streaks). This is most likely due to the inadequate HU correction obtained with the commercial MARs algorithms, which was sometimes worse than no correction at all.

A possible explanation for why AMPP consistently outperformed the commercial MAR algorithms could be related to the image reconstruction process of the techniques. The majority of current commercial approaches are sinogram-based and manipulate the raw projection data through the identification, deletion, and replacement of corrupted raw data. The imprecise estimation of the removed data can assign incorrect HU values and create additional artifacts and blurring in the final images [10, 11]. Literature has also shown that these MAR approaches are generally not successful at reducing artifacts created by dental fillings [15]. The HN region exhibits a complex geometry with a large number of sharp transitions between the diverse types of tissues present (bone, different organs types, air, etc). In contrast, AMPP does not require the replacement of deleted metal thresholded data with artificially interpolated data. It makes use of a stereoscopic solution to assign accurate HU data obtained from gantry tilted scans that are used to reconstruct a final image free of artifacts posterior to the oral cavity. In addition to improving the visualization of the tissues posterior to the oral cavity, it contains accurate HU values allowing for improved proton dose calculations and distributions observed in this work.

## 5.5 Conclusion

In this study the impact on proton therapy dose distributions from all major commercial MAR algorithms (GE, Siemens, Philips and Toshiba) and a novel in-house stereoscopic technique developed using CT gantry tilts (AMPP) was investigated on a realistic HN anthropomorphic phantom. CT metal artifacts were shown to negatively impact proton dose distributions on all five targets analyzed. The commercial MAR algorithm solutions examined here performed inconsistently throughout all targets when compared to a metal-free baseline. A lack of CTV coverage and increased number of hotspots were observed throughout all commercial solutions. Dose distribution errors were related to proximity to the artifacts, demonstrating the inability of commercial techniques to adequately correct severe artifacts. In contrast, AMPP consistently showed dose distributions that best matched the baseline for all five targets. This is likely due to the fact that AMPP makes use of accurate HU information, as opposed to interpolated data as is done in the commercial algorithms. Future work is planned to expand the proton dosimetry investigation performed here to actual HN patients in an IRB approved study.



## ***Chapter 6 – Discussion***

### **6.1 General Discussion**

An innovative stereoscopic technique was presented in this work and shown to reduce metal artifacts present in the posterior region of HN patients' CT images. The novelty of this technique is characterized by the use of scanner gantry angles to reconstruct a final image free of artifacts posterior to the oral cavity where dental amalgams were located. With the acquisition of an angled CT scan that contains metal, the artifacts produced extend away from the areas of interest, allowing for the attainment of accurate HU information in areas that would otherwise have been affected in a typical 0° angle scan. Two CT scans at opposing angles have been shown to provide enough data to reconstruct a final CT image free of artifacts posterior to the oral cavity that contains accurate HU numbers. In contrast, our stereoscopic technique does not use sinogram manipulated projection data present in most other commercially available MAR algorithms. Furthermore, projection data collected from commercial CT scanners that is used in their MAR algorithms are vendor specific and proprietary, requiring research agreements in order to allow access to them [1]. This limits any user manipulation of the data to enhance the commercial MAR solutions. The algorithm developed in this study is applied in the image space and therefore does not require the need to obtain and manipulate the proprietary raw data from vendors, making it suitable to any CT scanner that allows gantry tilts. In addition to being applicable to any of the CT imagers, the algorithm presented in this work does not require information about the type and size of the metals in the image, making it easily applicable to any patients with dental work. The only information the algorithm requires as input is two angled CT images extracted directly from

the CT console, the selection of a threshold metal HU value, and shear and scaling factors. With this information appropriately provided, the output of the AMPP algorithm is a single final artifact corrected CT image.

The initial testing of the AMPP algorithm's capability was conducted using a simplified geometrical jaw phantom. Testing on the geometrical phantom showed that the AMPP algorithm provides accurate HU number information and generates geometrically/spatially correct structure information, when compared to the metal free baseline CT image. In addition to reconstructing accurate images of the geometrical phantom, AMPP also outperformed a current commercially available artifact reduction method. When compared to SmartMAR, our stereoscopic technique provided superior HU accuracy in the posterior region of the phantom, hence correcting the streaking caused by the dental metal implants better than the commercial solution. The CT image quality analysis was expanded from the geometrical phantom to an anthropomorphic phantom that simulated actual patient anatomy. AMPP once again, regardless of the heterogeneity of the structures within the phantom, provided accurate artifact-corrected CT images. The AMPP algorithm corrected images were further compared to the corrected images from four major CT vendors' MAR algorithms; OMAR from Philips, iMAR from Siemens, SEMAR from Canon, and SmartMAR from GE. It was concluded, based on an analysis of all of the corrected images as compared to an artifact-free baseline image, that the commercial MAR algorithms generally reduced the severity of metal artifacts in the anthropomorphic HN CT scan images, but at varying degrees of accuracy. Aside from showing differences in artifact management between the commercial solutions, the performance of the commercial MAR algorithms were all inferior to that of our in-house-developed AMPP algorithm. The AMPP-corrected images were nearly identical to

the corresponding baseline image set in the posterior region. AMPP as a MAR solution can aid in patient diagnosis for providing a way to physicians to evaluate clearer images that are truthful representations of patients' real anatomy. That in turn would also improve the ability to properly delineate targets and OARs, improving radiation treatment care as whole. AMPP can be applied to any artifacts originating in the oral cavity, but its success in removing artifacts directly inside the oral cavity, however, is limited due to the nature of the angled technique.

In addition to determining AMPP's capability to generate a superior artifact corrected image from other solutions, a proton therapy dosimetry impact was also evaluated for AMPP and all major commercial MAR algorithms using the HN anthropomorphic phantom. It was found that the CT metal artifacts from dental amalgams negatively impact proton dose distributions in which the commercial MAR solutions performed inconsistently while attempting to correct them. The lack of CTV coverage and increased number of hotspots observed throughout commercial solutions was sometimes worse than if no artifact correction was attempted. These dosimetry evaluations between the ideal baseline image set and the various MAR-corrected image sets suggest that the commercial MAR algorithms' performances vary more with target location and less with target shape. The targets that were located close to the oral cavity, and therefore subject to the more severe artifacts, had dose distributions showing greater variations, demonstrating the inability of commercial techniques to adequately correct for severe artifacts, assigning incorrect HU values that impacted on the range of the proton dose calculations. The AMPP-corrected images, however, provided dose distributions that consistently agreed with the baseline dose distribution for all plans analyzed and target locations. The explanation for why AMPP consistently outperformed the

commercial MAR algorithms could be due to it being a stereoscopic solution that assigns accurate HU data obtained from gantry tilted scans, ultimately allowing for the improved proton dose calculations and distributions observed in this work. Unlike the commercial solutions, AMPP does not rely on interpolated data, but rather makes use of the actual HU information unaltered by the artifacts. The correct HU information results in accurate relative linear stopping power ratios to be used in the dose calculations. The dosimetric impact in the photon world is also problematic, from contouring issues to dose calculation inaccuracies. However, the consequences for dose calculation accuracy are particularly relevant in proton therapy because of the strong dependency between accurate representation of HU values and a correct relative linear stopping power prediction, and consequently, target coverage

## **6.2 Response to the Hypothesis**

The hypothesis of this work was:

“A CT artifact management technique can be developed for HN proton therapy delivery that will reduce dental induced artifacts posterior to the oral cavity better than current clinical artifact reduction techniques as measured by an improvement in the visualization of the targets and OARs and, accuracy of the delivered proton dose distribution.”

The first component of the hypothesis was to develop a CT artifact reduction technique to manage metal artifacts in the posterior region of HN such that visualization and image quality of the targets and OARS was better than commercial solutions. The results of Chapter 3 and 4 show that the stereoscopic AMPP technique developed was suitable for CT imaging and allowed for the successful reconstruction of artifact corrected images in the posterior

region of a HN phantom than the other commercial MAR algorithms. The results described in Chapter 3 revealed that our technique outperformed the commercial algorithm SmartMAR providing better HU agreement with the metal-free baseline on a geometrical phantom. Chapter 4 results presented a more complete image quality evaluation of the in-house technique developed here and the 4 currently available major commercial algorithms; OMAR (Philips Healthcare System), SmartMAR (GE Medical Systems), iMAR (Siemens Healthcare) and SEMAR (Canon) on a heterogeneous anthropomorphic phantom. Although the commercial algorithms generally reduced the severity of the metal artifacts to a certain degree, their performances were all inferior to that of our in-house-developed AMPP algorithm. The AMPP algorithm produced superior metal corrected images that presented no geometrical distortion and accurate HU values when compared to a metal free baseline as compared to other MAR solutions.

The last component of the hypothesis was to demonstrate that the AMPP algorithm corrected image set would result in superior proton dose distributions when compared to the alternative commercial solutions. The results presented in Chapter 5 demonstrated the impact on proton therapy dose distributions from all major commercial MAR algorithms (GE, Siemens, Philips and Canon) and our novel in-house stereoscopic technique. The commercial MAR algorithm solutions examined here performed poorer and inconsistently for all target sizes/locations posterior to the dental implants, while AMPP consistently resulted in proton dose distributions that best matched the baseline. Since our AMPP correction algorithm outperformed all of the commercial algorithms in all aspects investigated in our study, the hypothesis is supported.



## 6.3 Future Studies

### 6.3.1 Algorithm Application and Expansion

The stereoscopic artifact reduction technique developed in this work was originally designed for HN cases but also has the potential for improvement in artifact management and imaging of anatomical structures in other areas of the body that have metal inserts (eg, surgical clips, prostheses). Approximately 200,000 lumbar spine operations are performed annually in the United States where the metal hardware surgically implanted within a patient can present limitations in any CT imaging procedures that involve the area with the implants [2]. With the increasing use of metallic instrumentation, physicians are being forced to rely on plain radiography and myelography for the evaluation of these patients [2]. Given the results obtained with AMPP in the HN region and the general posterior location of spinal rods, it is likely that spine metal artifacts would be considerably improved with the use of our newly developed technique, without any need for algorithm revision. Brain surgical clips and hip prosthesis however, can be more centrally located inside the human body. For cases like that, AMPP can be further expanded to also eliminate artifacts in the anterior region, in addition to the posterior region of the body. The same concept using gantry angles can be mirrored to the anterior region. A final image can be fused together using the areas of the CT image set that contain no artifacts, improving the image posterior and anterior to the artifacts; nose and chin in the case of HN (**Error! Reference source not found.**Figure 22). Due to the nature of the technique, artifacts orthogonal to the gantry tilt and involved by the metal inserts cannot be addressed. That means the artifacts in between the hip prosthesis cannot be improved and will remain showing the dark streak due to severe photon starvation.

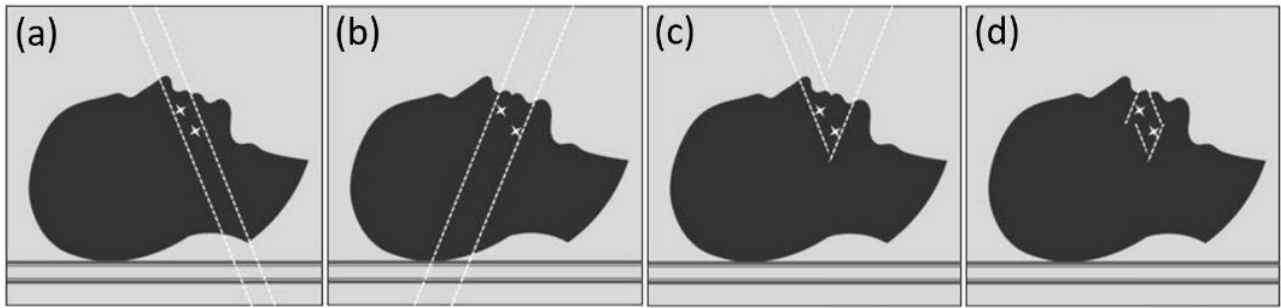


**Figure 22: Diagram representing a HN patient with metal in the oral cavity showing the extent of the artifacts (dashed lines) on angled CT scans (a-b) and on the final AMPP reconstructed image (c). (d) shows the technique once expanded to also eliminate artifacts in the anterior region (nose and chin) in addition to the posterior region.**

It is also possible to further the correction and apply the vendor's MAR algorithm available after AMPP is applied to the image set in the attempts of correcting the photon starvation in between the metal (and inside the oral cavity in HN cases). However, due to the sinogram manipulation nature of the commercial MAR algorithms, the entire CT slice that contains metal will be affected, possibly altering the HU information of areas already accurately corrected with AMPP. Therefore, additional studies would be required in order to evaluate the accuracy of the HU information in the event of both algorithms being applied together. It is important to note that the order in which the MAR algorithms are implemented is crucial to preserve the best HU assignment in the image. AMPP should be applied first so that the main retrieval of HU information is based on true HU numbers and the commercial sinogram manipulation following is used to only further improve the image. The idea being that the less interpolation required will imply in less uncertainty in the final image set. Another important consideration in the co-implementation of AMPP with a commercial MAR algorithm is that it would require the ability to perform both algorithms at the CT console (in

the appropriate order). This could produce a significant obstacle due to the requirement of vendor-institution agreements to allow for the correct implementation.

### **6.3.2 Patient Studies**

The focus of this work was to investigate the success of the AMPP algorithm on an anthropomorphic phantom. The phantom was built with tissue equivalent materials, human bones and air cavities in order to try to mimic as closely as possible a real patient. However, human HN anatomy and target shape/location are even more complex and elaborate than simulated with our HN phantom. The HN region presents with numerous different organs, several of which are radiation sensitive structures, and tissue interfaces in close proximity to potential disease. Therefore, future studies are planned to investigate the performance of the AMPP technique on actual patient anatomy, assessing the improvements in visualization of tissues. In conjunction to image quality studies, the radiation dosimetry impact in patients can also be investigated. Inter- and intra-observer contouring variability, target coverage and dose calculation accuracy can be examined using our in-house technique in comparison to current clinical methods. Assessment of required treatment planning times will be performed since the AMPP technique would negate the need for dosimetrists to manually override HU values in CT images affected by metal artifacts. In addition to improvements in image quality and proton dose distributions, patient motion in between scans may also need to be examined. The scans will be separated by a few seconds and the patient's breathing or moving of the tongue may change the scans and affect the fusion of the final corrected images.

## 6.4 Clinical Implementation

Once AMPP is proven safe and effective for artifact removal in HN patients, the technique can be implemented for regular clinical use. For both diagnostic and therapeutic cases, patients that presented with metal dental fillings would acquire 2 scans at opposing CT gantry angles. The work performed here suggests that a  $15^\circ$  gantry angle tilt is enough to attain substantial artifact reduction in the posterior region of the patient. The scanner console should have the algorithm installed so that once both images are acquired the final artifact reduced image can be reconstructed and displayed for physician approval. If vendor agreements cannot be established to have the AMPP protocol installed along with their software, both image sets can be extracted and post processed at an office computer at the institution. The algorithm's execution time is dependent on the number of slices in each image set, but on average takes 40 seconds to run, making it feasible to be readily implemented into most clinical workflows.

The reconstruction of the artifact-free image requires two scans instead of one, which may deliver additional dose to the patient. The cost of any extra dose ( $< 10$  cGy) would need to be weighed against improved image quality and associated benefit to diagnosis and/or radiotherapy treatment of patients. The comparison to other MAR solutions shown in this work however, is indicative of the potential benefit behind our approach. For radiotherapy patients in particular, this one-time extra dose is negligible ( $< 0.1\%$ ) compared with the total treatment and imaging dose already committed to HN cancer patients and can provide dose distributions nearly identical to a metal free baseline.

## ***Chapter 7 – Conclusion***

Metal fillings can create severe imaging artifacts when undergoing CT imaging. These artifacts can seriously affect disease diagnosis as well as the subsequent radiation treatment planning. In this study, a novel stereoscopic MAR algorithm was developed using CT gantry tilts and evaluated on a geometrical phantom. The algorithm developed here offered the improvement of not requiring the replacement of deleted metal thresholded data with artificially interpolated data making use of accurate HU data obtained from two different scans. The in-house algorithm was compared to 4 currently available major commercial algorithms; OMAR (Philips Healthcare System), SmartMAR (GE Medical Systems), iMAR (Siemens Healthcare) and SEMAR (Canon) using an anthropomorphic head and neck phantom. Although commercial MAR algorithms generally reduced the severity of metal artifacts in head and neck CT scans, their performance was inferior to AMPP. The AMPP algorithm has the potential to be broadly implemented, improve visualizations in patient anatomy and provide accurate, non-interpolated HU information. In addition to improving visualization, a proton therapy dosimetric analysis showed that AMPP provided the best image set for treatment planning calculations, providing plans most comparable to a metal free baseline, likely due to the fact that AMPP makes use of accurate HU information, as opposed to interpolated data as is done in the commercial algorithms.

## *Appendix A*

### **Untilting of CT Image CT MATLAB Code**

%%%% Image Reconstruction pre AMPPing - Tilted CT to axial format + Distortion Corrections (& small

%%%% modifications - slice selection, metadata assignment and metadata editing)

%%%% Daniela Branco 2017/18

%%%% Program reads in a CT scan as a volume with its metadata. It will then

%%%% untilt the volume using an affine transformation (shear factor needs

%%%% to be determined). The untilted creates extra slices that need to me

%%%% deleted so that each metadata file can be attached to the final

%%%% untilted volume of images. Metadata is then modified to representing a

%%%% perpendicular scan and pixel numbers are corrected to represent HUs.

%%%% Volume is saved as a DICOM set of separate images.

% Reading CT images

close all

clear all

clc

addpath(genpath('Y:\MDACC\PhD Thesis\Research\MATLAB'));

[metadata, I] = CTread('Y:\PhD Thesis\Research\CT Images\ANTHROPOMORPHIC PHANTOM\RED\_DB\_INSERT\GE Robustness Study\Slice\S15\_120\_slice1.25\');

%% OPTIONAL - Untilting of sample Slice - determine angle (a variable or shear factor)

% close all

% figure

% sagittalView = I(:,60,:);

% sagittalView2D = squeeze(sagittalView);

```

% imagesc(sagittalView2D); impixelinfo

% %Shear Factor

% a = 0.06;      %Inferior tilts require a negative _a
%                Superior tilts require a positive _a

% t = [1 0 0 ; a 1 0; 0 0 1];

% tform = affine2d(t);

% Untilted_sagittalView2D = imwarp(sagittalView2D,tform,'Interp','linear');

% Untilted_sagittalView2D(Untilted_sagittalView2D < 50) = 24;

% figure

% imagesc(Untilted_sagittalView2D), impixelinfo

% title([a]);

%% Untilting of Volume

a = 0;

b = -0.115; %Shear Factor

t = [1 0 a 0 ; 0 1 b 0; 0 0 1 0; 0 0 0 1];

tform = affine3d(t);

Perpendicular_Image_Volume = imwarp(I,tform,'Interp','linear');

%% OPTIONAL - Sample Images from untitled Volume

% close all

% % Sagittal VIEW

% % figure

%                Untilted_sagittalView3Dsqueeze
squeeze(Perpendicular_Image_Volume(:,200,:));

% % imagesc(Untilted_sagittalView3Dsqueeze), impixelinfo

%

% % Axial VI

```

```

% figure

% imagesc(Perpendicular_Image_Volume(:,:,24)), impixelinfo

%

%

%% Selecting Phantom slices

%

%
        Perpendicular_Image_Volume_final(:,:,1:98)
Perpendicular_Image_Volume(:,:,24:121);
=

%% Metadata Editing

for i = 1:size(Perpendicular_Image_Volume,3)

    metadata{i}.ImageOrientationPatient = [1;0;0;0;1;0];

end

%% OPTIONAL - Deleting extra slices

% for i = 1:14

%     Perpendicular_Image_Volume(:,:,i) = [];

% end

%% Scalling Transformation

%

% s = 0.989;    %Distortion Factor - based on scan angle

% t = [1 0 0 0; 0 s 0 0; 0 0 1 0; 0 0 0 1];

% tform = affine3d(t);

%
        Perpendicular_Image_Volume_final_scale
imwarp(Perpendicular_Image_Volume_final,tform);
=

%

% % Adding air rows

% k = floor((1-s)*512);    %Number of rows to be added to complete 512 pixels on
the y direction

```



```

%
% for i = 1:size(Perpendicular_Image_Volume_final_scale,3)

%           Perpendicular_Image_Volume_final_scale_FINAL(:,i)      =
padarray(Perpendicular_Image_Volume_final_scale(:,i),k,24,'pre');

%
Perpendicular_Image_Volume_final_scale_FINAL(Perpendicular_Image_Volume_final_sc
ale_FINAL < 50) = 24;

% end

%

%% Scalling Transformation

s = 0.965;    %Distortion Factor - based on scan angle

t = [1 0 0 0; 0 s 0 0; 0 0 1 0; 0 0 0 1];

tform = affine3d(t);

Perpendicular_Image_Volume_final_scale                                =
imwarp(Perpendicular_Image_Volume,tform);

% Adding air rows

k = floor((1-s)*512);    %Number of rows to be added to complete 512 pixels on the
y direction

for i = 1:size(Perpendicular_Image_Volume_final_scale,3)

    Perpendicular_Image_Volume_final_scale_FINAL(:,i)                =
padarray(Perpendicular_Image_Volume_final_scale(:,i),k,24,'pre');

Perpendicular_Image_Volume_final_scale_FINAL(Perpendicular_Image_Volume_final_sc
ale_FINAL < 50) = 24;

end

%% Write the matrix in DICOM format to be uploaded into TPSs

for i = 1:size(Perpendicular_Image_Volume_final_scale_FINAL,3)

```

```

dicomwrite(Perpendicular_Image_Volume_final_scale_FINAL(:,:,i),['S15_slice125_untilted_
',num2str(i)
'.dcm'],metadata{i},'CreateMode','Copy','MultiframeSingleFile','False','UseMetadataBitDepths',true');

    end

    % for i = 1:size(Perpendicular_Image_Volume,3)

    %
dicomwrite(Perpendicular_Image_Volume(:,:,i),['I15_ChinDown_geoUncorrected_'
num2str(i)
'.dcm'],metadata{i},'CreateMode','Copy','MultiframeSingleFile','False','UseMetadataBitDepths',true');

    % end

    %%%%%%%%%%% END
%%%%%%%%%%

%% OPTIONAL - Visualize images - scrollsubplot

    % figure

    % for k = 1:166

    %     subplot(1,1,k)

    %     imagesc(Untilted_saggitalView3D_axial(:,:,k));

    %     colormap gray

    % end

    %% HU correction (Eclipse does this again so DO NOT DO this step if importing
images into it)

    % Perpendicular_Image_Volume_final = (Perpendicular_Image_Volume_final *
metadata{1}.RescaleSlope) + metadata{1}.RescaleIntercept;

    %

    % imagesc(Perpendicular_Image_Volume_final(:,:,15)), impixelinfo

```

## AMPP MATLAB Code

```
%%%%%%%% AMPP it up! - Final combination of images to produce artifact free
%%%%%%%% posterior image
%%%%%%%% Daniela Branco 2017/18

%%%%%%%% Program will read superior and inferior tilted image sets and find the
%%%%%%%% reference point (midpoint between artifacts) so that the images can be
%%%%%%%% then be added properly and saved as DICOM separate images.

% Reading CT scans - superior and inferior tilts

clear all

close all

clc

addpath(genpath('E:\MDACC\PhD Thesis\Research\MATLAB'));

[metadata_superior,I_superior] = CTread('Y:\PhD Thesis\Research\CT
Images\ANTHROPOMORPHICteeth\Untilted\red_mixedTeeth_S15\');

[metadata_inferior,I_inferior] = CTread('Y:\PhD Thesis\Research\CT
Images\ANTHROPOMORPHICteeth\Untilted\red_mixedTeeth_I15\');

%%%%%%%% Finding INFERIOR scan half point in phantom

nSlices_I_inferior = size(I_inferior,3);

nSlices_I_superior = size(I_superior,3);
```

```

for i = 1:nSlices_I_inferior
    [row,col] = find(I_inferior(:,i)>1000);
    if ~isempty(row)
        start_slice_inf = i;
        break
    end
end

for i = nSlices_I_inferior:-1:1
    [row,col] = find(I_inferior(:,i)>1000);
    if ~isempty(row)
        end_slice_inf = i;
        break
    end
end

reference_slice_inferior = floor((start_slice_inf + end_slice_inf)/2);    %REFERENCE
SLICE INFERIOR

%reference_slice_inferior = 24;

%% Finding SUPERIOR scan half point in phantom
for i = 1:nSlices_I_superior
    [row,col] = find(I_superior(:,i)>1000);
    if ~isempty(row)
        start_slice_sup = i;
        break
    end
end
end

```

```

for i = nSlices_I_superior:-1:1

    [row,col] = find(I_superior(:,i)>1000);
    if ~isempty(row)
        end_slice_sup = i;
        break
    end
end

reference_slice_superior = floor((start_slice_sup + end_slice_sup)/2);
%REFERENCE SLICE SUPERIOR

%reference_slice_superior = 24;

%% Finding ANTERIOR scan point in phantom on SUPERIOR scan
nSagSlices_I_inferior = size(I_inferior,2);
nSagSlices_I_superior = size(I_superior,2);

for i = 1:nSagSlices_I_inferior

    [row,col] = find(I_inferior(i,:)>30000);
    if ~isempty(row)
        start_SagSlice_inf = i;
        break
    end
end

reference_SagittalSlice_inferior = start_SagSlice_inf; %REFERENCE SLICE
SAGITTAL VIEW INFERIOR

```

```

%% Finding ANTERIOR scan point in phantom on INFERIOR scan
for i = 1:nSagSlices_I_superior
    [row,col] = find(I_superior(i,:,:)>30000);
    if ~isempty(row)
        start_SagSlice_sup = i;
        break
    end
end

reference_SagittalSlice_superior = start_SagSlice_sup;    %REFERENCE SLICE
SAGITTAL VIEW SUPERIOR

%% Creates the Artifact Corrected Matrix

for k = 1:1:reference_slice_inferior
    ArtifactCorrectedImage_inf(:, :,k) = I_inferior(:, :,k);
end
ArtifactCorrectedImage_inf(1:(reference_SagittalSlice_superior),:,:) = [];

for z = reference_slice_superior:nSlices_I_superior
    ArtifactCorrectedImage_sup(:, :,z) = I_superior(:, :,z);
end
ArtifactCorrectedImage_sup(:, :,1:(reference_slice_superior-1)) = [];
ArtifactCorrectedImage_sup(1:reference_SagittalSlice_superior,:,:) = [];

%%

```

```

for z = 1:1:reference_SagittalSlice_superior
    ArtifactCorrectedImage_sagInf(z, :, :) = I_inferior(z, :, :);
end

ArtifactCorrectedImage_sagInf(:, :, 1:reference_slice_inferior) = [];

for z = 1:1:reference_SagittalSlice_superior
    ArtifactCorrectedImage_sagSup(z, :, :) = I_superior(z, :, :);
end

ArtifactCorrectedImage_sagSup(:, :, (reference_slice_superior-1):nSlices_I_superior) =
[];

%%

ArtifactCorrectedImage_post                                =
cat(3, ArtifactCorrectedImage_inf, ArtifactCorrectedImage_sup);

ArtifactCorrectedImage_post(:, :, 1:3) = [];

%%

ArtifactCorrectedImage_ant                                =
cat(3, ArtifactCorrectedImage_sagSup, ArtifactCorrectedImage_sagInf);

%% ArtifactCorrectedImage_ant(:, :, (size(ArtifactCorrectedImage_ant, 3)+1)) = [24];

ArtifactCorrectedImage_FULL = zeros(512, 512, 41);

ArtifactCorrectedImage_FULL                                =
cat(1, ArtifactCorrectedImage_ant, ArtifactCorrectedImage_post);

%% Write the matrix in DICOM format to be uploaded into TPSs

%% for i = 1:size(ArtifactCorrectedImage_ant, 3)

```





## *Appendix B*

Slice							
Imaging	Scanner	Energy	Thickness			Phantom	Recon
Technique	Vendor	(kVp)	(mm)	mA	SFOV	Head Tilt	Type
Uncorrected	Siemens	120	2	300	Head	No	Standard
OMAR	Philips	120	3	300	Head	No	Standard
SEMAR	Toshiba	120	3	140	Head	No	Standard
iMAR	Siemens	120	2	200	Head	No	Standard
SmartMAR	GE	120	2.5	320	Head	No	Standard
AMPP	Siemens	120	2	300	Head	No	Standard

Table: Scan parameters for data analysis of CT number accuracy and artifact severity.

Slice							
Imaging	Scanner	Energy	Thickness				Recon
Parameter	Vendor	(kVp)	(mm)	mA	SFOV	Head Tilt	Type
Energy, 100 kVp	GE	100	2.5	500	Head	No	Standard
Energy, 120 kVp	GE	120	2.5	500	Head	No	Standard
Energy, 140 kVp	GE	140	2.5	500	Head	No	Standard
Slice Thickness	GE	120	1.25	500	Head	No	Standard
SFOV	GE	120	2.5	500	Small Body	No	Standard
Head Tilt	GE	120	2.5	500	Head	Yes	Standard
Recon Algorithm	GE	120	2.5	500	Head	No	Detail

Table: Imaging parameters of the AMPP algorithm for the robustness analysis. Each metal scan was repeated without the metal amalgam teeth with the same parameters to obtain the baselines.

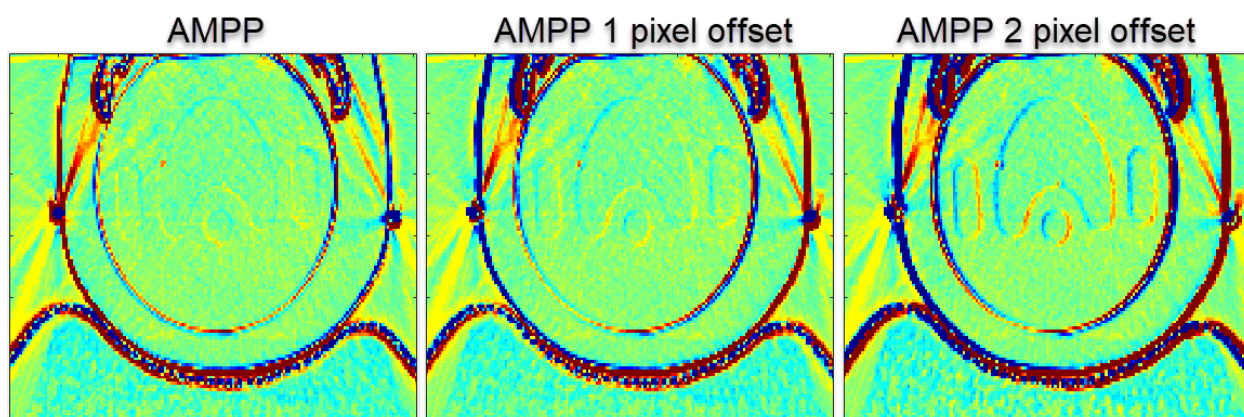


Figure: (a-c) HU error maps show differences among the original AMPP-corrected images (a), an AMPP-corrected image with a misalignment of 1 pixel (b), and an AMPP-corrected image with a misalignment of 2 pixels (c), as compared with corresponding baseline images, demonstrating the consequences of poor image registration. It is possible to see the outline of the target and OARs as the pixel offset increases.

## ***Chapter 8 – Bibliography***

1. Cleveland J, Junger M, Saraiya M, Markowitz L, Dunne E, Epstein J. *The connection between human papillomavirus and oropharyngeal squamous cell carcinomas in the United States*. The Journal of the American Dental Association, 2011. 142(8): p. 915-924.
2. NCI, N.C.I. *Head and Neck Cancers*. 8/16/2017]; Available from: <https://www.cancer.gov/types/head-and-neck/head-neck-fact-sheet>.
3. Gupta B, Johnson N, Kumar N, *Global Epidemiology of Head and Neck Cancers: A Continuing Challenge*. Oncology, 2016. 91(1): p. 13-23.
4. Tuyns A, Estève J, Raymond L, Berrino F, Benhamou E, Blanchet F, Boffetta P, Crosignani P, del Moral A, Lehmann W, *Cancer of the larynx/hypopharynx, tobacco and alcohol: IARC international case-control study in Turin and Varese (Italy), Zaragoza and Navarra (Spain), Geneva (Switzerland) and Calvados (France)*. Int J Cancer, 1988. 41(4): p. 483-91.
5. Winn D, *Epidemiology of cancer and other systemic effects associated with the use of smokeless tobacco*. Adv Dent Res, 1997. 11(3): p. 313-21.
6. Wojciech Golusiński, René L, Andreas Dietz, *HPV Infection in Head and Neck Cancer*. Vol. 206. 2017: Springer.
7. Sand L, Jalouli J, Larsson P, Hirsch, J, *Prevalence of Epstein-Barr virus in oral squamous cell carcinoma, oral lichen planus, and normal oral mucosa*. Oral Surg Oral Med Oral Pathol Oral Radiol Endod, 2002. 93(5): p. 586-92.
8. Holmes D, M Slomka, J Mahabir, S Beeravolu, S Emani, *Is dental care utilization associated with oral cavity cancer in a large sample of community-based United States residents?* Community Dentistry and Oral Epidemiology, 2009. 37(2): p. 134-142.

9. Wake M, *The urban/rural divide in head and neck cancer--the effect of atmospheric pollution*. Clin Otolaryngol Allied Sci, 1993. 18(4): p. 298-302.
10. Moulin J, Mur J, Wild P, Perreaux J, Pham Q, *Oral cavity and laryngeal cancers among man-made mineral fiber production workers*. Scand J Work Environ Health, 1986. 12(1): p. 27-31.
11. Liebling T, Rosenman K, Pastides H, Griffith R, Lemeshow S. *Cancer mortality among workers exposed to formaldehyde*. American Journal of Industrial Medicine, 1984. 5(6): p. 423-428.
12. Rossing M, Vaughan L, McKnight B, *Diet and pharyngeal cancer*. International Journal of Cancer, 1989. 44(4): p. 593-597.
13. Sánchez M, Martínez C, Nieto A, Castellsagué X, Quintana M, Bosch F, Muñoz N, Herrero R, Franceschi S, *Oral and oropharyngeal cancer in Spain: influence of dietary patterns*. European Journal of Cancer Prevention, 2003. 12(1): p. 49-56.
14. Boeing H, Dietrich T, Hoffmann K, Pischon T, Ferrari P, Lahmann PH, Boutron-Ruault MC, Clavel-Chapelon F, Allen N, Key T, Skeie G, Lund E, Olsen A, Tjønneland A, Overvad K, Jensen MK, Rohrmann S, Linseisen J, Trichopoulou A, Bamia C, Psaltopoulou T, Weinehall L, Johansson I, Sánchez MJ, Jakszyn P, Ardanaz E, Amiano P, Chirlaque MD, Quirós JR, Wirfalt E, Berglund G, Peeters PH, van Gils CH, Bueno-de-Mesquita HB, Büchner FL, Berrino F, Palli D, Sacerdote C, Tumino R, Panico S, Bingham S, Khaw KT, Slimani N, Norat T, Jenab M, Riboli E. *Intake of fruits and vegetables and risk of cancer of the upper aero-digestive tract: the prospective EPIC-study*. Cancer Causes Control, 2006. 17(7): p. 957-69.

15. Winn D, *Diet and nutrition in the etiology of oral cancer*. Am J Clin Nutr, 1995. 61(2): p. 437s-445s.
16. Moore C, Flynn M, and Greenberg R, *Evaluation of size in prognosis of oral cancer*. Cancer, 1986. 58(1): p. 158-62.
17. Kramer S, Marcial V, Pajak T, MacLean C, Davis L, *Prognostic factors for loco/regional control and metastasis and the impact on survival*. Int J Radiat Oncol Biol Phys, 1986. 12(4): p. 573-8.
18. Lawrence J, *Proton irradiation of the pituitary*. Cancer, 1957. 10(4): p. 795-798.
19. Koehler A, Schneider R, and Sisterson J, *Flattening of proton dose distributions for large-field radiotherapy*. Medical Physics, 1977. 4(4): p. 297-301.
20. *History of Proton Therapy*. Available from: <http://www.mdanderson.org/patient-andcancer-information/proton-therapy-center/what-is-proton-therapy/history-of-protontherapy/index.html>.
21. Sandberg G, *Electron Beam Flattening with an Annular Scattering Foil*. IEEE Transactions on Nuclear Science, 1973. 20(3): p. 1025-1026.
22. Das I, Paganetti H, *Principles and Practice and Proton Beam Therapy*. Vol. 37. 2015.
23. Bassal M, Mertens A, Taylor L, Neglia J, Greffe B, Hammond S, Ronckers C, Friedman D, Stovall M, Yasui Y, Robison L, Meadows A, Kadan-Lottick N, *Risk of selected subsequent carcinomas in survivors of childhood cancer: a report from the Childhood Cancer Survivor Study*. J Clin Oncol, 2006. 24(3): p. 476-83.
24. Oeffinger K, Mertens A, Sklar C, Kawashima T, Hudson M, Meadows A, Friedman D, Marina N, Hobbie W, Kadan-Lottick N, Schwartz C, Leisenring W, Robison L. *Chronic*

*Health Conditions in Adult Survivors of Childhood Cancer*. New England Journal of Medicine, 2006. 355(15): p. 1572-1582.

25. Lawrence T, Haffty B, and Harris J, *Milestones in the Use of Combined-Modality Radiation Therapy and Chemotherapy*. Journal of Clinical Oncology, 2014. 32(12): p. 1173-1179.

26. Moreno A, Frank S, Garden A, Rosenthal D, Fuller C, Gunn G, Reddy J, Morrison W, Williamson T, Holliday E, Phan J, Blanchard P. *Intensity modulated proton therapy (IMPT) - The future of IMRT for head and neck cancer*. Oral Oncol, 2019. 88: p. 66-74.

27. Liebl Jakob P, Zhu Mingyao, Winey B, *The influence of patient positioning uncertainties in proton radiotherapy on proton range and dose distributions*. Medical Physics, 2014. 41(9): p. 091711-n/a.

28. Park P, Cheung J, Zhu X, Lee A, Sahoo N, Tucker S, Liu W, Li H, Mohan R, Court L, Dong L. *Statistical Assessment of Proton Treatment Plans Under Setup and Range Uncertainties*. International Journal of Radiation Oncology Biology Physics, 2013. 86(5): p. 1007-1013.

29. Uwe Schneiderdag E, Lomax A, *The calibration of CT Hounsfield units for radiotherapy treatment planning*. Physics in Medicine and Biology, 1996. 41(1): p. 111-124.

30. Summers P, Neihart J, Blatnica A, Sahoo N, Gillin M, Followill D, Ibbott G. *Relative stopping power measurements to aid in the design of anthropomorphic phantoms for proton radiotherapy*. J Appl Clin Med Phys, 2014. 15(2): p. 4523.

31. Moyers M, Sardesai M, Sun S, Miller D, *Water equivalence of various materials for 155 to 250 MeV protons*. Med. Phys, 1992. 19(3): p. 829.

32. Constantinou C, Harrington J, L DeWerd, *An electron density calibration phantom for CT-based treatment planning computers*. Medical Physics, 1992. 19(2): p. 325-327.
33. Indra Das, Paganetti H. *Principles and Practice of Proton Beam Therapy*. Vol. 37. 2015: Medical Physics Publishing.
34. Bushberg J, Leidholdt E, Boone J, *The Essential Physics of Medical Imaging*. 2001: Lippincott Williams and Wilkins.
35. Herman G, *Correction for beam hardening in computed tomography*. Physics in Medicine & Biology, 1979. 24(1): p. 81.
36. Schaffner B, Pedroni E, *The precision of proton range calculations in proton radiotherapy treatment planning: experimental verification of the relation between CT-HU and proton stopping power*. Physics in Medicine and Biology, 1998. 43.
37. O'Daniel J, Rosenthal D, Garden A, Barker J, Ahamad A, Ang K, Asper J, Blanco A, de Crevoisier R, Holsinger F, Patel C, Schwartz D, Wang H, Dong L. *The Effect of Dental Artifacts, Contrast Media, and Experience on Interobserver Contouring Variations in Head and Neck Anatomy*. American Journal of Clinical Oncology, 2007. 30(2): p. 191-198.
38. Kim Y, Tomé W, Bal M, McNutt T, Spies L. *The impact of dental metal artifacts on head and neck IMRT dose distributions*. Radiotherapy and Oncology, 2006. 79(2): p. 198-202.
39. Mail N, Albarakati Y, Ahmad Khan, Saeedi F, Safadi N, Al-Ghamdi S, Saoudi A. *The impacts of dental filling materials on RapidArc treatment planning and dose delivery: Challenges and solution*. Medical Physics, 2013. 40(8): p. 081714-n/a.

40. Newhauser W, Giebeler A, Langen KM, Mirkovic D, Mohan R. *Can megavoltage computed tomography reduce proton range uncertainties in treatment plans for patients with large metal implants?* Physics in medicine and biology, 2008. 53(9): p. 2327-2344.
41. Richard P, Sandison G, Dang Q, Johnson B, Wong T, Parvathaneni U. *Dental amalgam artifact: Adverse impact on tumor visualization and proton beam treatment planning in oral and oropharyngeal cancers.* Practical Radiation Oncology, 2015. 5(6): p. e583-e588.
42. Jessie Y, Kerns J, Nute J, Liu X, Balter P, Stingo F, Followill D, Mirkovic D, Howell R, Kry S. *An evaluation of three commercially available metal artifact reduction methods for CT imaging.* Physics in Medicine & Biology, 2015. 60(3): p. 1047.
43. Ge W, Snyder D, O'Sullivan J, Vannier M. *Iterative deblurring for CT metal artifact reduction.* IEEE Transactions on Medical Imaging, 1996. 15(5): p. 657-664.
44. Zhao S, Robertson D, Wang G, Whiting B, Bae K. *X-ray CT metal artifact reduction using wavelets: an application for imaging total hip prostheses.* IEEE Transactions on Medical Imaging, 2000. 19(12): p. 1238-1247.
45. Man B, Nuyts J, Dupont P, Marchal G, Suetens P. *An iterative maximum-likelihood polychromatic algorithm for CT.* IEEE Transactions on Medical Imaging, 2001. 20(10): p. 999-1008.
46. Jikun W, Sandison G, Hsi W, Ringor M, Lu X. *Dosimetric impact of a CT metal artefact suppression algorithm for proton, electron and photon therapies.* Physics in Medicine & Biology, 2006. 51(20): p. 5183.



47. Andersson K, Ahnesjö A, Dahlgren C, *Evaluation of a metal artifact reduction algorithm in CT studies used for proton radiotherapy treatment planning*. Journal of Applied Clinical Medical Physics, 2014. 15(5): p. 112-119.
48. Paganetti H, *Range uncertainties in proton therapy and the role of Monte Carlo simulations*. Physics in Medicine and Biology, 2012. 57(11): p. R99-R117.
49. Kalender W, Hebel R, Ebersberger J, *Reduction of CT artifacts caused by metallic implants*. Radiology, 1987. 164(2): p. 576-577.
50. Meyer E, Raupach R, Lell M, Schmidt B, Kachelriess M. *Normalized metal artifact reduction (NMAR) in computed tomography*. Medical Physics, 2010. 37(10): p. 5482-5493.
51. Bal M, L Spies, *Metal artifact reduction in CT using tissue-class modeling and adaptive prefiltering*. Medical Physics, 2006. 33(8): p. 2852-2859.

## Chapter 1

1. Herman G. Correction for beam hardening in computed tomography. Phys Med Bio. 1977; 24(1).
2. O'Daniel J, Rosenthal D, Garden A, Barker J, Ahamad A, Ang K, Asper J, Blanco A, de Crevoisier R, Holsinger F, Patel C, Schwartz D, Wang H, Dong L. The Effect of Dental Artifacts, Contrast Media, and Experience on Interobserver Contouring Variations in Head and Neck Anatomy. Am. J. Clin. Oncol. 2007; 30(2): 191-198.
3. Kim Y, Tomé W, Bal M, McNutt T, Spies L. The impact of dental metal artifacts on head and neck IMRT dose distributions. Radiother Oncol. 2006; 79(2): 198-202.

4. Mail N, Albarakati Y, Ahmad Khan, Saeedi F, Safadi N, Al-Ghamdi S, Saoudi A. The impacts of dental filling materials on RapidArc treatment planning and dose delivery: Challenges and solution. *Med Phys*. 2013; 40(8): 817141-8171411.
5. Huang J, Followill D, Howell R, Liu X, Mirkovic D, Stingo F, Kry S. Approaches to reducing photon dose calculation errors near metal implants. *Med Phys*. 2016; 43(9): 5117-5130.
6. Wei J, Sandison G, Wen-Chien H, Ringor M, Lu X. Dosimetric impact of a CT metal artefact suppression algorithm for proton, electron and photon therapies. *Phys Med Bio*. 2006; 51(20): 5183-5197.
7. Schaffner B, Pedroni E. The precision of proton range calculations in proton radiotherapy treatment planning: experimental verification of the relation between CT-HU and proton stopping power. *Phys Med Bio*. 1998; 43: 1579–1592.
8. Das I, Paganetti H. *Principles and Practice and Proton Beam Therapy*. 2015.
9. Paganetti H, Range uncertainties in proton therapy and the role of Monte Carlo simulations. *Phys Med Bio*. 2012; 57(11): R99-R117.
10. Newhauser W, Giebeler A, Langen KM, Mirkovic D, Mohan R. Can megavoltage computed tomography reduce proton range uncertainties in treatment plans for patients with large metal implants? *Phys Med Bio*. 2008; 53(9): 2327-2344.
11. Kim C, Pua R, Lee C, Choi D, Cho B, Lee S, Cho S, Kwak J. An additional tilted-scan-based CT metal-artifact-reduction method for radiation therapy planning. *J Appl Clin Med Phys*. 2019; 20(1): 237-249.

12. Richard P, Sandison G, Dang Q, Johnson B, Wong T, Parvathaneni U. Dental amalgam artifact: Adverse impact on tumor visualization and proton beam treatment planning in oral and oropharyngeal cancers. *Pract Radiat Oncol*. 2015; 5(6): 583-588.
13. Axente M, Paidi A, Von Eyben R, Zeng C, Bani-Hashemi A, Krauss A, Hristov D. Clinical evaluation of the iterative metal artifact reduction algorithm for CT simulation in radiotherapy. *Med Phys*. 2015; 42(3): 1170-1183.
14. Zhang D. Single Energy Metal Artifact Reduction A Reliable Metal Management Tool in CT. White Paper, 2017.
15. Metal Artifact Reduction for Orthopedic Implants (O-MAR). White Paper, 2013.
16. Smart Metal Artifact Reduction (MAR). White Paper, 2013.
17. Huang J, Kerns J, Nute J, Liu X, Balter P, Stingo F, Followill D, Mirkovic D, Howell R, Kry S. An evaluation of three commercially available metal artifact reduction methods for CT imaging. *Phys Med Bio*. 2015; 60: 1047-1067.
18. Wang G, Snyder DL, O'Sullivan JA, Vannier MW. Iterative deblurring for CT metal artifact reduction. *IEEE Trans on Medical Imaging*. 1996; 15(5): 657-664.
19. Zhao S, Robertson DD, Wang G, Whiting B, Bae KT. X-ray CT metal artifact reduction using wavelets: an application for imaging total hip prostheses. *IEEE Trans Med Imaging*. 2000; 19(12): 1238-1247.
20. Man D, Nuyts J, Dupont P, Marchal G, Suetens P. An iterative maximum-likelihood polychromatic algorithm for CT. *IEEE Trans Med Imaging*. 2001; 20(10): 999-1008.

21. Kalender A, Hebel R, Ebersberger J. Reduction of CT artifacts caused by metallic implants. *Radiol.* 1987; 164(2): 576-577.

22. Greenlee R, Hill-Harmon M, Murray T, Thun M. Cancer Statistics. *CA Cancer J Clin.* 2001; 51(1): 15-36.

### Chapter 3

1. Schauer DA, Linton OW (2009) NCRP report no. 160, ionizing radiation exposure of the population of the United States, medical exposure--are we doing less with more, and is there a role for health physicists? *Health Phys* 97:1-5.

2. Moreno A, Frank S, Garden A, Rosenthal D, Fuller C, Gunn G, Reddy J, Morrison W, Williamson T, Holliday E, Phan J, Blanchard P. (2007) The effect of dental artifacts, contrast media, and experience on interobserver contouring variations in head and neck anatomy. *Am J Clin Oncol* 30:191-198.

3. Kim Y, Tomé W, Bal M, McNutt T, Spies L. (2006) The impact of dental metal artifacts on head and neck IMRT dose distributions. *Radiother Oncol* 79:198-202.

4. Mail N, Albarakati Y, Ahmad Khan, Saeedi F, Safadi N, Al-Ghamdi S, Saoudi A. (2013) The impacts of dental filling materials on RapidArc treatment planning and dose delivery: challenges and solution. *Med Phys* 40:081714.

5. Huang J, Followill D, Howell R, Liu X, Mirkovic D, Stingo F, Kry S. (2016) Approaches to reducing photon dose calculation errors near metal implants. *Med Phys* 43:5117-5130.

6. Zhao S, Robertson D, Wang G, Whiting B, Bae T (2000) X-ray CT metal artifact reduction using wavelets: an application for imaging total hip prostheses. *IEEE Trans Med Imaging* 19:1238-1247.

7. Man B, Nuyts J, Dupont P, Marchal G, Suetens P (2001) An iterative maximum-likelihood polychromatic algorithm for CT. *IEEE Trans Med Imaging* 20:999-1008.
8. Yazdia M, Gingras L, Beaulieu L (2005) An adaptive approach to metal artifact reduction in helical computed tomography for radiation therapy treatment planning: Experimental and clinical studies. *Int J Radiat Oncol Biol Phys* 62:1224-1231.
9. Zhang X, Wang J, Xing L (2011) Metal artifact reduction in x-ray computed tomography (CT) by constrained optimization. *Med Phys* 38:701-711.
10. Meyer E, Raupach R, Lell M, Schmidt B, Kachelrie M (2010) Normalized metal artifact reduction (NMAR) in computed tomography. *Med Phys* 37:5482-5493.
11. Li H, Noel C, Chen H, Harold Li H, Low D, Moore K, Klahr P, Michalski J, Gay HA, Thorstad W, Mutic S. (2012) Clinical evaluation of a commercial orthopedic metal artifact reduction tool for CT simulations in radiation therapy. *Med Phys* 39:7507-7517.
12. Axente M, Paidi A, Von Eyben R, Zeng C, Bani-Hashemi A, Krauss A, Hristov D. (2015) Clinical evaluation of the iterative metal artifact reduction algorithm for CT simulation in radiotherapy. *Med Phys* 42:1170-1183
13. GE Healthcare (2013) Smart metal artifact reduction (MAR) white paper.
14. Toshiba Medical. Single energy metal artifact reduction white paper.
15. Huang J, Kerns J, Nute J, Liu X, Balter P, Stingo F, Followill D, Mirkovic D, Howell R, Kry S. (2015) An evaluation of three commercially available metal artifact reduction methods for CT imaging. *Phys Med Biol* 60:1047-1067.
16. Das I, Paganetti H (2015) Principles and Practice of Proton Beam Therapy.

**The University of Texas MD Anderson Cancer Center UTHealth  
Graduate School of Biomedical Sciences  
Results of the Defense of the PhD Dissertation**

*This form is to be submitted to [gsbs.reports@uth.tmc.edu](mailto:gsbs.reports@uth.tmc.edu) within two weeks after the PhD defense.*

We, the undersigned, as the Advisory Committee in charge of the Defense of the PhD Dissertation for

Daniela Branco (student's name),

report that we have examined the candidate on his/her dissertation research on 4/24/20 (date).  
(Please check the boxes that apply.)

☒ We recommend that the candidate be granted the Doctor of Philosophy degree. If the Committee has attached any conditions to the recommendation, e.g., requiring that the dissertation be rewritten, the signing of the dissertation by the Committee members indicates the conditions have been met.

☒ The Advisory Committee is satisfied with the evaluation of the student's dissertation by Turnitin.

☒ The Advisory Committee agrees that the candidate understands and has acted appropriately on ethical issues related to the dissertation project.

☒ The Advisory Committee attests that the student contributed substantially to the text of any previously published work incorporated into the dissertation.

☒ The Advisory Committee attests that any figure taken from the student's publication(s) and used in the dissertation is the result of work done by the student, him/herself.

☒ The student has a first-author publication submitted [for students who entered prior to Fall 2014] or in press/published (for students who entered GSBS Fall 2014 and beyond).

☐ We do not recommend that the candidate be granted the Doctor of Philosophy degree at this time. [Please attach a letter to indicate the reason(s) for this decision.]

(Please type each committee member's name and degree(s) under the signature line.)

Dave Follon  
Dave Q Follon III  
Chair, Advisory Committee

Stephen Kr  
Stephen Kr

Patrice Taylor  
Patrice Taylor

Stephen Fren  
Stephen Fren

Xiaodong Zhang  
Xiaodong Zhang

John Rong  
John Rong

The signature of the Program Director below indicates that the Program Director acknowledges the outcome of the defense.

Richard E. Wendt III  
Richard E. Wendt III  
Program Director  
2020.05.18 08:29:44 -05'00'

Program Director, Printed Name and Signature

17. Grant R, Summers PA, Neihart JL, Blatnica AP, Sahoo N, Gillin MT, Followill DS, Ibbott GS. (2014) Relative stopping power measurements to aid in the design of anthropomorphic phantoms for proton radiotherapy. *J Appl Clin Med Phys* 15:4523.
18. Molineu A, Hernandez N, Nguyen T (2013) Credentialing results from IMRT irradiations of an anthropomorphic head and neck phantom. *Med Phys* 40: 022101.
19. Branco D, Taylor P, Zhang X, Li H, Guindani M, Followill D. (2017) An Anthropomorphic Head and Neck Quality Assurance Phantom for Credentialing of Intensity-Modulated Proton Therapy. *Int J Particle Ther* 4:40:47.

#### Chapter 4

1. O'Daniel J, Rosenthal D, Garden A, Barker J, Ahamad A, Ang K, Asper J, Blanco A, de Crevoisier R, Holsinger F, Patel C, Schwartz D, Wang H, Dong. *The Effect of Dental Artifacts, Contrast Media, and Experience on Interobserver Contouring Variations in Head and Neck Anatomy*. *American Journal of Clinical Oncology*, 2007. 30(2): p. 191-198.
2. Kim Y, Tomé W, Bal M, McNutt T, Spies L. *The impact of dental metal artifacts on head and neck IMRT dose distributions*. *Radiotherapy and Oncology*, 2006. 79.
3. Mail N, Albarakati Y, Ahmad Khan, Saeedi F, Safadi N, Al-Ghamdi S, Saoudi A. *The impacts of dental filling materials on RapidArc treatment planning and dose delivery: Challenges and solution*. *Medical Physics*, 2013. 40(8): p. 081714-n/a.
4. Herman, G.T., *Correction for beam hardening in computed tomography*. *Physics in Medicine & Biology*, 1979. 24(1): p. 81.
5. Yu L, Li H, Mueller J, Kofler JM, Liu X, Primak AN, Fletcher JG, Guimaraes LS, Macedo T, McCollough CH. *Metal artifact reduction from reformatted projections for hip*

*prostheses in multislice helical computed tomography: techniques and initial clinical results.*

Investigative radiology, 2009. 44(11): p. 691-696.

6. Kalender, W.A., R. Hebel, and J. Ebersberger, *Reduction of CT artifacts caused by metallic implants.* Radiology, 1987. 164(2): p. 576-577.

7. Meyer E, Raupach R, Lell M, Schmidt B, Kachelriess M. *Normalized metal artifact reduction (NMAR) in computed tomography.* Medical Physics, 2010. 37(10): p. 5482-5493.

8. Bal, M., L. Spies, *Metal artifact reduction in CT using tissue-class modeling and adaptive prefiltering.* Medical Physics, 2006. 33(8): p. 2852-2859.

9. Daniela Branco, S.K., Paige Taylor, John Rong, Benton Palka, Xiaodong Zhang, Steven J. Frank, and David Followill, *Image quality analysis of a novel CT metal artifact management technique against four major CT vendor techniques on an anthropomorphic head and neck phantom.* Conference Proceedings, ESTRO 2020.

10. Subhas N, Primak AN, Obuchowski NA, Gupta A, Polster JM, Krauss A, Iannotti JP. *Iterative metal artifact reduction: Evaluation and optimization of technique.* Skeletal Radiology, 2014. 43(12): p. 1729-1735.

11. Zhang, D. *Single Energy Metal Artifact Reduction A Reliable Metal Management Tool in CT.* 2017. White Paper.

12. Li H, Noel C, Chen H, Harold Li H, Low D, Moore K, Klahr P, Michalski J, Gay HA, Thorstad W, Mutic S. *Clinical evaluation of a commercial orthopedic metal artifact reduction tool for CT simulations in radiation therapy.* Medical physics, 2012. 39(12): p. 7507-7517.

13. Mahnken A, Raupach R, Wildberger JE, Jung B, Heussen N, Flohr TG, Günther RW, Schaller S. *A new algorithm for metal artifact reduction in computed tomography: in vitro and in vivo evaluation after total hip replacement.* Invest Radiol, 2003. 38(12): p. 769-75.



14. Verburg, J.M, J. Seco, *CT metal artifact reduction method correcting for beam hardening and missing projections*. Physics in Medicine and Biology, 2012. 57(9): p. 2803-2818.
15. Jessie Y, Kerns J, Nute J, Liu X, Balter P, Stingo F, Followill D, Mirkovic D, Howell R, Kry S. *An evaluation of three commercially available metal artifact reduction methods for CT imaging*. Physics in Medicine & Biology, 2015. 60(3): p. 1047.
16. Huang J, Followill D, Howell R, Liu X, Mirkovic D, Stingo F, Kry S. *Approaches to reducing photon dose calculation errors near metal implants*. Medical Physics, 2016. 43(9): p. 5117-5130.
17. Jikun W, Sandison G, Hsi W, Ringor M, Lu X. *Dosimetric impact of a CT metal artefact suppression algorithm for proton, electron and photon therapies*. Physics in Medicine and Biology, 2006. 51(20): p. 5183-5197.
18. Paganetti, H., *Range uncertainties in proton therapy and the role of Monte Carlo simulations*. Physics in Medicine and Biology, 2012. 57(11): p. R99-R117.
19. D. Branco, S.K., P. Taylor, J. Rong, X. Zhang, S. Frank, and D. Followill, *Development of a stereoscopic CT metal artifact management algorithm using gantry angle tilts for head and neck patients*. Journal of Applied Clinical Medical Physics, 2019. Accepted/pending publication, JACMP 2020.
20. Grant R, Summers PA, Neihart JL, Blatnica AP, Sahoo N, Gillin MT, Followill DS, Ibbott GS. *Relative stopping power measurements to aid in the design of anthropomorphic phantoms for proton radiotherapy*. J Appl Clin Med Phys, 2014. 15(2): p. 4523.

21. Lewis D, Taylor P, Followill D, Sahoo N, Mahajan A, Stingo F, Kry S. *A New Anthropomorphic Pediatric Spine Phantom for Proton Therapy Clinical Trial Credentialing*. Int J Part Ther, 2018. 4(4): p. 20-27.
22. Branco D, Taylor P, Zhang X, Li H, Guindani M, Followill D. *An Anthropomorphic Head and Neck Quality Assurance Phantom for Credentialing of Intensity-Modulated Proton Therapy*. International Journal of Particle Therapy, 2017. 4(3): p. 40-47.

## Chapter 5

1. Chen B, Leng S, Yu L, Holmes D 3rd, Fletcher J, McCollough C. *An open library of CT patient projection data*. SPIE Medical Imaging. Vol. 9783. 2016: SPIE.
2. William P. Sanders, Eeric Truumees, *Imaging of the postoperative spine*. Seminars in Ultrasound, CT and MRI. Vol 25, Issue 6, 2004: 523-535, ISSN 0887-2171, <https://doi.org/10.1053/j.sult.2004.09.007>.

## Chapter 6

## ***Chapter 9 - Vita***

Daniela Rezende Fiuza Branco was born in Belo Horizonte, Minas Gerais, Brazil. The son of Manuel da Rocha Fiuza Branco Junior and Maria Celeste Fiuza Branco. After concluding high school in 2008 at Colegio Santa Doroteia, Daniela moved to the United States where she received her degree of Bachelors of Science with a major in physics in 2014 at Wright State University Dayton, Ohio. In August of that year she entered The University of Texas Graduate School of Biomedical Sciences at Houston where she completed her Masters in medical physics in 2016. Upon completion, she enrolled in the medical physics PhD program at The University of Texas MD Anderson Cancer Center UTHealth Graduate School of Biomedical Sciences in 2016.

Permanent Address:

1175 Av. Dois – Veredas das Geraes

Nova Lima, MG Brasil